NTNU

Norwegian University of
Science and Technology

Aerodynamic Response of Slender Suspension Bridges

Birgir Fannar Gudmundsson

Civil and Environmental Engineering (2 year)
Submission date: June 2016
Supervisor: Einar Norleif Strømmen, KT
Co-supervisor: Kristian Berntsen, Satens Vegvesen
Bjørn Isaksen, Statens Vegvesen

Norwegian University of Science and Technology
Department of Structural Engineering

MASTEROPPGAVE 2014

Konstruksjonsteknikk

for

Birgir F. Gudmundsson

DYNAMISK RESPONS AV LANGE SLANKE HENGEBRUER

Aerodynamic response of slender suspension bridges

I Norge er det for tiden under planlegging en rekke meget slanke brukonstruksjoner, for eksempel Halsafjorden, Julsundet og Nordfjorden, alle som klassiske hengebroer, enten med enkelt eller splittet kassetverrsnitt i hovedbæreren. Disse broene har hovedspenn mellom ca. 1550 og 2050 m. De er svært utsatt for den dynamiske lastvirkningen fra vind. Halsafjorden som er den lengste med et spenn på ca. 2050 m er på grensen av det som tidligere er bygget av denne typen konstruksjoner. Prosjektene er spesielt krevende med hensyn til virvel-avløsning og bevegelsesinduserte krefter, dvs. med hensyn til å oppnå en konstruktiv utførelse som ikke medfører uakseptable virvelavløsningssvingninger ved lave vindhastigheter og tilstrekkelig sikkerhet mot en uakseptabelt lav stabilitetsgrense i koblede vertikal og torsjonssvingninger (”flutter”). Hensikten med denne oppgaven er å se på mulige utførelser av fjordkryssinger i denne spennvidden med tanke på å oppnå gunstige aerodynamiske egenskaper, og hvor det legges spesiell vekt på kryssinger i form av en eller annen variant av den klassiske hengebroen. Arbeidet foreslås lagt opp etter følgende plan:

1. Studenten setter seg inn i teorien for hengebroen som konstruksjonssystem.
2. Studenten setter seg inn i teorien for dynamisk respons og aerodynamisk stabilitet av slanke broer (se for eksempel *Strømmen: Theory of bridge aerodynamics, Springer 2006*).
3. For en eller flere aktuelle utførelser og spennvidder (avtales med veileder) skal det foretas en utredning med sikte på å kvantifisere de viktigste mekaniske egenskapene (dvs. aktuelle masse- og stivhetsegenskaper). Det skal foretas beregninger av de aktuelle egenfrekvensene og tilhørende egensvingeformene som er avgjørende for broens dynamiske egenskaper. I den grad det er mulig kan beregningene baseres på regnemaskinprogrammet Alvsat (eller innhentes fra Vegdirektoratet/Bruavdelingen).
4. For de samme tilfellene som er behandlet under punkt 3 skal det foretas beregninger av vindindusert dynamisk respons. Studenten kan selv velge om han vil legge vekt på virvelavløsning, «buffeting» eller stabilitet. For å kunne ta tilstrekkelig hensyn til bevegelsesinduserte krefter skal responsberegningene utføres i modalkoordinater i Matlab, enten i tidsplanet eller i frekvensplanet. I den grad tiden tillater det kan studenten velge å undersøke om en eller flere massedempere kan bedre systemets dynamiske egenskaper.

Studenten kan selv velge hvilke problemstillinger han ønsker å legge vekt på. Oppgaven skal gjennomføres i samarbeid med Dr.ing. Bjørn Isaksen og Siv.ing. Kristian Berntsen i Vegdirektoratet.

NTNU, 2016-01-15

Einar Strømmen

Preface

This thesis constitutes the result of the work carried out in spring 2016 as the final part of the Master's degree programme in Structural Engineering at the Norwegian University of Science and Technology (NTNU), Trondheim, Norway. This work has been carried out at the Department of Structural Engineering and in cooperation with the Norwegian Public Roads Administration.

I would like to give thanks to Professor Dr. Ing. Einar Strømmen at the university for his invaluable help and guidance throughout every stage of the work. I would also like to thank Kristian Berntsen for always answering my questions promptly and thoroughly, as well as the Norwegian Public Roads Administration for funding this thesis.

Birgir F. Gudmundsson
Trondheim, 2016-06-06

Abstract

The design and construction of the new coastal highway E39 along the west coast of Norway involves great challenges due to the large width and depth of the fjords along the coast. The new bridges involved in this project are very long and slender, which means aerodynamic design is very important. This thesis studies the aerodynamic stability of one such bridge, a proposed bridge crossing the Halsafjord. This bridge is a single span suspension bridge with a main span of 2050 meters, and a streamlined dual box girder deck, 32 meters wide in total.

The solution has been pursued in modal coordinates and in the frequency domain. The eigenfrequencies and eigenmodes have been calculated using the calculation program ALVSAT, and the numerical analysis of the bridge has been performed in MATLAB. Only the lowest vertical and torsion modes are considered in this analysis. The aerodynamic derivatives are determined from indicial functions obtained experimentally from wind tunnel testing.

A stability limit is identified by investigating where the response is greatly increased for a small increase in mean wind velocity until it approaches infinity. It has been concluded that flutter is the only type of instability that can affect the bridge. It is shown that while both the vertical and torsional modes gain considerable damping, motion induced loss of stiffness in torsion is the main driving force for the loss of stability. The calculations show that the flutter stability limit occurs only after the vertical and torsion modes have coupled, and that their cooperation alongside the loss of torsional stiffness cause the combined vertical-torsion peak in the frequency response function to be larger than the original peaks at $V = 0$.

Notation

Matrices and vectors:

Matrices are in general bold upper case Latin or Greek letters

Vectors are in general bold lower case Latin or Greek letters

$diag\,[\cdot]$ is a diagonal matrix whose content is written within the brackets.

$\det(\cdot)$ is the determinant of the matrix within the brackets.

Statistics:

$E\,[\cdot]$ is the average value of the variable within the brackets

$Var\,(\cdot)$ is the variance of the variable within the brackets

$Cov\,(\cdot)$ is the covariance of the variable within the brackets

$Coh\,(\cdot)$ is the coherence function of the content within the brackets

$R\,(\cdot)$ is the auto- or cross-correlation function

$\rho\,(\cdot)$ is the covariance coefficient of content within brackets

σ, σ^2 is the standard deviation, variance

Imaginary quantities:

i is the imaginary unit (i.e. $i = \sqrt{-1}$).

$\mathrm{Re}\,(\cdot)$ is the real part of the variable within the brackets.

$\mathrm{Im}\,(\cdot)$ is the imaginary part of the variable within the brackets.

Superscripts and bars above symbols:

Superscript T indicates the transposed of a vector or a matrix.

Superscript * indicates the complex conjugate of a quantity.

Dots above symbols indicate time derivatives (e.g. $\dot{r} = dr/dt$, $\ddot{r} = d^2r/dt^2$).

Prime on a variable (e.g. $C_L^{'}$) indicates its derivative with respect to a relevant variable.

Bar above a variable (e.g. $\bar{H}$) indicates its time invariant average value.

Tilde above a variable (e.g. $\tilde{C}$) indicates a modal quantity.

Hat above a symbol (e.g. $\hat{H}$) indicates a normalised quantity.

The use of indices:

Index x, y or z refers to the corresponding structural axis.

Index x_f, y_f or z_f refers to corresponding flow axis.

u, v or w refer to flow components.

i and j are general indices on variables.

n and m are mode shape or element numbers.
p and k are in general used as node numbers.
D, L, M refer to drag, lift and moment.
r refers to response.
s indicates quantities associated with vortex shedding.
exp as an index is short for exposed, referring to wind exposed part of the structure.
c is short for cables and indicates main cables

Abbreviations:
CC and SC are short for the centre of cross-sectional neutral axis and the shear centre.
c/c is short for centre-to-centre distance.
tot is short for total.
max, min are short for maximum and minimum
ae is short for aerodynamic, indicates a flow induced quantity.
cr is short for critical.
int or ext are short for internal and external.

Latin letters:
A Area, cross sectional area
A_n Wind spectrum coefficient $(n = u, v, w)$
$A(\omega), B(\omega)$ Complex amplitudes
$A_1^* - A_6^*$ Aerodynamic derivatives associated with the motion in torsion
a Constant or Fourier coefficient, amplitude
$\mathbf{a}, \mathbf{a}_r, \mathbf{a}_R$ Coefficient, Fourier coefficient vector associated with response or load
B Cross sectional width
$\mathbf{B}_q$ Buffeting dynamic load coefficient matrix at cross sectional level
b Constant, coefficient, band-width parameter
b_c Distance between cable planes
$\mathbf{b}_q$ Mean wind load coefficient vector
$C, \mathbf{C}$ Damping or load coefficient, matrix containing damping coefficient
$C_{ae}, \mathbf{C}_{ae}$ Aerodynamic damping, aerodynamic damping matrix
C_w Cross sectional warping constant
$\bar{C}$ Force coefficients at mean angle of incidence
C' Slope of load coefficient curves at mean angle of incidence
c Constant, coefficient, Fourier amplitude
$Co, \mathbf{Co}$ Co-spectral density, co-spectral density matrix
$\mathbf{Cov}_j$ Covariance matrix associated with variable j
D Cross sectional depth
d Constant or coefficient

E Modulus of elasticity

$\hat{E}, \hat{\mathbf{E}}$ Impedance, impedance matrix

e, e_c Exponential number ($\approx 2,7183$), cable sag

F Force

f Frequency [Hz]

$f(\cdot)$ Function of variable within brackets

G Modulus of elasticity in shear

G_{xx} Single sided spectral density

g Gravity constant

$H, \mathbf{H}, \mathbf{H}_r, \mathbf{H}_\eta$ Frequency response function, frequency response matrix, modal frequency response matrix

$H(t), \bar{H}$ Horizontal force component

$H_1^* - H_6^*$ Aerodynamic derivatives associated with the across-wind motion

h_0 Height of the pylons measured from the deck

h_c, h_m Length of hangers at an arbitrary position along span, hanger length at midspan

h_r Vertical distance between shear centre and hanger attachment

$I(\beta)$ Numerical equivalent to the joint acceptance function

I_t St Venant torsion

I_u, I_v, I_w Turbulence intensity of flow components u, v, w

I_y, I_z Moment of inertia with respect to y or z axis

$\mathbf{I}$ Identity matrix

$J, \mathbf{J}$ Joint acceptance function, joint acceptance matrix

k Index variable, node or sample number

$K, \mathbf{K}$ Stiffness, stiffness matrix

$K_{ae}, \mathbf{K}_{ae}$ Aerodynamic stiffness, aerodynamic stiffness matrix

L Length

${}^sL_n$ Integral length scales ($s = x_f, y_f, z_f$, $n = u, v, w$)

l_e Effective length

$M, \mathbf{M}$ Mass, mass matrix

m Distributed mass

$M_{ae}, \mathbf{M}_{ae}$ Aerodynamic mass, aerodynamic mass matrix

N Number, number of elements in a system

N_{tot} Cross section axial force

$P_1^* - P_6^*$ Aerodynamic derivatives associated with the along-wind motion

$Q, \mathbf{Q}$ Wind load or wind load vector at system level

Q_{ae} Aerodynamic motion induced wind load at system level

$q, \mathbf{q}$ Wind load or wind load vector at cross sectional level

q_s, q_c Half the self weight of the beam, self weight of a single main cable

$r, \mathbf{r}$ Cross sectional displacement or rotation, displacement vector

R_d Dynamic amplification factor

$R, \mathbf{R}$ External load, external load matrix

$S, \mathbf{S}$ Auto or cross spectral density, cross-spectral density matrix

$\mathbf{S}_j$ Cross spectral density matrix associated with variable j

s Dimensionless time

t, T Time, total length of time series

U Instantaneous wind velocity in the main flow direction

u Fluctuating along-wind horizontal velocity component

V Mean wind velocity

V_y, V_z Shear forces

v Fluctuating across wind horizontal velocity component

$\mathbf{v}$ Wind velocity vector containing fluctuating component

w Fluctuating across wind vertical velocity component

x, y, X Arbitrary variables, e.g. functions of t or ω

x, y, z Cartesian structural element cross sectional main neutral axis

x_r Chosen span-wise position for response calculation

z_0 Terrain roughness length

z_{min} Minimum height for the use of a logarithmic wind profile

z_{ref} Reference height above ground

Greek letters:

α Coefficient, angle of incidence

β Constant, coefficient

γ_m Material factor

$\zeta, \boldsymbol{\zeta}$ Damping ratio or damping ratio matrix

$\zeta_{ae}, \boldsymbol{\zeta}_{ae}$ Aerodynamic modal damping, matrix containing aerodynamic modal damping contributions

$\eta, \boldsymbol{\eta}$ Generalised modal coordinate, modal coordinate matrix

θ Index indicating cross sectional rotation or load (about shear centre)

$\kappa_{ae}, \boldsymbol{\kappa}_{ae}$ Aerodynamic modal stiffness, matrix containing aerodynamic modal stiffness contributions

ν Poisson's ratio

λ Coefficient, wave length

$\mu_{ae}, \boldsymbol{\mu}_{ae}$ Aerodynamic modal mass, matrix containing aerodynamic modal mass contributions

ρ Coefficient or density (e.g. of air)

τ Time shift (lag)

$\phi_{y_n}, \phi_{z_n}, \phi_{\theta_n}$ Continuous mode shape components in y, z and θ directions

$\Phi(\cdot)$ Indicial function

$\boldsymbol{\Phi}$ Mode shape matrix containing N_{mod} $\boldsymbol{\varphi}_n$ vectors

$\boldsymbol{\Phi}_r$ Mode shape matrix at span-wise response location x_r

ψ Trial function

$\boldsymbol{\varphi}$ Mode shape vector containing components $\phi_y, \phi_z, \phi_\theta$

ω, ω_n Circular frequency (rad/s), eigenfrequency associated with mode shape n

$\omega_n(V)$ Resonance frequency associated with mode n at mean wind velocity V

Symbols with both Latin and Greek letters:

$\Delta f, \Delta\omega$ Frequency segment

Δt Time step

Δs Spatial separation ($s = x, y, z$)

Contents

List of Figures

List of Tables

1 Introduction

The ongoing Ferjefri E39 project conducted by The Norwegian Public Roads Administration (NPRA) aims to allow for ferry-free transportation along the west coast of Norway. The new coastal highway route will stretch from Kristiansand in the south of Norway all the way up to Trondheim in central Norway at a total length of approximately 1100 km. The traffic along the coast today relies heavily on ferry links due to the extremely wide and deep fjords. This new route, when completed, will reduce travel time from 20 - 21 hours down to 12 - 13 hours, where the most significant contributions come from replacing the current ferry links with bridges. This involves great challenges, considering both the large width and depth of the fjords along the coast, reaching up to 5 km width and 1,5 km depth at the largest. Aerodynamic design of these bridges is therefore very important, especially considering that Norwegian suspension bridges are generally more slender than their foreign counterparts since they experience less traffic and require fewer lanes as a result [14].

In this thesis, a proposed single span suspension bridge over the Halsafjord in Western Norway will be studied with respect to its aerodynamic properties. The proposed bridge has a main span of 2050 meters, thus it surpasses the current record holder for the longest bridge span in the world, the Akashi-Kaikyo Bridge with its central span of 1991 meters [11]. The main focus will be on studying the aerodynamic stability of the bridge. This will be approached by two methods, first by conducting a dynamic response analysis of the bridge cross section over the relevant mean wind velocity range, and second by inspecting the roots of the impedance matrix to identify any common and simultaneous roots for its real and imaginary parts. A bridge has become unstable when its response drastically increases with a small increase of mean wind velocity. The main causes of instability problems are the motion induced forces that arise in the combined structure-flow system and can cause loss of stiffness and damping. Since an unstable bridge can lead to catastrophic deformations and rotations, it is important that the stability limits occur only at higher wind velocities than what could be expected on site. There exist stability limits for all eigenmodes of the system, yet it is the lowest modes that are of the most importance since they are the easiest ones to attain. In this thesis, only the lowest modes in the vertical direction and torsion will be considered.

The calculation program ALVSAT will be used to calculate the eigenfrequencies and eigenmodes of the bridge section [7]. Then dynamic response calculations and investigation of the stability limits will be performed in MATLAB using self-made scripts based on well-known theory of suspension bridges. Lastly, a study into the significance of some

key parameters will be conducted. The reader is assumed to be familiar with basic mathematics and statistics, as well as the basics of structural dynamics. However, a brief explanation of the most important concepts will be provided for completeness.

2 Basic Theory

2.1 Structural Dynamics

The study of structural dynamics is concerned with the response analysis for structures subject to dynamic, i.e. time dependent, loading. In its core, it is based upon the Principle of d'Alambert, which states that by considering an instantaneous moment in time where the system is frozen at an arbitrary position, we are able to establish equilibrium for any system that is in motion. In adopting this principle it is also assumed that the acceleration of the system can be interpreted as an inertia force $m\ddot{r}$ where m is the mass of the system and $\ddot{r}$ is the acceleration [21].

The behaviour of a dynamic system can be expressed as a combination of modes. Any dynamic motion can in fact be described by adding the relevant modes together. Each mode is characterized by certain parameters which depend on the system geometry and material properties as well as its boundary conditions. These parameters differ between modes, and they are known as the natural frequency ω_n, damping ratio ζ_n and mode shapes ϕ_n where n is the mode number [19]. These parameters are extracted by response calculations. Natural frequencies, also known as eigenfrequencies, can be thought of as the preference frequencies of a system. Given an undamped system left to oscillate by itself without any external influence, it will oscillate at an eigenfrequency and the oscillation shape will be the corresponding mode shape. If an external force drives the system to oscillate at its natural frequency ($\omega = \omega_n$), its response will increase dramatically due to a phenomenon known as resonance [3]. This is shown in Figure 2.1. The figure also shows the dramatic effect of damping on the response, as the response is plotted for different damping ratios ζ. Structural systems generally have very low damping, and hence the eigenfrequencies are very distinct.

The number of eigenfrequencies will always be the same as the number of degrees of freedom in the system. Analytically, all systems have an infinite amount of degrees of freedom. However it is usually deemed adequate to model a discrete system with a finite number of degrees of freedom. It is the lowest eigenfrequencies that are of the most interest anyway, since they require the least amount of energy to excite and usually give the largest response. Therefore, eigenfrequencies are usually presented in ascending order [4].

For dynamic systems, response calculations can be performed in what is known as the time domain or the frequency domain. The analyst is free to choose either one of those two approaches for the response calculations, and which approach is chosen depends entirely

on which is deemed more suitable for the situation at hand [21].

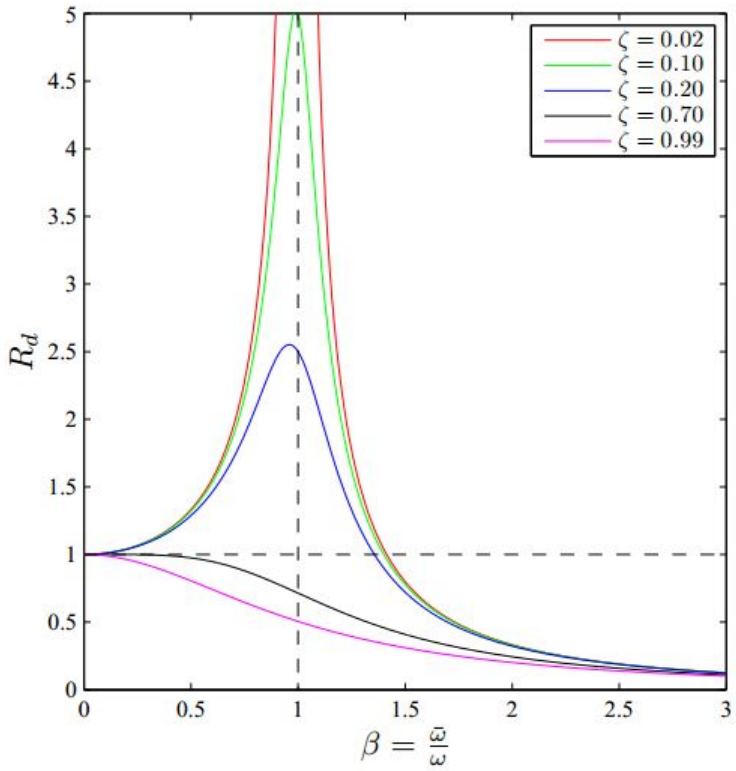

Figure 2.1: Dynamic amplification factor R_d as a function of frequency ratio and damping ratio [20]

2.1.1 Time Domain

In the time domain, the dynamic behaviour of a structure is described by differential equations of motion. In its most general form the equation of motion for a multi-degree of freedom system is as follows:

$$\mathbf{M}\ddot{\mathbf{r}}(t) + \mathbf{C}\dot{\mathbf{r}}(t) + \mathbf{K}\mathbf{r}(t) = \mathbf{R}(t) \tag{2.1}$$

where $\mathbf{M}$, $\mathbf{C}$ and $\mathbf{K}$ are the mass, damping and stiffness matrices of the system respectively, $\ddot{\mathbf{r}}$, $\dot{\mathbf{r}}$ and $\mathbf{r}$ are the acceleration, velocity and displacement and $\mathbf{R}(t)$ is the time dependent external loading on the system [3]. This equation is derived by applying d'Alambert's principle and taking force equilibrium. By solving this differential equation, the modal parameters ω_n, ζ_n and ϕ_n can be determined for the system. Since the load (and hence the response) is assumed to be a harmonic function, the solution takes the form [21]:

$$\mathbf{r} = \mathrm{Re}\left[\boldsymbol{\varphi} \cdot e^{i\omega t}\right] \tag{2.2}$$

where $\boldsymbol{\varphi}$ is the mode shape matrix. Substituting Eq. 2.2 into an undamped and unloaded version of Eq. 2.1 and simplifying, the equation takes the following form:

$$\left(\mathbf{K} - \omega^2 \mathbf{M}\right) \boldsymbol{\varphi} = \mathbf{0} \tag{2.3}$$

where the non-trivial solution is

$$\det\left(\mathbf{K} - \omega^2 \mathbf{M}\right) = 0 \tag{2.4}$$

which is an eigenvalue problem. By solving this, we are able to find the eigenfrequencies ω and corresponding eigenmodes ϕ [21].

2.1.2 Frequency Domain

In the frequency domain, the behaviour of a structure under dynamic loading is described by a set of algebraic equations. Applying Fourier transform, which is explained in more detail in Section 2.3.1, we can convert the equations of motion from Eq. 2.1 into a frequency domain description [21]. Starting from Eq. 2.1, we take the discrete Fourier transform:

$$\mathbf{r}(t) = \mathrm{Re}\sum_{\omega} \mathbf{a}_r(\omega) \cdot e^{i\omega t} \tag{2.5}$$

$$\mathbf{R}(t) = \mathrm{Re}\sum_{\omega} \mathbf{a}_R(\omega) \cdot e^{i\omega t} \tag{2.6}$$

where $\mathbf{a}_r$ and $\mathbf{a}_R$ are the Fourier coefficients of the displacement and load processes respectively. The equation of motion from Eq. 2.1 now takes the form:

$$\left(-\mathbf{M}\omega^2 + \mathbf{C}i\omega + \mathbf{K}\right) \cdot \mathbf{a}_r = \mathbf{a}_R \tag{2.7}$$

We can now define the frequency response function as the ratio between the Fourier transforms of the output r and the input R [19]:

$$\mathbf{H}_r(\omega) = \frac{\mathbf{a}_r}{\mathbf{a}_R} = \left(-\mathbf{M}\omega^2 + \mathbf{C}i\omega + \mathbf{K}\right)^{-1} \tag{2.8}$$

In other words, the frequency response function expresses the response of the structure to an applied force as a function of frequency. It is also known as a transfer function since it can be used to transfer the Fourier amplitude of the load $\mathbf{a}_R$ into the Fourier amplitude of the response $\mathbf{a}_r$ (and vice versa) if used on the form:

$$\mathbf{H}_r(\omega)\mathbf{a}_R = \mathbf{a}_r \tag{2.9}$$

It has been found convenient to express the frequency response function as a function of the frequency of motion, natural frequencies and corresponding damping ratios. For simplicity, we consider a single degree of freedom system for the development of the

expression. Starting with the single degree of freedom system version of the dynamic equilibrium equation [21],

$$M \cdot \ddot{r}(t) + C \cdot \dot{r}(t) + K \cdot r(t) = R(t) \tag{2.10}$$

where the response is given in the form $r(t) = \mathrm{Re}\left[A\left(\omega\right) \cdot e^{i\omega t}\right]$. Introducing this expression for $r(t)$ into 2.10 we obtain

$$\left(-M\omega^2 + Ci\omega + K\right) A(\omega) e^{i\omega t} = R(t) \cdot e^{i\omega t} \tag{2.11}$$

Dividing through the equation by K and introducing the natural frequencies $\omega_n^2 = K/M$ we get

$$\left(1 - \frac{\omega^2}{\omega_n^2} + \frac{C}{\omega_n^2 M} i\omega\right) A(\omega) e^{i\omega t} = \frac{R(t)}{K} e^{i\omega t} \tag{2.12}$$

Introducing the damping ratio $\zeta_n = C/\left(2\omega_n M\right)$ and solving for $A(\omega)$ gives

$$A(\omega) = \frac{R(t)}{K} \cdot \left[1 - \left(\omega/\omega_n\right)^2 + 2i\zeta_n \left(\omega/\omega_n\right)\right]^{-1} \tag{2.13}$$

By comparison with Eq. 2.9, we now find that the frequency response function in a single degree of freedom system system is given by

$$\hat{H}_n(\omega) = \left[1 - \left(\omega/\omega_n\right)^2 + 2i\zeta_n \left(\omega/\omega_n\right)\right]^{-1} \tag{2.14}$$

where the hat ($\hat{}$) is used to indicate that this is a non-dimensional quantity. This expression can be expanded for a general multi-degree of freedom system with N_{mod} number of modes as follows

$$\hat{\mathbf{H}}(\omega) = \begin{bmatrix} \hat{H}_1 & \cdots & 0 & \cdots & 0 \\ \vdots & \ddots & \vdots & \iddots & \vdots \\ 0 & \cdots & \hat{H}_n & \cdots & 0 \\ \vdots & \iddots & \vdots & \ddots & \vdots \\ 0 & \cdots & 0 & \cdots & \hat{H}_{N_{mod}} \end{bmatrix} \tag{2.15}$$

where $\hat{H}_n(\omega)$ is as given in Eq. 2.14 and $n = 1, \ldots, N_{mod}$.

2.1.3 Galerkin's Method

Galerkin's Method is a method of weighted residuals. In general, methods of weighted residuals are used to solve differential equations by expressing the solutions as a combination of known trial functions ψ_i that satisfy the boundary conditions and unknown coefficients a_i. Therefore, Galerkin's method can be used as a way of converting the continuous equi-

librium equation of motion (Eq. 2.1) into a numerical discrete problem. Since the solution is numerical, it is only an approximation and thus a residual $f(r, \ddot{r}) = R$ will be produced. The method aims to select the coefficients a_i such that the residual is minimized, or equal to zero, over a chosen domain. To evaluate the solution, weighted functions are used. In Galerkin's Method, the weighted functions are chosen to be equal to the trial functions. Hence, if the trial function is orthogonal, $\int \psi_i \psi_j = 0 \quad \text{when} \quad i \neq j$, the residual will be orthogonal as well [17]. Taking the exact unloaded and undamped version of Eq. 2.1,

$$f(r, \ddot{r}) = \mathbf{M}\ddot{\mathbf{r}}(t) + \mathbf{K}\mathbf{r}(t) = \mathbf{0} \tag{2.16}$$

Galerkin's Method converts the equation into the following numerical eigenvalue problem [21]

$$\mathbf{A} \cdot \mathbf{a} = \mathbf{0} \tag{2.17}$$

with unknown coefficients $\mathbf{a} = \begin{bmatrix} a_1 & \cdots & a_i & a_{N_\psi} \end{bmatrix}^T$, such that

$$r \approx \mathrm{Re} \sum_{i=1}^{N_\psi} a_i \cdot \psi_i(x) \cdot e^{i\omega t} \tag{2.18}$$

The approximate solution, given by

$$f\left(\sum_{i=1}^{N_\psi} a_i \psi_i e^{i\omega t} \right) = 0 \tag{2.19}$$

is successively weighed with the same functions ψ_j, $j = 1, 2, \ldots, N_\psi$ and integrated over its functional space (i.e. its length L or surface A), rendering Eq. 2.17, which in its full form is given by

$$\begin{bmatrix} A_{11} & \cdots & A_{1j} & \cdots & A_{1N_\psi} \\ \vdots & \ddots & \vdots & \iddots & \vdots \\ A_{i1} & \cdots & A_{ij} & \cdots & A_{iN_\psi} \\ \vdots & \ddots & \vdots & \iddots & \vdots \\ A_{N_\psi 1} & \cdots & A_{N_\psi j} & \cdots & A_{N_\psi N_\psi} \end{bmatrix} \begin{bmatrix} a_1 \\ \vdots \\ a_i \\ \vdots \\ a_{N_\psi} \end{bmatrix} = \mathbf{0} \tag{2.20}$$

where

$$A_{ij} = \int_L \psi_i \cdot f(\psi_j, \omega)\, dx \qquad \text{or} \qquad A_{ij} = \int_L \psi_i \cdot f(\psi_j, \omega)\, dA \tag{2.21}$$

2.2 Stochastic Process

A stochastic process is a physical process which is random in time and space and can only be predicted with a certain probability. Due to this randomness, the measured outcome of a process represents only one particular realisation of that process. If measurements of the process were to be repeated, even under the same conditions, the results would differ to some extent. I.e. there is an infinite number of other possible representatives of the process. Therefore the physical characteristics of a stochastic process must be described by the statistics of numerous sets of realisations [22]. An example of a stochastic process is shown in Figure 2.2. Another relevant example of a stochastic process is wind loading on a structure. Note that since the process itself is stochastic, it follows that any subsequent process will also be stochastic. Hence, the stochastic wind loading will produce a stochastic response in the structure. Stochastic dynamics is a field of dynamics that concerns itself with these stochastic processes, or noisy signals, in other words.

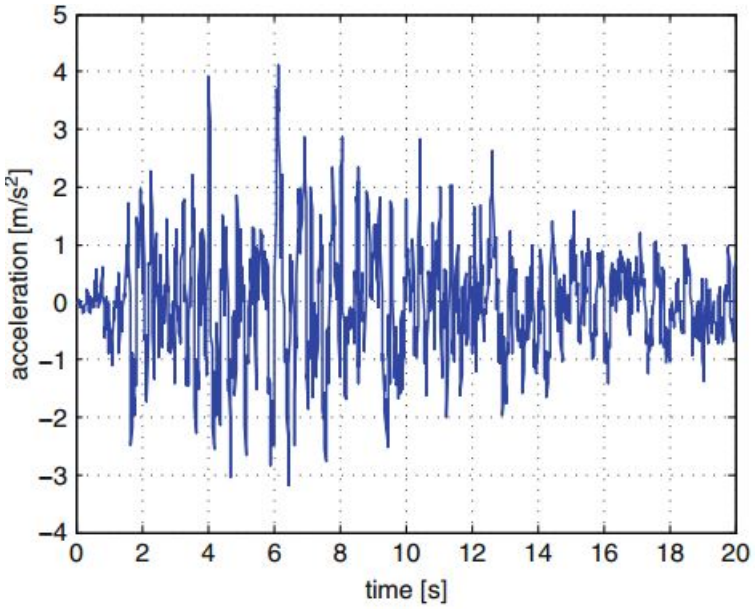

Figure 2.2: An example of a stochastic process is acceleration of the ground due to earthquakes [18]

2.3 Frequency Response

To identify the eigenfrequencies and damping properties of a structure under stochastic loading, it is appropriate to pursue a stochastic solution in frequency domain [21]. The aim of this section is to define and explain the various properties of the process needed for the response analysis in the frequency domain.

2.3.1 Fourier Transform

The Fourier transform is a fundamental tool in signal analysis used to transfer the signal from time domain to frequency domain. By taking the Fourier transform of a signal, we decompose the signal as a linear combination of sinusoidal (harmonic) functions at different frequencies [19]. In other words, any signal can be split up and described as the sum of multiple harmonic signals. It is noted that Fourier transformation is a reversible process and is therefore able to bind together the time domain and the frequency domain. Though this type of decomposition is originally developed for periodical functions, it can be extended to non-periodic functions. Any non-periodic function $x(t)$ which satisfies the condition [6]:

$$\int_{-\infty}^{\infty} |x(t)|dt < \infty \tag{2.22}$$

can be represented by the integral:

$$x(t) = \int_{-\infty}^{w} (A(\omega)cos\omega t + B(\omega)sin\omega t)\, d\omega \tag{2.23}$$

where

$$A(\omega) = \frac{1}{\pi}\int_{-\infty}^{w} x(t)cos\omega t dt \quad ; \quad B(\omega) = \frac{1}{\pi}\int_{-\infty}^{m} x(t)sin\omega t dt \tag{2.24}$$

More conveniently, this can be expressed in complex form:

$$x(t) = \int_{-\infty}^{\infty} X(\omega)e^{i\omega t}d\omega \tag{2.25}$$

where

$$X(\omega) = \frac{1}{2\pi}\int_{-\infty}^{\infty} x(t)e^{-i\omega t}dt \tag{2.26}$$

Examples of non-periodic functions are transient and random signals. With this theory, any signal, periodic or non-periodic, can now be decomposed into a sum of harmonic functions. In practice, however, it is impossible to do measurements over an infinitely long time period. Therefore discrete Fourier transform is taken, as it makes it possible to represent a finite time series. On a discrete form, Eq. 2.25 and Eq. 2.26 become [6]:

$$x(t_k) \equiv x_k = \sum_{n=0}^{N-1} X_n e^{i2\pi nk/N} \tag{2.27}$$

$$X(\omega_n) \equiv X_n = \frac{1}{N}\sum_{k=1}^{N} x_k e^{-i2\pi nk/N} \quad , \quad n = 1, \ldots, N \tag{2.28}$$

where N is the total number of data points. In our case, N represents time instants with a constant time step $\triangle t$.
The discrete Fourier transform requires a great amount of computational effort, however, since its evaluation requires N^2 operations. Therefore an algorithm under the name of fast Fourier transform has been developed. Given that the number of data points equals a power of 2, this algorithm reduces the number of operations to $N \cdot log_2 N$, making fast Fourier transform a much more efficient tool for Fourier transform than its discrete counterpart [19]. The fast Fourier transform algorithm is included in MATLAB as a function.

2.3.2 Modal Coordinates

The equilibrium equation of motion has already been presented in Section 2.1.1 and it has been established that the solution is a harmonic motion which may be described by

$$\mathbf{r} = \mathrm{Re}\left(\boldsymbol{\varphi} \cdot e^{i\omega t}\right) \qquad \text{where} \qquad \boldsymbol{\varphi} = \begin{bmatrix} a_1 & a_2 \end{bmatrix}^T \tag{2.29}$$

If the system is subject to any external load, an approximate solution to the equilibrium equation may be obtained by separating the position and time variables, and taking a linear combination of a limited set of chosen eigenmodes which are known, that is [21]

$$\mathbf{r}(t) \approx \sum_{i=1}^{N_{mod}} \boldsymbol{\varphi}_n \eta_n(t) \tag{2.30}$$

where $\eta_n(t)$ are now the unknown variables of the system. For continuous systems the mode shape functions are continuous as well, such that

$$\mathbf{r}(x,t) \approx \sum_{i=1}^{N_{mod}} \boldsymbol{\varphi}_n(x) \eta_n(t) \tag{2.31}$$

Instead of working with a linear combination of all the degrees of freedom of the system (N_r), we now work with a linear combination of a selected number of modes, N_{mod}. The computational advantage of this modal approach is considerable, since structural systems have a large number of degrees of freedom while the number of modes to consider can be chosen to be quite low and yet gain sufficient accuracy.
In a discrete format it is convenient to define a mode shape matrix [21]

$$\boldsymbol{\Phi} = \begin{bmatrix} \boldsymbol{\varphi}_1 & \boldsymbol{\varphi}_2 & \cdots & \boldsymbol{\varphi}_n & \cdots & \boldsymbol{\varphi}_{N_{mod}} \end{bmatrix} \tag{2.32}$$

where $\boldsymbol{\varphi}_n$ $(n = 1, 2, \ldots, N_{mod})$ contains the mode shape numerical values

$$\boldsymbol{\varphi}_n = \begin{bmatrix} \boldsymbol{\varphi}_1 & \boldsymbol{\varphi}_2 & \cdots & \boldsymbol{\varphi}_p & \cdots & \boldsymbol{\varphi}_{N_r} \end{bmatrix}^T \tag{2.33}$$

and a time dependent unknown vector

$$\boldsymbol{\eta}(t) = \begin{bmatrix} \eta_1 & \eta_2 & \cdots & \eta_n & \cdots & \eta_{N_{mod}} \end{bmatrix}^T \tag{2.34}$$

which is the modal coordinate vector. Then Eq. 2.30 takes the general form

$$\mathbf{r}(t) \approx \boldsymbol{\Phi}\boldsymbol{\eta}(t) \tag{2.35}$$

To establish the equilibrium equation of motion in modal coordinates, we substitute Eq. 2.35 into Eq. 2.1 and pre-multiply the entire equation by $\boldsymbol{\Phi}^T$,

$$\boldsymbol{\Phi}^T\mathbf{M}\boldsymbol{\Phi}\ddot{\boldsymbol{\eta}}(t) + \boldsymbol{\Phi}^T\mathbf{C}\boldsymbol{\Phi}\dot{\boldsymbol{\eta}}(t) + \boldsymbol{\Phi}^T\mathbf{K}\boldsymbol{\Phi}\boldsymbol{\eta}(t) = \boldsymbol{\Phi}^T\mathbf{R}(t) \tag{2.36}$$

This expression is simplified by defining modally equivalent structural properties (modal mass, stiffness and damping) and a modal load vector, i.e.

$$\begin{aligned} \tilde{\mathbf{M}} &= \boldsymbol{\Phi}^T\mathbf{M}\boldsymbol{\Phi} \\ \tilde{\mathbf{C}} &= \boldsymbol{\Phi}^T\mathbf{C}\boldsymbol{\Phi} \\ \tilde{\mathbf{K}} &= \boldsymbol{\Phi}^T\mathbf{K}\boldsymbol{\Phi} \\ \tilde{\mathbf{R}}\,(t) &= \boldsymbol{\Phi}^T\mathbf{R}\,(t) \end{aligned} \tag{2.37}$$

The modal dynamic equilibrium equation is then expressed by

$$\tilde{\mathbf{M}}\ddot{\boldsymbol{\eta}}(t) + \tilde{\mathbf{C}}\dot{\boldsymbol{\eta}}(t) + \tilde{\mathbf{K}}\boldsymbol{\eta}(t) = \tilde{\mathbf{R}}(t) \tag{2.38}$$

The orthogonal properties of the mode shapes give an additional benefit to using modal coordinates for frequency response analysis, that is, all of the off diagonal terms in $\tilde{\mathbf{M}}$ and $\tilde{\mathbf{K}}$ are zeros. Thus

$$\begin{aligned} \tilde{\mathbf{M}} &= diag\left[\tilde{M}_n\right] \\ \tilde{\mathbf{K}} &= diag\left[\tilde{K}_n\right] \end{aligned} \tag{2.39}$$

where $\tilde{M}_n = \boldsymbol{\varphi}_n^T\mathbf{M}\boldsymbol{\varphi}_n$ and $\tilde{K}_n = \boldsymbol{\varphi}_n^T\mathbf{K}\boldsymbol{\varphi}_n$. Since damping data is in general also associated with a particular mode shape, we also have that

$$\tilde{\mathbf{C}} = diag\left[\tilde{C}_n\right] \tag{2.40}$$

By introducing an arbitrary mode shape $\boldsymbol{\varphi}_n$ and its corresponding eigenfrequency ω_n into Eq. 2.3 and pre-multiplying by $\boldsymbol{\varphi}_n^T$,

$$\begin{aligned} \boldsymbol{\varphi}_n^T \left(\mathbf{K} - \omega_n^2 \mathbf{M}\right) \boldsymbol{\varphi}_n &= \mathbf{0} \\ \Rightarrow \boldsymbol{\varphi}_n^T \mathbf{K} \boldsymbol{\varphi}_n &= \omega_n^2 \boldsymbol{\varphi}_n^T \mathbf{M} \boldsymbol{\varphi}_n \end{aligned} \tag{2.41}$$

it is seen that the terms of the modal stiffness matrix may be more conveniently determined from

$$\tilde{K}_n = \omega_n^2 \tilde{M}_n \tag{2.42}$$

$\tilde{C}_n$ is then determined from

$$\tilde{C}_n = 2\tilde{M}_n \omega_n \zeta_n \tag{2.43}$$

where ζ_n are the modal damping ratios associated with a corresponding mode shape and critical modal damping $2\tilde{M}_n\omega_n$. It is now apparent that knowledge of the contents of the stiffness matrix $\mathbf{K}$ and the damping matrix $\mathbf{C}$ is not required to perform analysis in modal coordinates [21].
It should be noted that modal coordinates can be used both in time and frequency domain analyses, and whether it is more convenient to pursue a solution on original or modal coordinates depends on the case at hand. A solution in frequency domain is often far more conveniently obtained in modal degrees of freedom than in original.

2.3.3 Spectral Density

To define spectral density we first need to define correlation functions. Consider a random vibration parameter $x(t)$ in the time domain. Then the autocorrelation function $R_{xx}(\tau)$ is defined as [6]:

$$R_{xx}(\tau) = E\left[x(t) \cdot x(t+\tau)\right] \tag{2.44}$$

where τ is an arbitrary time lag. In words, this means that the autocorrelation function is the expected value of the vibration parameter multiplied by itself at a time shift τ. Unlike the random vibration parameter itself, its autocorrelation satisfies the requirements for Fourier transformation. If we then take the Fourier transform of the autocorrelation, we get what is called the auto- or power spectral density $S_{xx}(\omega)$:

$$S_{xx}(\omega) = \frac{1}{2\pi} \int_{-\infty}^{\infty} R_{xx}(\tau) \cdot e^{-i\omega\tau} d\tau \tag{2.45}$$

This means that spectral densities and correlation functions are Fourier transform pairs. The power spectral density is a frequency domain representation of the time domain variance in the process, and the area under the spectral density curve will be the variance of the process itself. In other words, the spectral density of $x(t)$ is intended to represent the

variance density distribution in the frequency domain. For example, in wind engineering the spectral densities are used to describe the fluctuation components of a wind flow in the frequency domain [22].
Eq. 2.45 describes a two-sided power spectral density, that is, the spectra is defined from $-\infty$ to ∞. The spectral density can also be described as one-sided, i.e. from 0 to ∞. Eq. 2.45 then becomes [19]:

$$G_{xx}(\omega) = \frac{2}{\pi} \int_0^\infty R_{xx}(\tau) \cdot cos(\omega t) d\tau \tag{2.46}$$

It is seen that when taking the one-sided spectrum we are no longer operating with a complex format. The relationship between the two-sided and the one-sided spectral density is simply $G_{xx}(\omega) = 2 \cdot S_{xx}(\omega)$. That is, a symmetric double-sided auto spectrum may be defined as the half of the corresponding one-sided spectrum [22].
Another way of defining the spectra is as expressed by Fourier amplitudes, also known as Fourier coefficients as in Section 2.1.2. Defining a non-normalized amplitude

$$a_k(\omega_k) = \int_0^T x(t) \cdot e^{-i\omega_k t} dt = T \cdot d_k \tag{2.47}$$

the two-sided power spectral density may be defined by

$$S_{xx}(\omega) = \frac{(a_k^*/T)\,(a_k/T)}{2\pi/T} = \frac{1}{2\pi T} \cdot a_k^* a_k \tag{2.48}$$

where T is the total length of the given time series. In the limit of $T \to \infty$, assuming sufficiently large number of realisations of the process, the two-sided power spectral density may be written on the following continuous form

$$S_{xx}(\omega) = \lim_{T\to\infty} \frac{1}{2\pi T} \cdot a^*(\omega) \cdot a(\omega) \tag{2.49}$$

It may also be useful to define some statistical properties between processes. For a pair of time variable functions $x(t)$ and $y(t)$, the cross correlation is defined similar to the autocorrelation function:

$$R_{xy}(\tau) = E\left[x(t) \cdot y(t+\tau)\right] \tag{2.50}$$

After a Fourier transform, we obtain what is known as the cross spectral density [6]:

$$S_{xy}(\omega) = \frac{1}{2\pi} \int_{-\infty}^\infty R_{xy}(\tau) \cdot e^{-i\omega\tau} d\tau \tag{2.51}$$

The cross spectral density contains the frequency domain properties between processes.

In the same sense that the power spectral density represents the time domain variance in the frequency domain, the cross spectral density represents the time domain covariance in the frequency domain [22]. It is noted that cross spectra are generally complex functions of frequency for non-symmetric systems.
Lastly, the spectral density S_{xx} of the input (f.ex. wind load) and the output S_{rr} (response of structure) have the following relation:

$$\mathbf{S}_{rr}(\omega) = \lim_{T\to\infty} \frac{1}{\pi T} \left(\mathbf{a}_r^* \cdot \mathbf{a}_r^T\right) = \lim_{T\to\infty} \frac{1}{\pi T} \left[\left(\mathbf{H}\left(\omega\right)\mathbf{a}_x\right)^* \cdot \left(\mathbf{H}\left(\omega\right)\mathbf{a}_x\right)^T\right] = \mathbf{H}^*\left(\omega\right) \cdot \lim_{T\to\infty} \frac{1}{\pi T} \left(\mathbf{a}_x^* \cdot \mathbf{a}_x^T\right) \cdot \mathbf{H}^T\left(\omega\right) = \mathbf{H}^*(\omega) \cdot \mathbf{S}_{xx}(\omega) \cdot \mathbf{H}^T(\omega) \quad (2.52)$$

where $\mathbf{H}^*(\omega)$ is the frequency response function complex conjugate transpose and $\mathbf{H}^T(\omega)$ is the frequency response function transposed. Therefore it is possible to transform one into the other. In the case of one-sided spectrum, $\mathbf{H}^*(\omega) = \mathbf{H}^T(\omega)$ since we do not have any complex part. Eq. 2.52 then becomes:

$$\mathbf{S}_{rr}(\omega) = |\mathbf{H}(\omega)|^2 \cdot \mathbf{S}_{xx}(\omega) \quad (2.53)$$

2.3.4 Coherence Function

The statistical property used to examine the relation between two properties is known as coherence. The coherence function for two processes $x(t)$ and $y(t)$ is defined as follows [22]:

$$Coh_{xy}(\omega) = \frac{|S_{xy}(\omega)|^2}{S_{xx}(\omega)S_{yy}(\omega)} = \frac{|G_{xy}(\omega)|^2}{G_{xx}(\omega)G_{yy}(\omega)} \quad (2.54)$$

Values of the coherence functions will always satisfy $0 \leq Coh_{xy}(\omega) \leq 1$, and give an estimation of to what extent $y(t)$ may be predicted from $x(t)$. In practice, all imaginary parts will cancel out as they are only mathematical tools, and are not physically real. Therefore only the real part of $Coh_{xy}(\omega)$ is of interest, also known as the co-spectrum:

$$\hat{Co}_{xy}\left(\omega\right) = \frac{\mathrm{Re}\left[S_{xy}\left(\omega\right)\right]}{\sqrt{S_x\left(\omega\right) \cdot S_y\left(\omega\right)}} \quad (2.55)$$

If $x(t)$ and $y(t)$ are realisations of the same stationary and ergodic process then $S_x(\omega) = S_y\left(\omega\right)$ and the co-spectrum is given by

$$\hat{Co}_{xy}\left(\omega\right) = \frac{1}{S_x\left(\omega\right)} \mathrm{Re}\left[S_{xy}\left(\omega\right)\right] \quad (2.56)$$

It is worth mentioning that the coherence function can be used to help identify the actual eigenfrequencies and modes of the system in the case of noisy signals, and by utilizing this

parameter we can minimize any possible error in the determination of eigenfrequencies and their corresponding modes. As previously stated, the coherence function has a range from 0 to 1, and will be close to 1 in correspondence of a natural frequency because of the high signal-to-noise ratio at that frequency. Therefore, by comparing the coherence function with the power spectral density we can identify which peak in the spectra is a natural frequency peak and which is a peak due to disturbances [19].

2.3.5 Time Series Simulation

A realisation of time domain response r_z and r_θ at a point x along the span may be simulated from a single point spectral density at any given wind velocity V. A single-sided auto spectral density $S_x(\omega)$ may be given on the discrete form as strømmen-2010

$$S_x(\omega_k) = \frac{c_k^2}{2\Delta\omega_k} \tag{2.57}$$

where $\Delta\omega_k$ is a frequency segment, $c_k = \sqrt{a_k^2 + b_k^2}$ and

$$\begin{bmatrix} a_k \\ b_k \end{bmatrix} = \frac{2}{T}\int_0^T x(t) \begin{bmatrix} \cos\omega_k t \\ \sin\omega_k t \end{bmatrix} dt \tag{2.58}$$

A time domain representative of the spectral density is then obtained by subdividing S_x into N blocks along the frequency axis, where each block covers a frequency segment $\Delta\omega_k$ and has its centre at ω_k. Hence, it is seen that the spectral density is the variance of each harmonic component per frequency segment. This is shown in Figure 2.3.

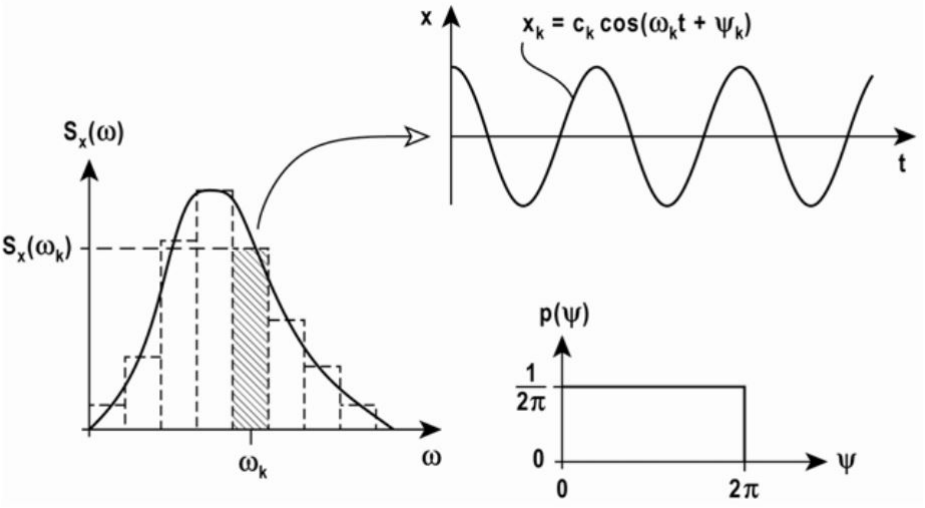

Figure 2.3: Obtaining a time series simulation from spectral density [22]

A time series representative of x is finally obtained by

$$x(t) = \mathrm{Re}\left\{\sum_{k=1}^{N} c_k \exp\left[i\left(\omega_k t + \psi_k\right)\right]\right\} \tag{2.59}$$

where ψ_k is an arbitrary phase angle between 0 and 2π. The amplitudes c_k may readily be obtained from the expression for $S_x(\omega_k)$ above,

$$c_k = \left[2 \cdot S_x(\omega_k) \cdot \Delta\omega_k\right]^{1/2} \tag{2.60}$$

3 Aerodynamics

3.1 Wind Flow

A wind field met by a structure is in the following theory described at a certain point by its own Cartesian coordinate system $(x, y, z)_f$, where x_f is the main flow direction and z_f is the vertical direction. For simplicity, it is taken for granted that the wind field is stationary and homogeneous within the time and space considered. The wind flow can be split up into a mean wind velocity $V(x_f, y_f, z_f)$ and a fluctuating part, or turbulence component, described by the variance or standard deviation. The oncoming wind flow is denoted

$$U(x_f, y_f, z_f, t) = \begin{cases} V(x_f, y_f, z_f) + u(x_f, y_f, z_f, t) \\ v(x_f, y_f, z_f, t) \\ w(x_f, y_f, z_f, t) \end{cases} \tag{3.1}$$

where $V + u$ is the along wind mean and fluctuating part, v is the horizontal fluctuating part perpendicular to flow main direction and w is the vertical fluctuating part [22]. The wind flow met by a bridge type structure is shown in Figure 3.1.

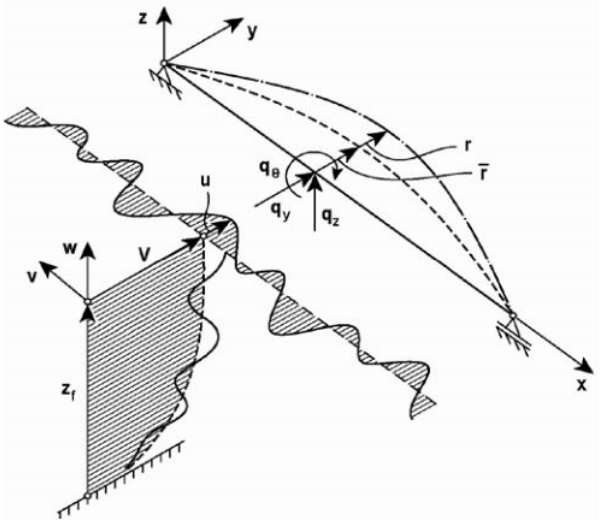

Figure 3.1: Bridge type structure subject to fluctuating wind field [21]

The mean wind velocity is generally described as the average wind velocity over a chosen time interval. It depends greatly on the local topography, as obstacles such as hills or valleys might diminish or increase the design wind velocity. As seen from Figure 3.1, the mean wind velocity increases exponentially with height as a function of a reference height,

often chosen to be $z_{ref} = 10\,m$. This height variation of velocity is due to horizontal friction forces from the surface which retard the flow, most significantly close to the ground. From Figure 3.1 it is further seen that the wind flow not only varies with height, but along the span as well. Hence, the fluctuating turbulence components are functions of both time and space. In the presence of large obstacles, turbulence becomes large close to the ground, but decreases steadily away from the ground. In the absence of obstacles, for example over a body of water, the turbulence is small [10].

Two further quantities are used to characterize the oncoming wind flow, the integral length scale and the turbulence intensity. The integral length scale ${}^{s}L_n$ provides a measure of the average length of a turbulent wind eddy in particular direction of flow, where $n = u,\, v,\, w$ and $s = x_f,\, y_f,\, z_f$ [22]. Turbulence intensity is a scale used for characterizing turbulence as a percent. Steady wind flow with low fluctuations has low turbulence intensity and an unsteady flow with high fluctuations has high turbulence intensity. An idealized flow of air with no fluctuation components would have a turbulence intensity value of 0%, however this case is unrealistic. Because of how turbulence intensity is calculated, values greater than 100% are possible. This can be the case for example when the average air speed is small and yet there are large fluctuations present [24]. An expression for turbulence intensities is given by [22]

$$I_n(z_f) = \frac{\sigma_n(z_f)}{V(z_f)} \qquad \text{where} \quad n = u, v, w \tag{3.2}$$

where $\sigma_n(z_f)$ is the standard deviation of the fluctuating wind velocity V at reference height z_f. A typical variation of the turbulence intensity for the along wind u component is given by

$$I_u(z_f) \approx \begin{cases} 1/\ln(z_f/z_0) & \text{when } z_f > z_{min} \\ 1/\ln(z_{min}/z_0) & \text{when } z_f \leq z_{min} \end{cases} \tag{3.3}$$

where z_0 is called the roughness length and z_{min} is a lower limit for the vertical height of wind velocity profile. These values depend on the terrain in the observed area, and can be found in standards. Under isotropic conditions high above the ground, $I_u \approx I_v \approx I_w$. From a height of over z_{min} to about 200 m, I_v and I_w can be approximated as

$$\begin{bmatrix} I_v \\ I_w \end{bmatrix} \approx \begin{bmatrix} 3/4 \\ 1/2 \end{bmatrix} \cdot I_u \tag{3.4}$$

What remains is an expression for the turbulence properties both in the time and frequency domain. The following auto covariance functions and covariance coefficients are used to represent the time domain properties of turbulence,

$$\begin{bmatrix} Cov_u(\tau) \\ Cov_v(\tau) \\ Cov_w(\tau) \end{bmatrix} = \begin{bmatrix} E\left[u(t) \cdot u(t+\tau)\right] \\ E\left[v(t) \cdot v(t+\tau)\right] \\ E\left[w(t) \cdot w(t+\tau)\right] \end{bmatrix} = \frac{1}{T} \int_0^T \begin{bmatrix} u(t) \cdot u(t+\tau) \\ v(t) \cdot v(t+\tau) \\ w(t) \cdot w(t+\tau) \end{bmatrix} dt \tag{3.5}$$

$$\rho_n(\tau) = \frac{Cov_n(\tau)}{\sigma_n^2} \qquad \text{where} \quad n = u, v, w \tag{3.6}$$

where τ is an arbitrary time lag. The cross covariance coefficients between two processes (turbulence components in this case) are defined by

$$\rho_{nm}(\tau) = \frac{Cov_{nm}(\Delta s, \tau)}{\sigma_n \cdot \sigma_m} \qquad \begin{cases} m, n = u, v, w \\ \Delta s = \Delta x_f, \Delta y_f, \Delta z_f \end{cases} \tag{3.7}$$

where Δs is an arbitrary separation. Spectral densities are used to represent the frequency domain properties of the turbulence components. In this thesis, the following non-dimensional expression proposed by J.C. Kaimal will be used to describe the turbulence spectral density

$$\frac{f \cdot S_n\{f\}}{\sigma_n^2} = \frac{A_n \cdot \hat{f}_n}{\left(1 + 1.5 \cdot A_n \cdot \hat{f}_n\right)^{5/3}} \qquad \text{where} \quad n = u, v, w \tag{3.8}$$

where $\hat{f}_n = f \cdot {}^{x_f} L_n / V$, f is the frequency in Hz and ${}^{x_f} L_n$ is the integral length scale of the relevant turbulence component. By converting f to angular frequency ω in rad/s, the normalized auto spectral density takes the following form:

$$\hat{S}_n(\omega) = \frac{S_n(\omega)}{\sigma_n^2} = \frac{A_n {}^{x_f} L_n / V}{(1 + 1,5 \cdot A_n \omega^{x_f} L_n / V)^{5/3}} \qquad \text{where} \quad n = u, v, w \tag{3.9}$$

Full scale recordings are required to determine the A_n parameter, however the following values may be adopted if such recordings are not available: $A_u = 6.8$, $A_v = A_w = 9.4$ [22]. The Kaimal auto spectral density for the Halsafjorden bridge is shown in Figure 3.2. The figure gives information on for what reduced frequencies the turbulence components are greatest, that is, for what frequency range the fluctuations in the wind flow are largest.

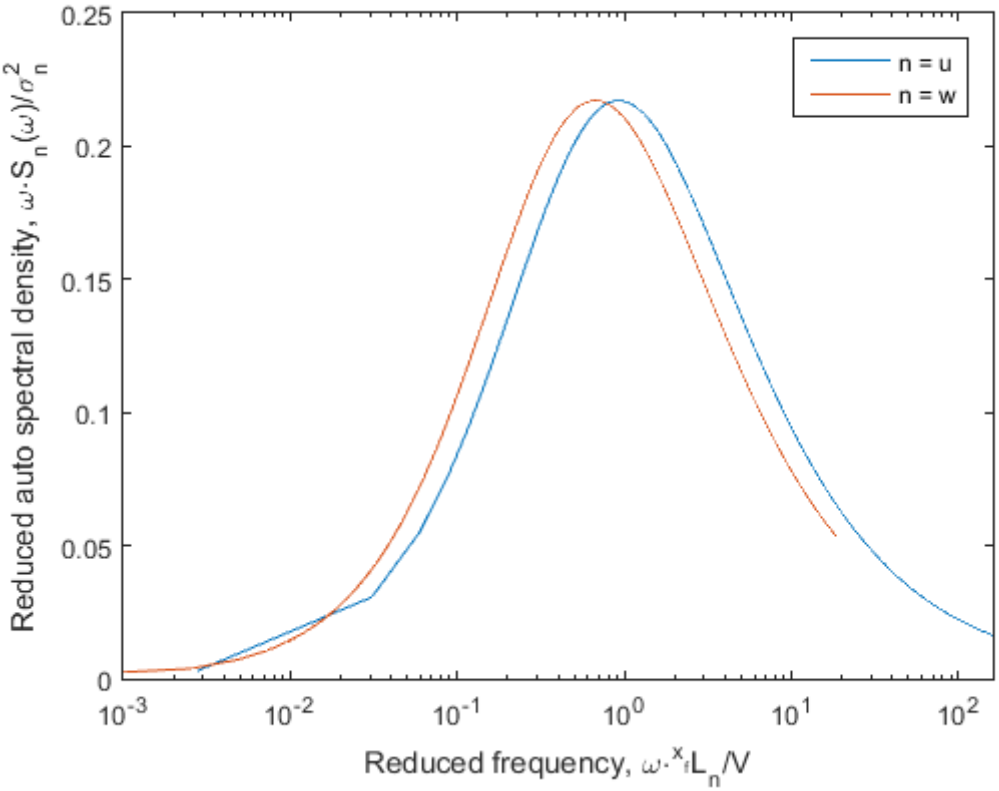

Figure 3.2: Kaimal spectral density of turbulence components

Lastly, the co-spectrum given in Section 2.3.4 may be developed further for the purposes of wind engineering. Assuming homogeneous conditions, a first approximation of the co-spectrum may be adopted as

$$\hat{Co}_{nn}(\Delta x, \omega) \exp\left(-C_{nx}\frac{\omega \Delta x}{V}\right) \qquad \text{where} \quad n = u, v, w \tag{3.10}$$

where $\Delta x = |x_1 - x_2|$ is the separation between two points along the span and C_{nx} are constants.

3.2 Motion Induced Loads

Buffeting wind load is the dynamic load due to turbulence in the oncoming flow, which acts on the structure and causes it to vibrate. For bridge type structures, wind with its main flow direction perpendicular to the bridge span is of most interest. As the wind load acts on the bridge, the bridge starts to move and this bridge motion produces aerodynamic forces which are motion dependent. Hence these additional loads are known as motion induced loads. As a consequence, the aerodynamic forces acting on the bridge are functions of both the incoming turbulence and of the bridge motion [5].
In the following we assume a straight line-like bridge under buffeting wind loading. As the bridge is line-like in the y_f direction it is unnecessary to include the v wind component

which acts along the bridge span and is hence of little consequence. We can assume there are no height variations of the bridge as well as that its z_f position is constant along the entire span before loading, in which case x_f is constant and y_f may be exchanged by x. It is also assumed that d'Alembert's principle may be adopted (see Section 2.1) such that we can take the bridge deck cross section at an instantaneous moment in time and establish dynamic equilibrium. The bridge deck frozen at an instant in time along with the relevant instantaneous flow and displacement quantities is shown in Figure 3.3. The figure shows the deck in three positions. On the bottom left the deck is shown at rest before any loading. After static loading, the deck has displaced to the position shown in the middle of the figure, where $\bar{r}_y$, $\bar{r}_z$ and $\bar{r}_\theta$ are the static displacements the deck has experienced. Around this position the deck will fluctuate. Including the dynamic fluctuations, d'Alembert's principle is applied at the moment in time when the deck is at the top right position in the figure. The deck has now been displaced by $\bar{r}_y + r_y$ in the y-direction, by $\bar{r}_z + r_z$ in the z-direction and rotated by $\bar{r}_\theta + r_\theta$ where r_y, r_z and r_θ are the dynamic displacements [22].

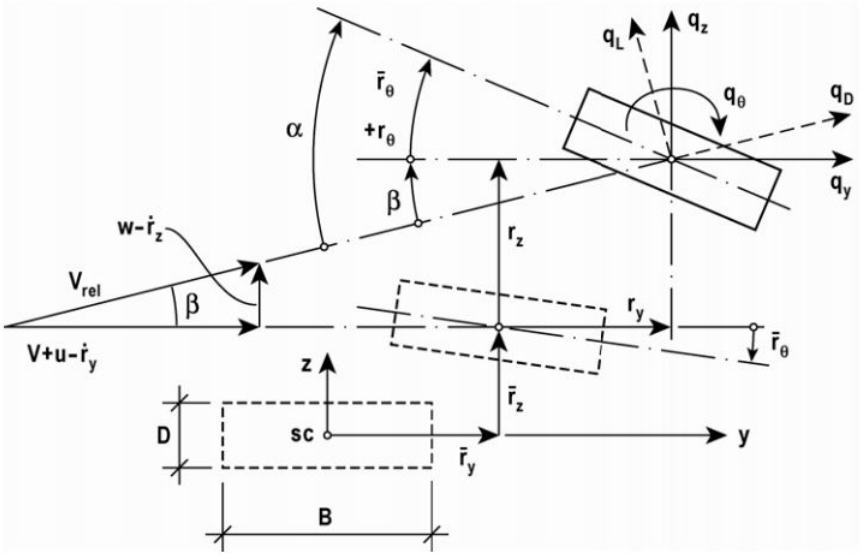

Figure 3.3: Instantaneous flow and displacement quantities [22]

In this final position the instantaneous drag force q_D, lift force q_L and moment force q_M acting on the cross section in flow axes are by definition given by

$$\begin{bmatrix} q_D(x,t) \\ q_L(x,t) \\ q_M(x,t) \end{bmatrix} = \frac{1}{2}\rho V_{rel}^2 \begin{bmatrix} D \cdot C_D(\alpha) \\ B \cdot C_L(\alpha) \\ B^2 \cdot C_M(\alpha) \end{bmatrix} \tag{3.11}$$

where V_{rel} is the relative instantaneous wind velocity, α is the corresponding angle of flow incidence and C_D, C_L and C_M are the drag, lift and moment coefficients. These forces are produced as the wind flows over a given body, where drag acts in the direction of the

flow, lift acts normal to the flow direction and moment acts as a rotation on the body. However, as seen from Figure 3.3, the flow axis does not necessarily coincide with the structural axis, and therefore the loads will need to be transformed into the structural axis by coordinate transformation. The resulting loads are then given in the structural axis by

$$\mathbf{q}_{tot}(x,t) = \begin{bmatrix} q_y \\ q_z \\ q_\theta \end{bmatrix}_{tot} = \begin{bmatrix} cos\beta & -sin\beta & 0 \\ sin\beta & cos\beta & 0 \\ 0 & 0 & 1 \end{bmatrix} \begin{bmatrix} q_D \\ q_L \\ q_M \end{bmatrix} \tag{3.12}$$

where

$$\beta = \arctan\left(\frac{w - \dot{r}_z}{V + u - \dot{r}_y}\right). \tag{3.13}$$

For this theory to be applicable in time domain as well as in frequency domain we apply two linearisation, where we assume that linearisation of any fluctuating parts will render results with sufficient accuracy. The first linearisation is that structural displacements and cross sectional rotations are small, as well as that the fluctuation components $u(x,t)$ and $v(x,t)$ are small as compared to the mean wind velocity V. In this case $cos\beta \approx 1$ and $sin\beta \approx tan\beta \approx \beta$. From Eq. 3.13 we have then that

$$\beta \approx \frac{w - \dot{r}_z}{V + u - \dot{r}_y} \approx \frac{(w - \dot{r}_z)}{V} \tag{3.14}$$

and thus

$$V_{rel}^2 = (V + u - \dot{r}_y)^2 + (w - \dot{r}_z)^2 \approx V^2 + 2Vu - 2V\dot{r}_y \tag{3.15}$$

and

$$\alpha = \bar{r}_\theta + r_\theta + \beta \approx \bar{r}_\theta + r_\theta + \frac{w}{V} - \frac{\dot{r}_z}{V}. \tag{3.16}$$

The second linearisation involves the load coefficients C_D, C_L and C_M. These load coefficients depend on the angle of incidence and the load coefficient curves, shown in Figure 3.4, and they vary non-linearly. As a linearisation, we replace the non-linear curves with the following linear approximation

$$\begin{bmatrix} C_D(\alpha) \\ C_L(\alpha) \\ C_M(\alpha) \end{bmatrix} = \begin{bmatrix} C_D(\bar{\alpha}) \\ C_L(\bar{\alpha}) \\ C_M(\bar{\alpha}) \end{bmatrix} + \alpha_f \cdot \begin{bmatrix} C_D'(\bar{\alpha}) \\ C_L'(\bar{\alpha}) \\ C_M'(\bar{\alpha}) \end{bmatrix} = \begin{bmatrix} \bar{C}_D \\ \bar{C}_L \\ \bar{C}_M \end{bmatrix} + \alpha_f \cdot \begin{bmatrix} C_D' \\ C_L' \\ C_M' \end{bmatrix} \tag{3.17}$$

where $\bar{\alpha}$ and α_f are the mean value and the fluctuating part of the angle of incidence, and C_D', C_L' and C_M' are the slopes of the load coefficient curves at $\bar{\alpha}$.

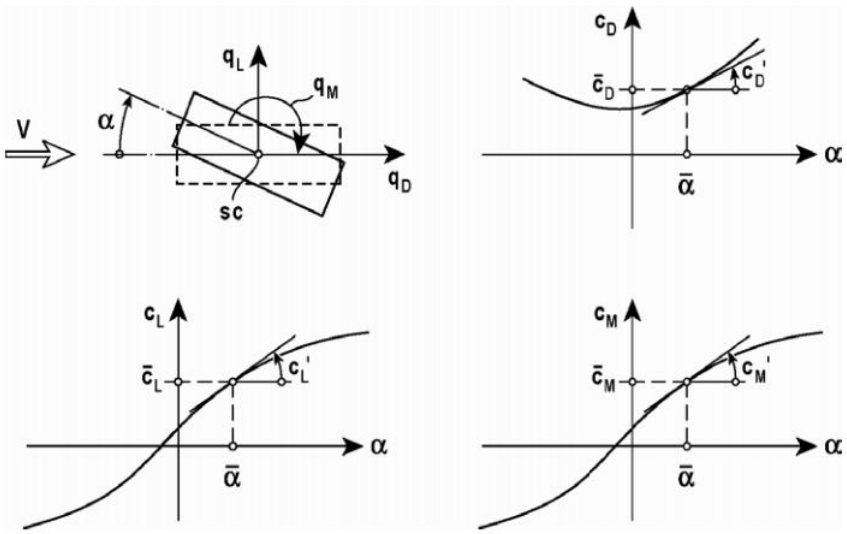

Figure 3.4: Load coefficients obtained from static tests [22]

From Eq. 3.16 we can deduce that $\bar{\alpha} = \bar{r}_\theta$ and $\alpha_f = r_\theta + \frac{w}{V} - \frac{\dot{r}_z}{V}$.
Now, substituting Eq. 3.11 into Eq. 3.12 and applying the first linearisation we get

$$\begin{bmatrix} q_y \\ q_z \\ q_\theta \end{bmatrix}_{tot} = \tfrac{1}{2}\rho V_{rel}^2 \begin{bmatrix} 1 & -\beta & 0 \\ \beta & 1 & 0 \\ 0 & 0 & 1 \end{bmatrix} \begin{bmatrix} D \cdot C_D(\alpha) \\ B \cdot C_L(\alpha) \\ B^2 \cdot C_M(\alpha) \end{bmatrix}$$

$$= \rho V(\tfrac{V}{2} + u - \dot{r}_y) \begin{bmatrix} 1 & -\frac{(w-\dot{r}_z)}{V} & 0 \\ \frac{(w-\dot{r}_z)}{V} & 1 & 0 \\ 0 & 0 & 1 \end{bmatrix} \begin{bmatrix} D \cdot C_D(\alpha) \\ B \cdot C_L(\alpha) \\ B^2 \cdot C_M(\alpha) \end{bmatrix} \tag{3.18}$$

$$= \rho V(\tfrac{V}{2} + u - \dot{r}_y) \begin{bmatrix} D \cdot C_D(\alpha) - \frac{(w-\dot{r}_z)}{V} \cdot B \cdot C_L(\alpha) \\ D \cdot C_D(\alpha) \cdot \frac{(w-\dot{r}_z)}{V} + B \cdot C_L(\alpha) \\ B^2 \cdot C_M(\alpha) \end{bmatrix}$$

Next we apply the second linearisation and obtain

$$\begin{bmatrix} q_y \\ q_z \\ q_\theta \end{bmatrix}_{tot} = \rho V(\frac{V}{2} + u - \dot{r}_y) \left\{ \begin{bmatrix} D\bar{C}_D \\ B\bar{C}_L \\ B^2\bar{C}_M \end{bmatrix} + \left(r_\theta + \frac{w}{V} - \frac{\dot{r}_z}{V} \right) \begin{bmatrix} DC_D' \\ BC_L' \\ B^2 C_M' \end{bmatrix} + \frac{w - \dot{r}_z}{V} \begin{bmatrix} -B\bar{C}_L \\ D\bar{C}_D \\ 0 \end{bmatrix} \right\} \tag{3.19}$$

Discarding all terms containing the product of quantities that have been assumed to be small we are finally left with

$$\mathbf{q}_{tot}\,(x,t) = \begin{bmatrix} \bar{q}_y(x) \\ \bar{q}_z(x) \\ \bar{q}_\theta(x) \end{bmatrix} + \begin{bmatrix} q_y(x,t) \\ q_z(x,t) \\ q_\theta(x,t) \end{bmatrix} = \bar{\mathbf{q}} + \mathbf{B}_q \cdot \mathbf{v} + \mathbf{C}_{ae} \cdot \dot{\mathbf{r}} + \mathbf{K}_{ae} \cdot \mathbf{r} \tag{3.20}$$

where

$$\mathbf{v}(x,t) = \begin{bmatrix} u & w \end{bmatrix}^T \tag{3.21}$$

$$\mathbf{r}(x,t) = \begin{bmatrix} r_y & r_z & r_\theta \end{bmatrix}^T \tag{3.22}$$

$$\bar{\mathbf{q}}(x) = \begin{bmatrix} \bar{q}_y(x) \\ \bar{q}_z(x) \\ \bar{q}_\theta(x) \end{bmatrix} = \frac{\rho V^2 B}{2} \begin{bmatrix} (D/B)\bar{C}_D \\ \bar{C}_L \\ B\bar{C}_M \end{bmatrix} = \frac{\rho V^2 B}{2} \cdot \hat{\mathbf{b}}_q \tag{3.23}$$

$$\mathbf{B}_q(x) = \frac{\rho V B}{2} \begin{bmatrix} 2(D/B)\bar{C}_D & \left((D/B)C_D' - \bar{C}_L\right) \\ 2\bar{C}_L & \left(C_L' + (D/B)\bar{C}_D\right) \\ 2B\bar{C}_M & BC_M' \end{bmatrix} = \frac{\rho V B}{2} \cdot \hat{\mathbf{B}}_q \tag{3.24}$$

$$\mathbf{C}_{ae}(x) = -\frac{\rho V B}{2} \begin{bmatrix} 2(D/B)\bar{C}_D & \left((D/B)C_D' - \bar{C}_L\right) & 0 \\ 2\bar{C}_L & \left(C_L' + (D/B)\bar{C}_D\right) & 0 \\ 2B\bar{C}_M & BC_M' & 0 \end{bmatrix} \tag{3.25}$$

$$\mathbf{K}_{ae}(x) = \frac{\rho V^2 B}{2} \begin{bmatrix} 0 & 0 & (D/B)C_D' \\ 0 & 0 & C_L' \\ 0 & 0 & BC_M' \end{bmatrix} \tag{3.26}$$

It should be noted that $\bar{\mathbf{q}}$ is the static load, $\mathbf{B}_q \cdot \mathbf{v}$ is the buffeting load (dynamic loading associated with turbulence in the oncoming flow), while $\mathbf{C}_{ae} \cdot \dot{\mathbf{r}}$ and $\mathbf{K}_{ae} \cdot \mathbf{r}$ are the motion induced loads associated with structural velocity and displacement . The $\mathbf{K}_{ae}$ matrix can change the total stiffness of the combined structure and flow system while $\mathbf{C}_{ae}$ can change the damping of the system. This means that the resonance frequency at $V \neq 0$ will be different than that in still air, at $V = 0$. $\mathbf{C}_{ae}$, $\mathbf{K}_{ae}$ and $\mathbf{M}_{ae}$ are known as the motion dependent cross sectional load coefficient matrices. The oncoming flow does not cause changes in the mass, so $\mathbf{M}_{ae}$ is negligible in this case [22].

3.3 Wind Tunnel Testing

Wind tunnel testing is an integral part of the aerodynamic design of a suspension bridge, since the wind load depends both on the dimensions of the deck as well as its shape. For long suspension bridges, their high flexibility makes them particularly vulnerable to aerodynamic instability (see section 3.7), which makes wind tunnel testing all the

more important. These tests are performed to identify the aerodynamic and aeroelastic behaviour of the different bridge components, and optimize the shape of the deck. Usually tests are performed in a smaller model scale on the individual components of the bridge (the deck, tower and cables), and subsequently on a full aeroelastic bridge model.
The general procedure for tests of the bridge deck is as follows [5]:

1) Static tests are performed on a sectional model of the deck to measure the drag, lift and moment coefficients C_D, C_L and C_M as a function of the angle of incidence α. The model is placed on a dynamometric system and allowed to rotate around the deck longitudinal axis. The load coefficients are then measured as a function of the wind angle of attack by changing the rotational angle of the deck.

2) The deck shape is optimized in order to fulfil the bridge stability requirements. By analysing the slopes of the load coefficients obtained in the static test, the deck shape can be designed to fulfil the stability requirements. These requirements are covered in more detail in Section 3.7.

3) Verification of that vortex shedding excitation of the deck is controlled. If it is not, the deck optimization must be repeated.

4) Dynamic tests in order to identify the aerodynamic derivatives (see Section 3.4) and extract the motion induced forces. Two methods currently in use are the free motion method and the forced method. During free motion tests the deck sectional model is allowed to vibrate freely under the mean wind speed action, the response of the system is measured and the aerodynamic derivatives are extracted by computing the variation of the structural response at a given wind velocity as compared to the values obtained in still air. The forced motion method is more expensive but more reliable. The deck is forced to vibrate in the y, z and θ directions at various frequencies, while the motion induced forces are measured for a given constant velocity.

3.4 Aerodynamic derivatives

The coefficients of the $\mathbf{C}_{ae}$ and $\mathbf{K}_{ae}$ matrices derived in Section 3.2 are better known as aerodynamic derivatives. Together, these eighteen coefficients give a full frequency domain description of motion induced dynamic forces associated with structural velocity and displacement. That is, they describe the wind flow around a given cross section. As such they are functions of the type of cross section and its dimensions, as well as the mean wind velocity and the frequency of motion. The main use for these aerodynamic derivatives is in the detection of unstable motion at high wind velocities. Usually they have to be experimentally determined in wind tunnel tests for a given cross section,

as was covered in the previous section. These tests have the limitation that the along wind motion is absent in the section model, and thus the experiments are limited to vertical and torsion displacements. The wind tunnel tests are performed at a smaller model scale and hence it must be possible to accurately convert the results to full scale. This means that the aerodynamic derivatives have to be extracted as functions of the reduced velocity $\hat{V} = V/(B\omega_i)$ where ω_i is the in-wind eigenfrequency associated with mode shape i. As previously mentioned, $\mathbf{C}_{ae}$ and $\mathbf{K}_{ae}$ can reduce the total damping and stiffness of the system and therefore it follows that the eigenfrequencies ω_i of the system will also be changed. However, in the quantification of the aerodynamic derivatives and their contribution to the total stiffness and damping it is assumed that the changes in the eigenfrequencies may be ignored [22]. The coefficients included in $\mathbf{C}_{ae}$ and $\mathbf{K}_{ae}$ are most commonly notated as follows

$$\mathbf{C}_{ae} = \begin{bmatrix} P_1 & P_5 & P_2 \\ H_5 & H_1 & H_2 \\ A_5 & A_1 & A_2 \end{bmatrix} \quad \text{and} \quad \mathbf{K}_{ae} = \begin{bmatrix} P_4 & P_6 & P_3 \\ H_6 & H_4 & H_3 \\ A_6 & A_4 & A_3 \end{bmatrix} \tag{3.27}$$

It has been considered convenient to normalize $\mathbf{C}_{ae}$ and $\mathbf{K}_{ae}$ with $\rho B^2\omega_i/2$ and $\rho B^2\omega_i^2/2$ into a non-dimensional form, such that

$$\mathbf{C}_{ae} = \frac{\rho B^2}{2} \cdot \omega_i(V) \cdot \hat{\mathbf{C}}_{ae} \quad \text{and} \quad \mathbf{K}_{ae} = \frac{\rho B^2}{2} \cdot [\omega_i(V)]^2 \cdot \hat{\mathbf{K}}_{ae} \tag{3.28}$$

where

$$\hat{\mathbf{C}}_{ae} = \begin{bmatrix} P_1^* & P_5^* & BP_2^* \\ H_5^* & H_1^* & BH_2^* \\ BA_5^* & BA_1^* & B^2A_2^* \end{bmatrix} \quad \text{and} \quad \hat{\mathbf{K}}_{ae} = \begin{bmatrix} P_4^* & P_6^* & BP_3^* \\ H_6^* & H_4^* & BH_3^* \\ BA_6^* & BA_4^* & B^2A_3^* \end{bmatrix} \tag{3.29}$$

It is these non-dimensional coefficients that are usually called aerodynamic derivatives. Comparing the notation of Eq. 3.28 and Eq. 3.29 with Eq. 3.25 and Eq. 3.26 and remembering that the aerodynamic derivatives were extracted as functions of $V/(B\omega_i)$, we get the quasi-static aerodynamic derivatives

$$\begin{bmatrix} P_1^* & H_1^* & A_1^* \\ P_2^* & H_2^* & A_2^* \\ P_3^* & H_3^* & A_3^* \\ P_4^* & H_4^* & A_4^* \\ P_5^* & H_5^* & A_5^* \\ P_6^* & H_6^* & A_6^* \end{bmatrix} = \begin{bmatrix} -2\bar{C}_D\frac{D}{B}\frac{V}{B\omega_i(V)} & -\left(C_L' + \bar{C}_D\frac{D}{B}\right)\frac{V}{B\omega_i(V)} & -C_M'\frac{V}{B\omega_i(V)} \\ 0 & 0 & 0 \\ C_D'\frac{D}{B}\left(\frac{V}{B\omega_i(V)}\right)^2 & C_L'\left(\frac{V}{B\omega_i(V)}\right)^2 & C_M'\left(\frac{V}{B\omega_i(V)}\right)^2 \\ 0 & 0 & 0 \\ \left(\bar{C}_L - C_D'\frac{D}{B}\right)\frac{V}{B\omega_i(V)} & -2\bar{C}_L\frac{V}{B\omega_i(V)} & -2\bar{C}_M\frac{V}{B\omega_i(V)} \\ 0 & 0 & 0 \end{bmatrix} \tag{3.30}$$

The choice of normalizing the aerodynamic derivatives with $\omega_y(V)$, $\omega_z(V)$ or $\omega_\theta(V)$ is optional, as the frequency ratio stays the same both in the model and full scale regardless. In this thesis it has been chosen to have normalized H_i^* with $\omega_z(V)$ and A_i^* with $\omega_\theta(V)$, where $i = 1 - 4$. Quantifying P_i^* is obsolete since it associated to drag, and y direction response is not of relevance for the purposes of this thesis.
Aerodynamic derivatives for the specific case of an ideal flat plate type of cross section are often used as a reference. They are given by

$$\begin{bmatrix} H_1^* & A_1^* \\ H_2^* & A_2^* \\ H_3^* & A_3^* \\ H_4^* & A_4^* \end{bmatrix} = \begin{bmatrix} -2\pi F\hat{V}_i & -\frac{\pi}{2}F\hat{V}_i \\ \frac{\pi}{2}\left(1 + F + 4G\hat{V}_i\right)\hat{V}_i & -\frac{\pi}{8}\left(1 - F - 4G\hat{V}_i\right)\hat{V}_i \\ 2\pi\left(F\hat{V}_i - G/4\right)\hat{V}_i & \frac{\pi}{2}\left(F\hat{V}_i - G/4\right)\hat{V}_i \\ \frac{\pi}{2}\left(1 + 4G\hat{V}_i\right) & \frac{\pi}{2}G\hat{V}_i \end{bmatrix} \tag{3.31}$$

where $\hat{V}_i = V/\left[B\omega_i\left(V\right)\right]$ and F and G are the real and imaginary parts of Theodorsen's circulatory function, given by

$$F\left(\frac{\hat{\omega}_i}{2}\right) = \frac{J_1 \cdot (J_1 + Y_0) + Y_1 \cdot (Y_1 - J_0)}{(J_1 + Y_0)^2 + (Y_1 - J_0)^2} \tag{3.32}$$

$$G\left(\frac{\hat{\omega}_i}{2}\right) = -\frac{J_1 \cdot J_0 + Y_1 \cdot Y_1}{(J_1 + Y_0)^2 + (Y_1 - J_0)^2} \tag{3.33}$$

J_n and Y_n $(n = 0, 1)$ used in this function are Bessel functions of the first and second kinds. $\hat{\omega}_i$ is the non-dimensional resonance frequency, $\hat{\omega}_i = B\omega_i(V)/V = \hat{V}^{-1}$. The aerodynamic derivatives associated with the along-wind direction are notably absent in the section model for a flat plate. They have been disregarded due to the limitations of wind tunnel testing, however these components are of minor importance for bridges with this type of cross section [22].

3.5 Modal Frequency Response Function

The aim of this section is to derive the modal equivalent of the frequency response function given by Eq. 2.14 with motion induced loads included. Starting from the modal dynamic equilibrium equation for mode number i

$$\tilde{M}_i \cdot \ddot{\eta}_i(t) + \tilde{C}_i \cdot \dot{\eta}_i(t) + \tilde{K}_i \cdot \eta_i(t) = \tilde{Q}_i(t) + \tilde{Q}_{ae_i}(t, \eta_i, \dot{\eta}_i, \ddot{\eta}_i) \tag{3.34}$$

where

$$\begin{bmatrix} \tilde{Q}_i(t) \\ \tilde{Q}_{ae_i}(t, \eta_i, \dot{\eta}_i, \ddot{\eta}_i) \end{bmatrix} = \int_{L_{exp}} \phi_i \cdot \begin{bmatrix} q \\ q_{ae} \end{bmatrix} dx \tag{3.35}$$

L_{exp} is the flow exposed part of the structure and $\tilde{Q}_{ae_i}$ is the modal motion induced load. To transfer this expression into the frequency domain we take the Fourier transform on both sides of the equation,

$$\begin{aligned} \eta_i(t) &= a_{\eta_i}(\omega) \cdot e^{i\omega t} \\ \tilde{Q}_i(t) &= a_{\tilde{Q}_i}(\omega) \cdot e^{i\omega t} \\ \tilde{Q}_{ae_i}(t) &= a_{\tilde{Q}ae_i}(\omega, \eta_i, \dot{\eta}_i, \ddot{\eta}_i) \cdot e^{i\omega t} \end{aligned} \tag{3.36}$$

which gives

$$\left(-\tilde{M}_i \cdot \omega^2 + \tilde{C}_i \cdot i\omega + \tilde{K}_i\right) \cdot a_{\eta_i}(\omega) = a_{\tilde{Q}_i}(\omega) + a_{\tilde{Q}ae_i}(\omega, \eta_i, \dot{\eta}_i, \ddot{\eta}_i) \tag{3.37}$$

where a_{η_i}, $a_{\tilde{Q}_i}$ and $a_{\tilde{Q}ae_i}$ are Fourier amplitudes. It is assumed that

$$a_{\tilde{Q}ae_i} = \left(-\tilde{M}_{ae_i} \cdot \omega^2 + \tilde{C}_{ae_i} \cdot i\omega + \tilde{K}_{ae_i}\right) \cdot a_{\eta_i}(\omega) \tag{3.38}$$

i.e. includes the motion induced part of the modal mass, stiffness and damping of the system. Substituting Eq. 3.38, into Eq. 3.37, we obtain

$$\begin{aligned} &\left(-\tilde{M}_i \cdot \omega^2 + \tilde{C}_i \cdot i\omega + \tilde{K}_i\right) \cdot a_{\eta_i}(\omega) = a_{\tilde{Q}_i}(\omega) + \left(-\tilde{M}_{ae_i} \cdot \omega^2 + \tilde{C}_{ae_i} \cdot i\omega + \tilde{K}_{ae_i}\right) \cdot a_{\eta_i}(\omega) \\ &\Rightarrow \left(-\left(\tilde{M}_i - \tilde{M}_{ae_i}\right)\omega^2 + \left(\tilde{C}_i - \tilde{C}_{ae_i}\right) \cdot i\omega + \left(\tilde{K}_i - \tilde{K}_{ae_i}\right)\right) \cdot a_{\eta_i}(\omega) = a_{\tilde{Q}_i}(\omega) \end{aligned} \tag{3.39}$$

Dividing through the equation with $\tilde{K}_i$ and substituting Eq. 2.42 and Eq. 2.43 gives after some simplifications

$$a_{\eta_i}(\omega) = \hat{H}_i(\omega) \cdot \frac{1}{\tilde{K}_i} \cdot a_{\tilde{Q}_i}(\omega) \tag{3.40}$$

where

$$\hat{H}_i(\omega) = \left[1 - \frac{\tilde{K}_{ae_i}}{\omega_i^2 \tilde{M}_i} - \left(1 - \frac{\tilde{M}_{ae_i}}{\tilde{M}_i}\right) \cdot \left(\frac{\omega}{\omega_i}\right)^2 + 2i\left(\zeta_i - \frac{\tilde{C}_{ae_i}}{2\omega_i \tilde{M}_i}\right) \cdot \frac{\omega}{\omega_i}\right]^{-1} \tag{3.41}$$

is the non-dimensional modal frequency response function. Finally, introducing $\mu_{ae_i} = \tilde{M}_{ae_i}/\tilde{M}_i$, $\kappa_{ae_i} = \tilde{K}_{ae_i}/\omega_i^2 \tilde{M}_i$ and $\zeta_{ae_i} = \tilde{C}_{ae_i}/\left(2\omega_i \tilde{M}_i\right)$, then

$$\hat{H}_i(\omega) = \left[1 - \kappa_{ae_i} - (1 - \mu_{ae_i}) \cdot \left(\frac{\omega}{\omega_i}\right)^2 + 2i\left(\zeta_i - \zeta_{ae_i}\right) \cdot \frac{\omega}{\omega_i}\right]^{-1} \tag{3.42}$$

The corresponding multi-mode form of the modal frequency response function is given by [22], taking full motion induced load effects:

$$\hat{\mathbf{H}}(\omega) = \left\{ \mathbf{I} - \boldsymbol{\kappa}_{ae} - \left(\omega \cdot diag \left[\frac{1}{\omega_i} \right] \right)^2 (\mathbf{I} - \boldsymbol{\mu}_{ae}) + 2i\omega \cdot diag \left[\frac{1}{\omega_i} \right] (\boldsymbol{\zeta} - \boldsymbol{\zeta}_{ae}) \right\}^{-1} \tag{3.43}$$

where

$$\boldsymbol{\mu}_{ae} = \begin{bmatrix} \ddots & & \iddots \\ & \mu_{ae_{ij}} & \\ \iddots & & \ddots \end{bmatrix} \quad \boldsymbol{\kappa}_{ae} = \begin{bmatrix} \ddots & & \iddots \\ & \kappa_{ae_{ij}} & \\ \iddots & & \ddots \end{bmatrix} \quad \boldsymbol{\zeta}_{ae} = \begin{bmatrix} \ddots & & \iddots \\ & \zeta_{ae_{ij}} & \\ \iddots & & \ddots \end{bmatrix} \tag{3.44}$$

are given by

$$\mu_{ae_{ij}} = \frac{\tilde{M}_{ae_{ij}}}{\tilde{M}_i} = \frac{\int_{L_{exp}} \left(\boldsymbol{\varphi}_i^T \mathbf{M}_{ae} \boldsymbol{\varphi}_j \right) dx}{\tilde{M}_i} = \frac{\rho B^2}{2\tilde{m}_i} \cdot \frac{\int_{L_{exp}} \left(\boldsymbol{\varphi}_i^T \hat{\mathbf{M}}_{ae} \boldsymbol{\varphi}_j \right) dx}{\int_L \left(\boldsymbol{\varphi}_i^T \boldsymbol{\varphi}_i \right) dx} \tag{3.45}$$

$$\kappa_{ae_{ij}} = \frac{\tilde{K}_{ae_{ij}}}{\omega_i^2 \tilde{M}_i} = \frac{\int_{L_{exp}} \left(\boldsymbol{\varphi}_i^T \mathbf{K}_{ae} \boldsymbol{\varphi}_j \right) dx}{\omega_i^2 \tilde{M}_i} = \frac{\rho B^2}{2\tilde{m}_i} \cdot \left[\frac{\omega_i(V)}{\omega_i} \right]^2 \frac{\int_{L_{exp}} \left(\boldsymbol{\varphi}_i^T \hat{\mathbf{K}}_{ae} \boldsymbol{\varphi}_j \right) dx}{\int_L \left(\boldsymbol{\varphi}_i^T \boldsymbol{\varphi}_i \right) dx} \tag{3.46}$$

$$\zeta_{ae_{ij}} = \frac{\tilde{C}_{ae_{ij}}}{2\omega_i \tilde{M}_i} = \frac{\rho B^2}{4\tilde{m}_i} \cdot \frac{\omega_i(V)}{\omega_i} \cdot \frac{\int_{L_{exp}} \left(\boldsymbol{\varphi}_i^T \hat{\mathbf{C}}_{ae} \boldsymbol{\varphi}_j \right) dx}{\int_L \left(\boldsymbol{\varphi}_i^T \boldsymbol{\varphi}_i \right) dx} \tag{3.47}$$

where $\omega_i(V)$ is the mean wind velocity dependent resonance frequency associated with mode i, $\omega_i = \omega_i(V = 0)$ is the mean wind velocity as calculated in still-air conditions and $\tilde{m}_i = \tilde{M}_i / \int_L \left(\boldsymbol{\varphi}_i^T \cdot \boldsymbol{\varphi}_i \right) dx$ is the modally equivalent and evenly distributed mass.

3.6 Response Calculations

This section gives a general solution strategy for calculation of the dynamic response due to wind loading, as presented by [22]. Three methods can be used for obtaining the solution. First, if eigenmodes are well separated and, hence there is no significant coupling between displacement components, a single mode single component response solution will render a sufficiently accurate solution. Second, a single mode three component response solution may be used when there is significant coupling between modes, yet they are still well separated. Lastly, a general multi-mode approach does not require the modes to be either uncoupled or far apart and can be used for all cases. For the sake of generality, only the multi-mode approach will be presented here, as the two other cases are nothing but special cases of this general method.

The solution method is pursued in modal coordinates (see Section 2.3.2) and in the fre-

quency domain (see Section 2.1.2). The solution is given in frequency domain as the spectral density of the response, where

$$\mathbf{S}_{rr}(x_r,\omega) = \begin{bmatrix} S_{r_y r_y} & S_{r_y r_z} & S_{r_y r_\theta} \\ S_{r_z r_y} & S_{r_z r_z} & S_{r_z r_\theta} \\ S_{r_\theta r_y} & S_{r_\theta r_z} & S_{r_\theta r_\theta} \end{bmatrix} \tag{3.48}$$

is the cross spectral density matrix of the unknown modal displacements r_y, r_z and r_θ. Here, the spectral density of the response has been converted from modal coordinates into original coordinates by

$$\mathbf{S}_{rr}(x_r,\omega) = \mathbf{\Phi}_r(x_r) \cdot \mathbf{S}_\eta(\omega) \cdot \mathbf{\Phi}_r^T(x_r) \tag{3.49}$$

where $\mathbf{S}_\eta(\omega)$ is the response spectral density in modal coordinates, given by

$$\begin{aligned} \mathbf{S}_\eta(\omega) = \lim_{T\to\infty} \frac{1}{\pi T}\left(\mathbf{a}_\eta^* \cdot \mathbf{a}_\eta^T\right) &= \lim_{T\to\infty} \frac{1}{\pi T}\left(\left(\hat{\mathbf{H}}_\eta \mathbf{a}_{\hat{Q}}\right)^* \cdot \left(\hat{\mathbf{H}}_\eta \mathbf{a}_{\hat{Q}}\right)^T\right) \\ &= \hat{\mathbf{H}}_\eta \cdot \left[\lim_{T\to\infty} \frac{1}{\pi T}\left(\mathbf{a}_{\hat{Q}}^* \cdot \mathbf{a}_{\hat{Q}}^T\right)\right] \cdot \hat{\mathbf{H}}_\eta^T = \hat{\mathbf{H}}_\eta^* \cdot \mathbf{S}_{\hat{Q}} \cdot \hat{\mathbf{H}}_\eta^T \end{aligned}$$

where $\mathbf{S}_{\hat{Q}}(\omega)$ is the spectral density of the modal load defined by

$$\mathbf{S}_{\hat{Q}}(\omega) = \lim_{T\to\infty} \frac{1}{\pi T}\left(\mathbf{a}_{\hat{Q}}^* \cdot \mathbf{a}_{\hat{Q}}^T\right) \tag{3.50}$$

The response spectral density can be converted to the time domain by frequency domain integration. There the solution is given by the covariance matrix, containing the time domain variances and covariances of each response displacement component r_y, r_z and r_θ. The covariance matrix is given by

$$\mathbf{Cov}_{rr}(x_r) = \begin{bmatrix} \sigma^2_{r_y r_y} & Cov_{r_y r_z} & Cov_{r_y r_\theta} \\ Cov_{r_z r_y} & \sigma^2_{r_z r_z} & Cov_{r_z r_\theta} \\ Cov_{r_\theta r_y} & Cov_{r_\theta r_z} & \sigma^2_{r_\theta r_\theta} \end{bmatrix} \tag{3.51}$$

which is obtained by frequency domain integration,

$$\mathbf{Cov}_{rr}(x_r) = \int_0^\infty \mathbf{S}_{rr}(x_r,\omega)d\omega = \mathbf{\Phi}_r(x_r)\left[\int_0^\infty \hat{\mathbf{H}}_\eta^*(\omega)\mathbf{S}_{\hat{Q}}(\omega)\hat{\mathbf{H}}_\eta^T(\omega)d\omega\right]\mathbf{\Phi}_r^T(x_r) \tag{3.52}$$

where $\hat{\mathbf{H}}_\eta(\omega)$ is as given in Eq. 3.43 and $\mathbf{\Phi}_r(x_r)$ is the mode shape matrix given in Eq. 2.32.

The content of the normalised modal load matrix $\mathbf{S}_{\hat{Q}}(\omega)$ is given by

$$S_{\hat{Q}_i\hat{Q}_j}(\omega) = \frac{\rho B^3}{2\tilde{m}_i} \cdot \frac{\rho B^3}{2\tilde{m}_j} \cdot \left(\frac{V}{B\omega_i}\right)^2 \cdot \left(\frac{V}{B\omega_j}\right)^2 \cdot \hat{J}_{ij}^2 \tag{3.53}$$

where $\hat{J}_{ij}^2$ is known as the reduced joint acceptance function. In wind engineering, this function is used to quantify the ability of the wind loading to excite the mode considered. The function contains the span-wise statistical averaging of variance contributions from the fluctuating wind flow components, i.e. it accounts for variations of the wind velocity over the length of the mode. Theoretically, if the joint acceptance function equals 1, the wind velocity is the same over the span of the bridge. Close to 0, the span-wise deviations in wind velocity are great. The reduced joint acceptance function is given by [21]

$$\hat{J}_{ij}^2 = \frac{\iint_{L_{exp}} \boldsymbol{\varphi}_i^T(x_1) \cdot \left\{\hat{\mathbf{B}}_q \cdot \left[\mathbf{I}_v^2 \cdot \hat{\mathbf{S}}_v(\Delta x, \omega)\right] \cdot \hat{\mathbf{B}}_q^T\right\} \cdot \boldsymbol{\varphi}_j(x_2) dx_1 dx_2}{\left(\int_L \boldsymbol{\varphi}_i^T \cdot \boldsymbol{\varphi}_i dx\right) \cdot \left(\int_L \boldsymbol{\varphi}_j^T \cdot \boldsymbol{\varphi}_j dx\right)} \tag{3.54}$$

where

$$\mathbf{I}_v = diag\begin{bmatrix} I_u & I_w \end{bmatrix} \tag{3.55}$$

$$\hat{\mathbf{S}}_v = diag\begin{bmatrix} S_{uu}/\sigma_u^2 & S_{ww}/\sigma_w^2 \end{bmatrix} \tag{3.56}$$

and $\hat{\mathbf{B}}_q$ has previously been defined in Eq. 3.24.

3.7 Stability

As the mean wind load acting on a structure increases, the response of the structure will generally increase as well. As high wind velocities are reached, motion induced forces may reduce the total stiffness of the combined structure and flow system. After these motion induced load effects start occurring, a certain critical mean wind velocity limit may be reached, at which point the dynamic response curve will rapidly increase for a small increase in the wind velocity until it approaches infinity. This is known as a stability limit, and is shown in Figure 3.5. The number of stability limits in a system is equal to the number of modes that system has, where each stability limit is associated with a corresponding mode shape.

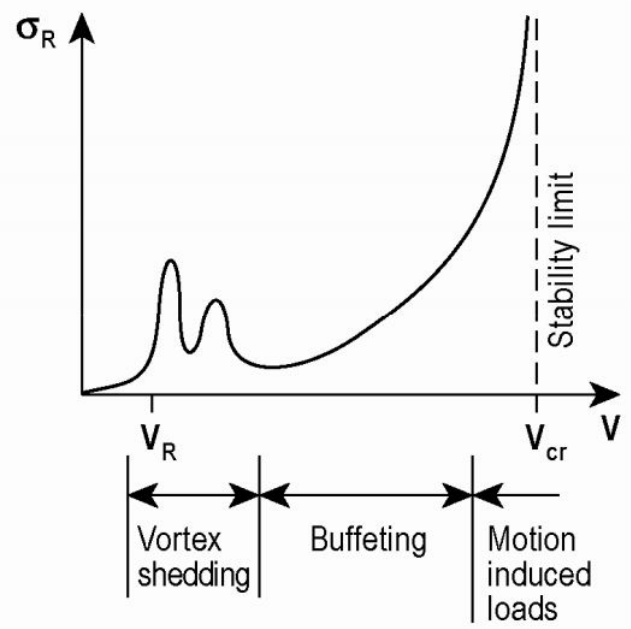

Figure 3.5: Relationship between structural response and mean wind velocity [22]

As the structural displacement response approaches infinity, so does the frequency response function in Eq. 3.43. It follows that its inverse, known as the impedance matrix $\hat{\mathbf{E}}$, will approach zero at this point. Therefore we can define the stability limit where both the real and the imaginary part of the non-dimensional impedance matrix is zero, i.e. where

$$\begin{gathered} \left|\det\left(\hat{\mathbf{E}}\left(\omega, V\right)\right)\right| = 0 \\ \Rightarrow \mathrm{Re}\left(\det\left(\hat{\mathbf{E}}\left(\omega, V\right)\right)\right) = 0 \qquad \text{and} \qquad \mathrm{Im}\left(\det\left(\hat{\mathbf{E}}\left(\omega, V\right)\right)\right) = 0 \end{gathered} \tag{3.57}$$

and $\hat{\mathbf{E}}\left(\omega, V\right)$ is given as

$$\hat{\mathbf{E}}(\omega, V) = \left\{\mathbf{I} - \boldsymbol{\kappa}_{ae} - \left(\omega \cdot diag\left[\frac{1}{\omega_i}\right]\right)^2 + 2i\omega \cdot diag\left[\frac{1}{\omega_i}\right](\boldsymbol{\zeta} - \boldsymbol{\zeta}_{ae})\right\} \tag{3.58}$$

where any aerodynamic mass effects have been neglected. The effect of $\boldsymbol{\kappa}_{ae}$ is to change the stiffness properties of the system, while $\boldsymbol{\zeta}_{ae}$ affects the system by changing its damping properties. For a two-mode approach, their contents are as follows:

$$\boldsymbol{\kappa}_{ae} = \begin{bmatrix} \kappa_{ae_{zz}} & \kappa_{ae_{z\theta}} \\ \kappa_{ae_{\theta z}} & \kappa_{ae_{\theta\theta}} \end{bmatrix} \qquad \text{and} \qquad \boldsymbol{\zeta}_{ae} = \begin{bmatrix} \zeta_{ae_{zz}} & \zeta_{ae_{z\theta}} \\ \zeta_{ae_{\theta z}} & \zeta_{ae_{\theta\theta}} \end{bmatrix} \tag{3.59}$$

where

$$\kappa_{ae_{zz}} = \frac{\rho B^2}{2\tilde{m}_z} H_4^* \frac{\int_{L_{exp}} \phi_z^2 dx}{\int_L \phi_z^2 dx} \qquad \kappa_{ae_{z\theta}} = \frac{\rho B^3}{2\tilde{m}_z} H_3^* \frac{\int_{L_{exp}} \phi_z \phi_\theta dx}{\int_L \phi_z^2 dx} \tag{3.60}$$

$$\kappa_{ae_{\theta z}} = \frac{\rho B^3}{2\tilde{m}_\theta} A_4^* \frac{\int_{L_{exp}} \phi_\theta \phi_z dx}{\int_L \phi_\theta^2 dx} \qquad \kappa_{ae_{\theta\theta}} = \frac{\rho B^4}{2\tilde{m}_\theta} A_3^* \frac{\int_{L_{exp}} \phi_\theta^2 dx}{\int_L \phi_\theta^2 dx} \tag{3.61}$$

$$\zeta_{ae_{zz}} = \frac{\rho B^2}{4\tilde{m}_z} H_1^* \frac{\int_{L_{exp}} \phi_z^2 dx}{\int_L \phi_z^2 dx} \qquad \zeta_{ae_{z\theta}} = \frac{\rho B^3}{4\tilde{m}_z} H_2^* \frac{\int_{L_{exp}} \phi_z \phi_\theta dx}{\int_L \phi_z^2 dx} \tag{3.62}$$

$$\zeta_{ae_{\theta z}} = \frac{\rho B^3}{4\tilde{m}_\theta} A_1^* \frac{\int_{L_{exp}} \phi_\theta \phi_z dx}{\int_L \phi_\theta^2 dx} \qquad \zeta_{ae_{\theta\theta}} = \frac{\rho B^4}{4\tilde{m}_\theta} A_2^* \frac{\int_{L_{exp}} \phi_\theta^2 dx}{\int_L \phi_\theta^2 dx} \tag{3.63}$$

While in Section 3.4 we assumed changes to the resonance frequencies were negligible, close to an instability limit the motion induced load effect of changing the system's eigenfrequencies ω_i can no longer be ignored, and ω_i will be taken at the relevant critical wind velocity V_{cr}. As such the impedance matrix depends both on the mean wind velocity as well as the frequency of motion and the determination of V_{cr} will require iterations.
The solution to Eq. 3.57 is an eigenvalue problem, each representing a stability limit. Of all the eigenvalues that can be extracted from the equation, it is the lowest one that is most important for design of structures, giving the lowest V_{cr} and corresponding in-wind resonance frequency ω_r. It should be noted that that this is not the only method of identifying stability limits. Another method is to calculate the dynamic response of the structure over the wind velocity range, and identifying where the response starts to rapidly approach infinity.
There are four types of unstable behaviour of a bridge section, characterized either by vertical motion, torsional motion or a combination of both. Since it is the lowest eigenmodes that are of most importance and the fact that unstable behaviour of bridges only depends on r_z and r_θ, it is sufficient to search only for the stability limits associated with the lowest vertical and torsional modes, $\boldsymbol{\varphi}_1 \approx \begin{bmatrix} 0 & \phi_z & 0 \end{bmatrix}_1^T$ and $\boldsymbol{\varphi}_2 \approx \begin{bmatrix} 0 & 0 & \phi_\theta \end{bmatrix}_2^T$. The possible types of unstable behaviour of a bridge section will be described in the following subsections. All these descriptions are obtained from [22].

3.7.1 Static divergence

Static divergence is a static type of instability governed by torsional frequency and the slope of the moment coefficient C'_M. It can occur when the predominant mode shape is torsional and is as such a problem of losing torsion stiffness due to interaction effects with the air flow. Since $\omega = \omega_r = 0$ for static problems, and the only mode shape to be considered is $\boldsymbol{\varphi}_2 \approx \begin{bmatrix} 0 & 0 & \phi_\theta \end{bmatrix}^T$, the impedance matrix from Eq. 3.58 is reduced to the simple form

$$\hat{E}_\eta \left(\omega_r = 0, V_{cr}\right) = 1 - \kappa_{ae_{\theta\theta}} \tag{3.64}$$

As described above, instabilities occur when $\hat{E}_\eta = 0$. It follows that static divergence will

occur when $\kappa_{ae_{\theta\theta}} = 1$. Substituting the quasi-static expression for A_3^* from Eq. 3.30 into the expression for $\kappa_{ae_{\theta\theta}}$ (Eq. 3.61) and equating to 1, we get

$$\frac{\rho B^4}{2\tilde{m}_\theta}\left(\frac{\omega_\theta(V_{cr})}{\omega_\theta}\right)^2 C'_M \left(\frac{V_{cr}}{B\omega_\theta(V_{cr})}\right)^2 \frac{\int_{L_{exp}} \phi_\theta^2 dx}{\int_L \phi_\theta^2 dx} = 1 \tag{3.65}$$

from which we are able to solve for the critical mean wind velocity V_{cr} for static divergence,

$$V_{cr} = B \cdot \omega_\theta \cdot \left(\frac{2\tilde{m}_\theta}{\rho B^4 C'_M} \cdot \frac{\int_L \phi_\theta^2 dx}{\int_{L_{exp}} \phi_\theta^2 dx}\right)^{1/2} \tag{3.66}$$

3.7.2 Galloping

Galloping is a single mode unstable behaviour containing motion purely in the vertical direction, i.e. the mode shape vector becomes $\boldsymbol{\varphi}_1 \approx \begin{bmatrix} 0 & \phi_z & 0 \end{bmatrix}^T$. The resonance frequency associated with this mode is $\omega_r = \omega_z(V)$. Since the motion is purely vertical, the impedance matrix reduces to

$$\hat{E}_\eta\left(\omega_r, V_{cr}\right) = 1 - \kappa_{ae_{zz}} - \left(\omega_r/\omega_z\right)^2 + 2i\left(\zeta_z - \zeta_{ae_{zz}}\right)\omega_r/\omega_z \tag{3.67}$$

In this case, unstable behaviour will occur under the simultaneous conditions that

$$\begin{aligned} \mathrm{Re}\left(\hat{E}_\eta\right) &= 1 - \kappa_{ae_{zz}} - \left(\omega_r/\omega_z\right)^2 = 0 \\ \mathrm{Im}\left(\hat{E}_\eta\right) &= 2i\left(\zeta_z - \zeta_{ae_{zz}}\right)\omega_r/\omega_z = 0 \end{aligned} \tag{3.68}$$

from which we observe that

$$\begin{aligned} \omega_r^2 &= \omega_z^2 - \omega_z^2\kappa_{ae_{zz}} = \omega_z^2 - \tfrac{\rho B^2}{2\tilde{m}_z} \cdot \omega_r^2 \cdot H_4^* \tfrac{\int_{L_{exp}} \phi_z^2 dx}{\int_L \phi_z^2 dx} \\ \Rightarrow \omega_r &= \omega_z(V_{cr}) = \omega_z\left(1 + \tfrac{\rho B^2}{2\tilde{m}_z} H_4^* \tfrac{\int_{L_{exp}} \phi_z^2 dx}{\int_L \phi_z^2 dx}\right)^{-1/2} \end{aligned} \tag{3.69}$$

and that

$$\zeta_z = \zeta_{ae_{zz}} = \frac{\rho B^2}{4\tilde{m}_z}\left(\frac{\omega_z(V_{cr})}{\omega_z}\right) H_1^* \frac{\int_{L_{exp}} \phi_z^2 dx}{\int_L \phi_z^2 dx} \tag{3.70}$$

It should also be noted that since $\zeta_z - \zeta_{ae_{zz}} = 0$ is a requirement for galloping to occur, it will only occur when H_1^* is positive. As seen from the expression above, negative H_1^* will increase the total vertical damping of the system, hence $\zeta_z - \zeta_{ae_{zz}} = 0$ will never be fulfilled.

Substituting the quasi-static expression for H_1^* from Eq 3.30 into Eq. 3.70, we are able to obtain an expression for V_{cr} for galloping:

$$\zeta_z = -\frac{\rho B^2}{4\tilde{m}_z}\left(\frac{\omega_z(V_{cr})}{\omega_z}\right)\left(C_L' + \bar{C}_D\frac{D}{B}\right)\frac{V_{cr}}{B\omega_z(V_{cr})}\frac{\int_{L_{exp}}\phi_z^2 dx}{\int_L \phi_z^2 dx} \tag{3.71}$$

$$\Rightarrow V_{cr} = B\omega_z \cdot \frac{\zeta_z}{-\left(C_L' + \bar{C}_D \cdot D/B\right)} \cdot \frac{4\tilde{m}_z}{\rho B^2} \cdot \frac{\int_L \phi_z^2 dx}{\int_{L_{exp}} \phi_z^2 dx} \tag{3.72}$$

Another prerequisite for galloping is that $C_L' < -\bar{C}_D \cdot D/B$. The right side of this inequality is always positive. However, the slope of the lift coefficient $\left(C_L'\right)$ is able to take negative values, which should be taken as a danger signal.

3.7.3 Dynamic instability in torsion

Another type of single mode unstable behaviour is known simply as dynamic instability in torsion. The mode shape vector for this type of instability becomes $\boldsymbol{\varphi}_2 \approx \begin{bmatrix} 0 & 0 & \phi_\theta \end{bmatrix}^T$, and its corresponding resonance frequency $\omega_r = \omega_\theta(V)$. Since vertical z motion is not present or neglected, the impedance matrix reduces to

$$\hat{E}_\eta\left(\omega_r, V_{cr}\right) = 1 - \kappa_{ae_{\theta\theta}} - \left(\omega_r/\omega_\theta\right)^2 + 2i\left(\zeta_\theta - \zeta_{ae_{\theta\theta}}\right)\omega_r/\omega_\theta \tag{3.73}$$

where unstable behaviour will only occur when both the real and imaginary parts are simultaneously equal to zero:

$$\begin{aligned} \mathrm{Re}\left(\hat{E}_\eta\right) &= 1 - \kappa_{ae_{\theta\theta}} - \left(\omega_r/\omega_\theta\right)^2 = 0 \\ \mathrm{Im}\left(\hat{E}_\eta\right) &= 2i\left(\zeta_\theta - \zeta_{ae_{\theta\theta}}\right)\omega_r/\omega_\theta = 0 \end{aligned} \tag{3.74}$$

It is seen that

$$\omega_r = \omega_\theta(V_{cr}) = \omega_\theta\left(1 + \frac{\rho B^4}{2\tilde{m}_\theta}A_3^*\frac{\int_{L_{exp}}\phi_\theta^2 dx}{\int_L \phi_\theta^2 dx}\right)^{-1/2} \tag{3.75}$$

when damping is such that

$$\zeta_\theta = \zeta_{ae_{\theta\theta}} = \frac{\rho B^4}{4\tilde{m}_\theta}\left(\frac{\omega_\theta(V_{cr})}{\omega_\theta}\right)A_2^*\frac{\int_{L_{exp}}\phi_\theta^2 dx}{\int_L \phi_\theta^2 dx} \tag{3.76}$$

Since $\zeta_\theta - \zeta_{ae_{\theta\theta}} = 0$ is a requirement for dynamic instability in torsion, A_2^* must attain positive values for this to be an issue.

3.7.4 Flutter

The last type of instability discussed here is a combined unstable motion of both vertical and torsion displacements. This can occur when the mean wind velocity dependent resonance frequencies $\omega_z(V_{cr})$ and $\omega_\theta(V_{cr})$ get coupled, i.e. resonance occurs for both

vertical and torsional displacements at the same frequencies. This coupling occurs via the off-diagonal terms $\kappa_{ae_{z\theta}}$ and $\kappa_{ae_{\theta z}}$ and therefore the two modes considered must be shape-wise similar, i.e. the off-diagonal terms must be unequal to zero. The two mode shapes are as follows:

$$\boldsymbol{\varphi}_1 \approx \begin{bmatrix} 0 & \phi_z & 0 \end{bmatrix}^T \qquad \boldsymbol{\varphi}_2 \approx \begin{bmatrix} 0 & 0 & \phi_\theta \end{bmatrix}^T \tag{3.77}$$

with corresponding eigenfrequencies $\omega_1 = \omega_z$ and $\omega_2 = \omega_\theta$. As before, the stability limit is identified by $\left|\det\left(\hat{\mathbf{E}}\left(\omega, V\right)\right)\right| = 0$. Flutter occurs when the eigenfrequencies are coupled, i.e. when $\omega_r = \omega_z(V_{cr}) = \omega_\theta(V_{cr})$. In this particular case, where only the two modes are considered, the impedance matrix is given as

$$\begin{aligned}\hat{\mathbf{E}}_\eta(\omega_r, V_{cr}) = &\begin{bmatrix} 1 & 0 \\ 0 & 1 \end{bmatrix} - \begin{bmatrix} \kappa_{ae_{zz}} & \kappa_{ae_{z\theta}} \\ \kappa_{ae_{\theta z}} & \kappa_{ae_{\theta\theta}} \end{bmatrix} - \begin{bmatrix} (\omega_r/\omega_z)^2 & 0 \\ 0 & (\omega_r/\omega_\theta)^2 \end{bmatrix} \\ &+ 2i \begin{bmatrix} \omega_r/\omega_z & 0 \\ 0 & \omega_r/\omega_\theta \end{bmatrix} \cdot \begin{bmatrix} \zeta_z - \zeta_{ae_{zz}} & -\zeta_{ae_{z\theta}} \\ -\zeta_{ae_{\theta z}} & \zeta_\theta - \zeta_{ae_{\theta\theta}} \end{bmatrix}\end{aligned} \tag{3.78}$$

Fully expanding the real and imaginary parts of $\left|\det\left(\hat{\mathbf{E}}\left(\omega, V\right)\right)\right|$ separately gives the following two equations

$$\begin{aligned}\mathrm{Re}\left(\det\left(\hat{\boldsymbol{E}}_\eta\right)\right) = &\, 1 - \kappa_{ae_{zz}} - \kappa_{ae_{\theta\theta}} + \kappa_{ae_{zz}} \cdot \kappa_{ae_{\theta\theta}} - \kappa_{ae_{z\theta}} \cdot \kappa_{ae_{\theta z}} - \\ &4 \cdot \left[(\zeta_z - \zeta_{ae_{zz}}) \cdot (\zeta_\theta - \zeta_{ae_{\theta\theta}}) - \zeta_{ae_{z\theta}} \cdot \zeta_{ae_{\theta z}}\right] \cdot (\omega_r/\omega_z) \cdot (\omega_r/\omega_\theta) - \\ &(1 - \kappa_{ae_{\theta\theta}}) \cdot (\omega_r/\omega_z)^2 - (1 - \kappa_{ae_{zz}}) \cdot (\omega_r/\omega_\theta)^2 + (\omega_r/\omega_z)^2 \cdot (\omega_r/\omega_\theta)^2 = 0\end{aligned} \tag{3.79}$$

$$\begin{aligned}\mathrm{Im}\left(\det\left(\hat{\boldsymbol{E}}_\eta\right)\right) = &\, 2 \cdot \{[(1 - \kappa_{ae_{\theta\theta}}) \cdot (\zeta_z - \zeta_{ae_{zz}}) - \kappa_{ae_{\theta z}} \cdot \zeta_{ae_{z\theta}}] \cdot \omega_r/\omega_z + \\ &[(1 - \kappa_{ae_{zz}}) \cdot (\zeta_\theta - \zeta_{ae_{\theta\theta}}) - \kappa_{ae_{z\theta}} \cdot \zeta_{ae_{\theta z}}] \cdot \omega_r/\omega_\theta - \\ &(\zeta_\theta - \zeta_{ae_{\theta\theta}}) \cdot (\omega_r/\omega_\theta) \cdot (\omega_r/\omega_z)^2 - (\zeta_z - \zeta_{ae_{zz}}) \cdot (\omega_r/\omega_z) \cdot (\omega_r/\omega_\theta)^2\} = 0\end{aligned} \tag{3.80}$$

It should be noted that calculating the flutter stability limit involves iterations, since ω_r and V_{cr} both need to be known to be able to read off the aerodynamic derivatives. In cases where ω_θ/ω_z is larger than 1.5, Selberg's formula may be used to provide a rough estimate of the stability limit,

$$V_{cr} = 0.6 B \omega_\theta \left\{ \left[1 - \left(\frac{\omega_z}{\omega_\theta}\right)^2\right] \cdot \frac{(\tilde{m}_z \cdot \tilde{m}_\theta)^{1/2}}{\rho B^3} \right\}^{1/2} \tag{3.81}$$

4 Suspension Bridges

Suspension bridges have four main components which all work together: bridge deck beam, cable system, towers and anchor blocks. The roadway itself is supported from below by a girder beam, which most often consist of either a system of trusses or a stiffened box girder. There are usually two towers, or pylons, on each side of the bridge main span. They sustain two parallel cables, which in turn sustain the girder beam through vertical hangers that connect the two together. From the pylons, the cables connect to an anchor block which transfers the axial forces from the cables to the ground. The four components are shown in Figure 4.1. The anchorages and towers are usually erected first. Then the cables are installed between the two tower pairs and hangers attached to them. Finally, the girder beam can be raised to position, usually in sections, which are then individually hooked to the hangers [8].

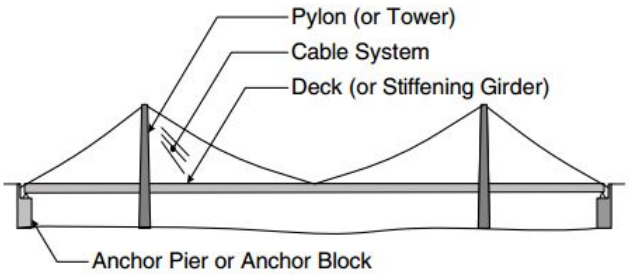

Figure 4.1: A typical suspension bridge [10]

4.1 The Single Span Suspension Bridge

The single span suspension bridge is the most simple case of a suspension bridge. Only the main span is supported by the cable system while the main cables continue past the pylons as backstays connected to the anchor blocks. This means that the side spans are acting independent of the cable system. All the weight of the main beam is transferred via the hangers directly into the two cables. From there the weight is transferred to the pylons, and further into the anchor blocks via the backstays [10]. The overall geometry of a single span suspension bridge is shown in Figure 4.2,

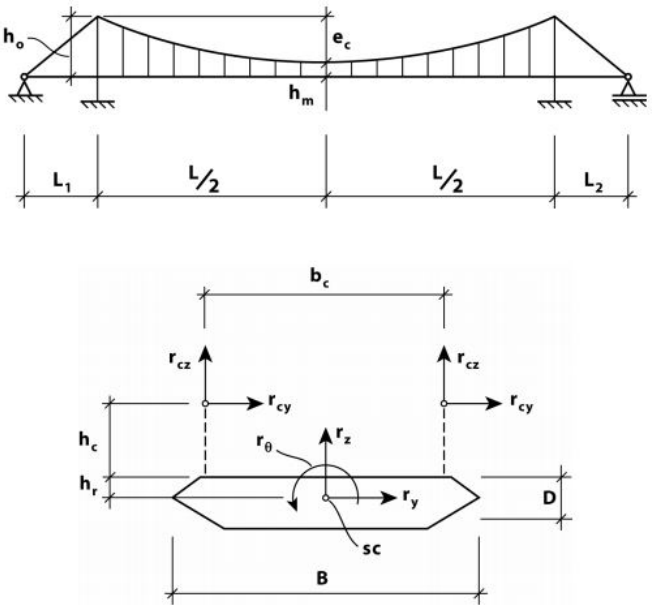

Figure 4.2: A single span suspension bridge [21]

where:
$h_o -$ height of the pylons measured from the deck
$e_c -$ cable sag
$h_m -$ distance between cable and deck at midspan
$L -$ length of main span
$L_1, L_2 -$ length of side spans
$B -$ width of the deck
$D -$ depth of the deck
$b_c -$ distance between the cables on either side of the deck
$r_n -$ deck displacement components, $n = z, y, \theta$
$r_{cn} -$ cable displacement components, $n = z, y$
$h_c -$ height of cables at an arbitrary coordinate along the span
$h_r -$ vertical distance between the shear centre (sc) and hanger attachment

For simplicity, it is assumed that the shear centre of the main beam coincides with its centroid. Flexibility of hangers as well as backstays and towers are ignored as that usually only results in minor discrepancies in the calculation of the eigenvalues of the system. With these assumptions in place, the system behaves as a combination of two cables and a beam where the main girder and the the two cable planes move in perfect harmony. Therefore, the motion of the system can be split into three independent components: in plane vertical component z, out of plane horizontal component y and pure torsion component θ. The idealized structural system of a suspension bridge is shown in Figure 4.3, where it has been distinguished between the distributed mass m_n of the bridge girder in the $n = y$, z and θ directions. The hanger self weight is included, half in m_z and half in the self

weight of the cable, m_c. EI_y, EI_z, GI_t and EI_w give the stiffness properties of the beam, while $(EA)_c$ gives the stiffness properties of the cable. It should be noted that the shear force V_b in the beam at its connection to the two pylons is negligible, due to all its weight being distributed to the cables and further to the ground, as described previously in this section.

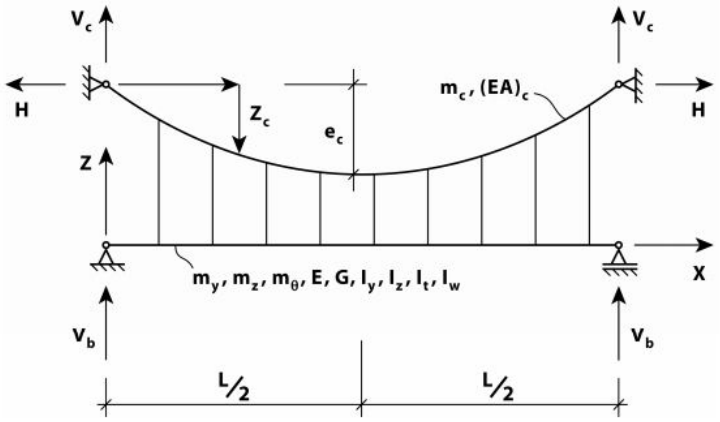

Figure 4.3: Idealized structural system of a suspension bridge [21]

4.2 The Cable Systems

4.2.1 Structural Considerations

A cable system consists of a cable and attached hangers. In a traditional suspension bridge, the cables are supported at 4 points: the anchorage to the ground on each side of the bridge, and on the two pylon tops. The cables are the main load-carrying components in the bridge. They are what holds up the bridge deck and transfer the loads to the ground. They are therefore designed to support the loads from the girder, the hanger cables and their own self weight. Vertical forces from traffic and self weight of the bridge deck are transferred through to the hangers as tensile forces and from there to the cables, which will then also be in pure tension. The biggest advantage of using cables as the main load-carrying elements is related to the low consumption of structural material in the cables themselves, as much smaller cross sections are required than for a steel beam, for example. This stems from the high efficiency of load transfer by pure tension [10].
An important attribute of a suspension cable is its ability to self-adapt to external loads. That is, it will instantly change the shape of its axis, vary curvature and deformation to adapt to the condition of stress on the structure. This is all elastic deformation so it will return to its equilibrium state after unloading, unlike a beam or and arch which are much more susceptible to plastic deformations [12].
It is important to consider the sag of the cables, as it has an effect on their load-carrying capabilities. The sag ratio is defined as the ratio of the sag of the cable (denoted e_c) to the length L of the cable span, e_c/L. The horizontal force H in the cable is inversely

proportional to the sag ratio. This means that small sag will result in large forces, requiring uneconomically thick cables. However, when the sag ratio becomes larger than a certain limit, deflections start to grow significantly. It has been determined that the optimal sag ratio, giving not too high loads and not too high deflections, is generally between $\frac{1}{9}$ and $\frac{1}{11}$. It is noted that the sag ratio can for example be adjusted by increasing or decreasing the pylon height in the design [10].

4.2.2 The Shallow Cable Theory

Unlike beams or beam-columns, a cable has negligible cross sectional bending and torsion stiffness. Therefore a cable must rely almost entirely on the presence of an axial force N and its axial elastic stiffness property EA, where E is the elastic modulus for the cable material and A is the cross section area. Thus, a cable will only offer stiffness against displacement r_x, r_y and r_z. Shallowness is assumed in the following theory. A cable is defined as shallow if the cable sag is less than $\frac{1}{10}$ of its suspended length. Figure 4.4a shows the shallow cable suspended over the main span of a bridge, where z_c is the cable vertical position at an arbitrary coordinate x, e_c is the cable sag and L is the length of the span. Figure 4.4b shows a free body diagram of the same cable in static, or time invariant equilibrium [21].

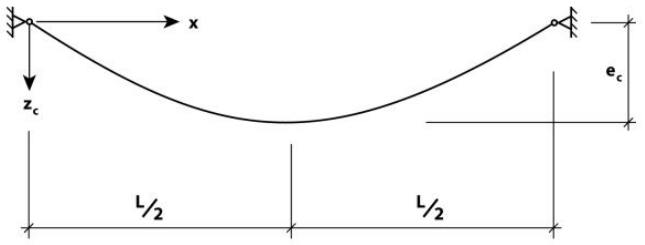

(a) Suspended cable

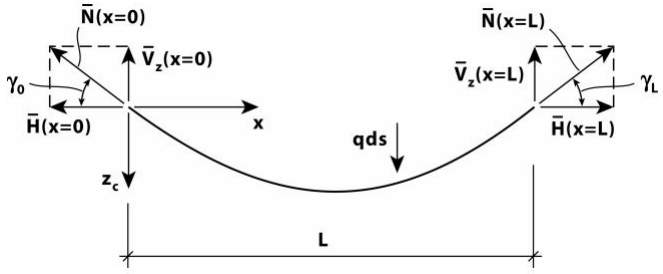

(b) Static equilibrium

Figure 4.4: A shallow cable supported at identical levels [21]

The cable will be subject to both static forces due to gravity field as well as forces due to dynamic motion of the cable itself. Only the static forces are shown in Figure 4.4b but for dynamic equilibrium, the fluctuating parts must also be included. The internal forces in the cables are then:

$$\begin{aligned} N_{tot} &= \bar{N}(x) + N(x,t) \\ H_{tot} &= \bar{H}(x) + H(x,t) \\ V_{z,tot} &= \bar{V}_z(x) + V_z(x,t) \\ V_{y,tot} &= V_y(x,t) \end{aligned} \tag{4.1}$$

where N_{tot} is the cross section axial force, and H_{tot} and $V_{z,tot}$ are its horizontal and vertical components respectfully, while $V_{y,tot}$ is the out of plane force component which is only caused by dynamic motion. The static parts of the forces are derived in detail in [21] by taking the force and moment equilibrium for an finite element ds at an arbitrary position along the span, subject only to vertical gravity force $q \cdot ds$. The time invariant axial force is found to be:

$$\bar{N} = \bar{H} \cdot \cosh\left(\frac{qx}{\bar{H}} - \frac{qL}{2\bar{H}}\right) \tag{4.2}$$

and the vertical force component at the supports:

$$\bar{V}_z(x=0) = \bar{V}_z(x=L) = \frac{qL}{2}\left[1 + \frac{1}{24}\left(\frac{qL}{\bar{H}}\right)^2\right] \tag{4.3}$$

It is noted that these expressions for $\bar{N}$ and $\bar{V}_z$ are dependent on the time invariant part of the horizontal force $\bar{H}$, which will be derived in Section 4.2.4. For suspension bridges, q is the total static vertical load acting on the cable, i.e. the self weight of the cable, beam and hangers.

The same method is used to establish the relevant dynamic equilibrium requirements, with the dynamic components added to the finite element diagram (see Figure 4.5). Cable shallowness is again assumed, and in addition the simplification that the cable motion in the x direction r_x is negligible is adopted. This is reasonable for bridges due to their high span-wise stiffness. With this assumption the equilibrium requirement in the x direction simply becomes [21]

$$\frac{d}{dx}\left(\bar{H} + H\right) = 0 \tag{4.4}$$

which implies that both $\bar{H}$ and $H(t)$ are independent of x.

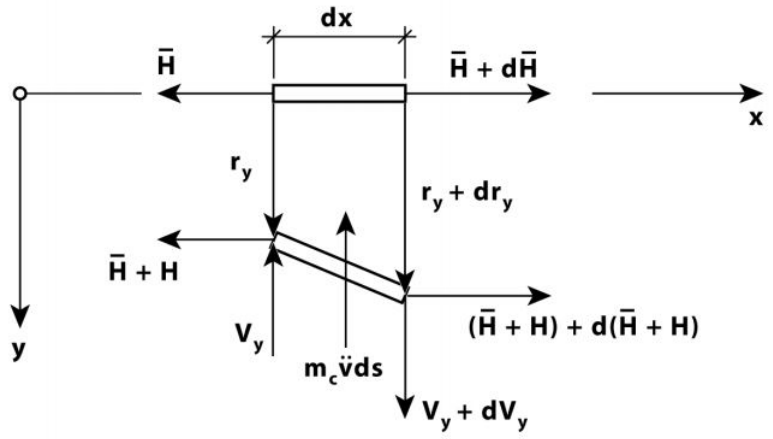

Figure 4.5: Equilibrium of shallow cable, y direction motion [21]

The corresponding equilibrium requirements in the y and z direction are given by

$$\begin{gathered} dV_y - m_c \ddot{r}_y \cdot ds = 0 \\ d\left(\bar{V}_z + V_z\right) + m_c g \cdot ds - m_c \ddot{r}_z \cdot ds = 0 \end{gathered} \tag{4.5}$$

where m_c is the cable mass per unit length. Similarly, the moment equilibrium taken about axes through the element midpoint and parallel to the y and z directions, are given by

$$\begin{gathered} \left(\bar{H} + H\right) \cdot d\left(z_c + r_z\right) - \left(\bar{V}_z + V_z\right) \cdot dx = 0 \\ \left(\bar{H} + H\right) \cdot dr_y - V_y \cdot dx = 0 \end{gathered} \tag{4.6}$$

from which the following is obtained

$$\begin{gathered} V_y = \left(\bar{H} + H\right) \frac{dr_y}{dx} \\ \bar{V}_z + V_z = \left(\bar{H} + H\right) \frac{d}{dx}\left(z_c + r_z\right) \end{gathered} \tag{4.7}$$

By substituting this into Eq. 4.5 and remembering that $\bar{H}$ and $H\left(t\right)$ are independent of x, we obtain

$$\begin{gathered} \left(\bar{H} + H\right) \frac{d^2 r_y}{dx^2} \frac{dx}{ds} = m_c \ddot{r}_y \\ \left(\bar{H} + H\right) \frac{d^2}{dx^2}\left(z_c + r_z\right) \frac{dx}{ds} + m_c g = m_c \ddot{r}_z \end{gathered} \tag{4.8}$$

The static case, where H, r_y and r_z are all zero, is then defined by

$$\bar{H} z_c^{"} = -m_c g \qquad \text{and} \qquad H z_c^{"} = -\frac{m_c g}{\bar{H}} H \tag{4.9}$$

Assuming that dynamic displacements are small, i.e. that

$$H r_y^{"} \ll \bar{H} r_y^{"} \qquad \text{and} \qquad H r_z^{"} \ll \bar{H} r_z^{"} \tag{4.10}$$

and shallowness justifies $ds \approx dx$, the first part of Eq. 4.8 becomes

$$\bar{H}r_y^{"}\frac{dx}{ds} + Hr_y^{"}\frac{dx}{ds} - m_c\ddot{r}_y = 0 \Rightarrow r_y^{"} - \frac{m_c}{\bar{H}}\ddot{r}_y = 0 \tag{4.11}$$

and the second part becomes

$$\begin{aligned} \bar{H}z_c^{"} + \bar{H}r_z^{"} + Hz_c^{"} + Hr_z^{"} + m_c g &= m_c\ddot{r}_z \\ \Rightarrow -m_c g + \bar{H}r_z^{"} - \tfrac{m_c g}{\bar{H}}H + m_c g &= m_c\ddot{r}_z \\ \Rightarrow \bar{H}r_z^{"} - \tfrac{m_c g}{\bar{H}}H - m_c\ddot{r}_z &= 0 \\ \Rightarrow r_z^{"} - \tfrac{m_c}{\bar{H}}\ddot{r}_z &= \tfrac{m_c g}{\bar{H}}\tfrac{H}{\bar{H}} \end{aligned} \tag{4.12}$$

Eq. 4.11 and 4.12 are the differential equations for unloaded and undamped motion of a shallow cable, for out of plane and vertical motion respectively. An expression for $H(t)$, the time dependent increase of cable tension during a small dynamic vertical motion $r_z(x,t)$, is yet to be determined. The reader is referred to [21] where this is derived in detail, while only the result will be included here. It is then given that

$$H(t) = \frac{EA}{l}\frac{8e_c}{L^2}\int_L r_z(x,t)\,dx \tag{4.13}$$

where $l_e = L\left[1 + 8\left(e_c/L\right)^2\right]$.
Defining

$$\lambda^2 = \left(\frac{8e_c}{L}\right)^2 \frac{EA}{\bar{H}}\frac{L}{l_e} \tag{4.14}$$

the full expressions for the differential equations for unloaded and undamped motion of a shallow cable become

$$\begin{aligned} r_y^{"} - \tfrac{m_c}{H}\ddot{r}_y &= 0 \\ r_z^{"} - \tfrac{m_c}{H}\ddot{r}_z &= \lambda^2\left(\tfrac{1}{L^3}\right)\textstyle\int_L r_z dx \end{aligned} \tag{4.15}$$

where $\int_L r_z dx$ accounts for cable stretching. It is noted that there is no coupling between r_z and r_y motion and therefore they may be handled separately. To solve these equations, we use the general solution for a differential equation which is given as

$$\begin{aligned} r_y(x,t) &= \mathrm{Re}\left[\phi_y(x)\cdot e^{i\omega t}\right] \\ r_z(x,t) &= \mathrm{Re}\left[\phi_z(x)\cdot e^{i\omega t}\right] \end{aligned} \tag{4.16}$$

where ϕ_y and ϕ_z are the mode shapes of the motion.

4.2.3 Solution to the Eigenvalue Problem for Shallow Cables

Horizontal Motion

Since in plane horizontal motion is trivial in the case of bridges, we only look at out of plane horizontal motion. In that situation $r_y \neq 0$ and $r_z = 0$ since the two motions are

uncoupled. Inserting Eq. 4.16 into Eq. 4.15 for that case, we get

$$\phi_y^{"} + \omega^2 \left(m_c/\bar{H}\right) \phi_y = 0 \tag{4.17}$$

which can only be satisfied for all values of x if the second derivative of ϕ_y is congruent to ϕ_y itself, and simultaneously satisfy the boundary conditions $\phi_y(x=0) = \phi_y(x=L) = 0$. That means that we can take the mode shape as an harmonic function, $\phi_{y_n} = a_{y_n} \sin(n\pi x/L)$, $n = 1, 2, 3, ...$ By inserting this into Eq. 4.17 and solving for ω_{y_n} we obtain the eigenfrequencies for horizontal out of plane motion

$$\omega_{y_n} = n\pi \sqrt{\bar{H}/(m_c L^2)} \tag{4.18}$$

Vertical Anti-symmetric Motion

In the case of vertical anti-symmetric motion (see Figure 4.6), $r_z \neq 0$, $r_y = 0$ and, since the cable retains its original length (no stretching for this type of motion as the cable is displaced anti-symmetrically about the midpoint), $\int_L r_z dx = 0$. Again, substituting Eq. 4.16 for vertical motion into Eq. 4.15 we get

$$\phi_z^{"} + \omega^2 \frac{m_c}{\bar{H}} \phi_z = 0 \tag{4.19}$$

where $\phi_{z_n} = a_{z_n} \sin(2n\pi x/L)$, $n = 1, 2, 3....$ Following the same procedure as before, we obtain the eigenfrequencies for vertical anti-symmetric motion

$$\omega_{z_n} = 2n\pi \sqrt{\bar{H}/(m_c L^2)} \tag{4.20}$$

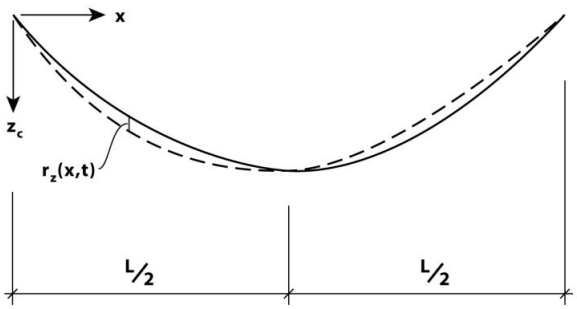

Figure 4.6: Vertical in plane anti-symmetric motion [21]

Vertical Symmetric Motion

In the case of vertical symmetric motion, cable stretching indeed does occur, so $\int_L r_z dx \neq 0$ and we must use the full version of Eq. 4.15 for vertical motion. This is shown in Figure 4.7. As before, introducing $r_z(x,t) = \mathrm{Re}\left[\phi_z(x) \cdot e^{i\omega t}\right]$ into Eq. 4.15 we get the differential equation

$$\phi_z^{"} + \beta^2 \phi_z = \lambda^2 \left(1/L^3\right) \int_L \phi_z dx \tag{4.21}$$

where $\beta^2 = \omega^2 m_c / \bar{H}$. The solution which satisfies the boundary conditions $\phi_y(x=0) = \phi_y(x=L) = 0$ as well as Eq. 4.21 for all values of x is given by

$$\phi_z = a_z \left\{1 - \cos\left[\beta\left(x - L/2\right)\right] / \cos\left(\beta L/2\right)\right\} \tag{4.22}$$

The eigenfrequencies are then obtained as before by substituting the expression for the mode shapes into the equation. After some simplifications, the resulting equation becomes

$$\tan\left(\frac{\beta L}{2}\right) = \frac{\beta L}{2} - \left(\frac{2}{\lambda}\right)^2 \left(\frac{\beta L}{2}\right)^3 \tag{4.23}$$

Since $\beta^2 = \omega^2 m_c / \bar{H}$, then any solution β_n to this equation represents an eigenfrequency

$$\omega_n = \beta_n \sqrt{\bar{H}/m_c} \tag{4.24}$$

and a corresponding eigenmode as given in Eq. 4.22.

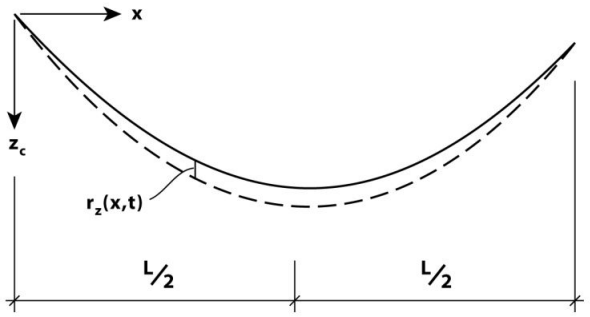

Figure 4.7: Vertical in plane symmetric motion [21]

4.2.4 Horizontal Cable Force in a Suspension Bridge System

With the addition of the beam forces to the system, the time invariant force diagram for each cable up to midspan is as shown in Figure 4.8, where q_s is the self weight of the beam taken up by the hangers and q_c is the self weight of the cable.

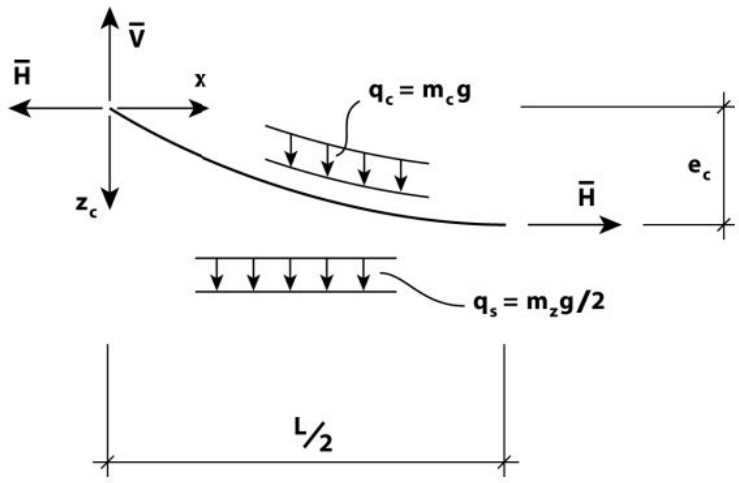

Figure 4.8: Time invariant force diagram for cable-beam system [21]

The time invariant horizontal cable force $\bar{H}$ in the cable-beam system can then be found by taking the moment equilibrium of half the cable span with respect to its top point, i.e. at its connection to the pylons. This gives:

$$\begin{aligned}\bar{H}\cdot e_c &= \int_0^{L/2}\left(\tfrac{m_z g}{2}dx + m_c g ds\right)x = g\int_0^{L/2}\left(\tfrac{m_z}{2}+m_c\tfrac{ds}{dx}\right)xdx \\ &= g\int_0^{L/2}\left\{\tfrac{m_z}{2}+m_c\left[1+\left(\tfrac{dz_c}{dx}\right)^2\right]^{\frac{1}{2}}\right\}xdx \approx g\int_0^{L/2}\left[\tfrac{m_z}{2}+m_c\left(1+\tfrac{1}{2}z_c'^2\right)\right]xdx\end{aligned} \tag{4.25}$$

Introducing $z_c \approx 4e_c\frac{x}{L}\left(1-\frac{x}{L}\right)$:

$$\begin{aligned}\tfrac{\bar{H}e_c}{g} &= \tfrac{m_z}{2}\int_0^{L/2}xdx + m_c\int_0^{L/2}\left[1+8\left(\tfrac{e_c}{L}\right)^2\left(1-2\tfrac{x}{L}\right)^2\right]xdx \\ &= \tfrac{m_z L^2}{16}+\tfrac{m_c L^2}{8}\left[1+\tfrac{4}{3}\left(\tfrac{e_c}{L}\right)^2\right]\end{aligned} \tag{4.26}$$

This gives the following expression for the horizontal cable force:

$$\bar{H} = \frac{m_z g L^2}{16 e_c}\left\{1+\frac{2m_c}{m_z}\left[1+\frac{4}{3}\left(\frac{e_c}{L}\right)^2\right]\right\} \tag{4.27}$$

4.3 Bridge Deck

The deck is subject to the major part of the external load on a suspension bridge. The traffic load is applied directly to the deck, the deck usually has high self weight and also has a much larger contact area for the wind load as compared to the cable system. The deck must then be able to transfer these forces to the cable system to reduce the moments in the deck. For a conventional suspension bridge with vertical cable planes, the support

by the cable system is most efficient for the deck self weight, less efficient for the traffic load and least efficient for the horizontal load [10].
The design of the bridge deck in a suspension bridge decisively influences how much the deck participates in the total structural system, as well as the size of the vertical dead load and lateral wind load that will act on the bridge. With a small depth-to-span ratio the bridge becomes lighter and hence the self weight of the bridge is decreased. However, at the same time the flexural stiffness of the deck is also decreased, potentially leaving it vulnerable to aerodynamic load effects. A small width-to-span ratio also increases the slenderness of the bridge, hence reducing its stiffness and efficiency towards aerodynamic loading. When it comes to aerodynamic stability, the torsional and flexural stiffness of the deck play the biggest role. That is, a bridge deck will only experience catastrophic oscillations if the structure is so flexible or soft that its motion will allow the aerodynamic instability to develop fully at actual wind speeds. Sufficient stiffness can be achieved both by having large dimensions of the deck or by designing the deck with a streamlined shape.

4.3.1 Box Girders

Traditional suspension bridges made before the 1960s achieved aerodynamic stability by the application of large trusses with considerable flexural and torsional stiffness. However, since the successful application of a streamlined box girder in the Severn Bridge of Great Britain, they have gained considerable popularity and are widely used all over the world. A closed box section achieves sufficient torsional stiffness for smaller depths than a corresponding truss section would. Additionally, a streamlining of the bridge girder has clear advantages as it leads to reduced wind forces and thus smaller dimensions [10]. As an example, the cross section of the box girder used for the Hardanger Bridge deck is shown in Figure 4.9.

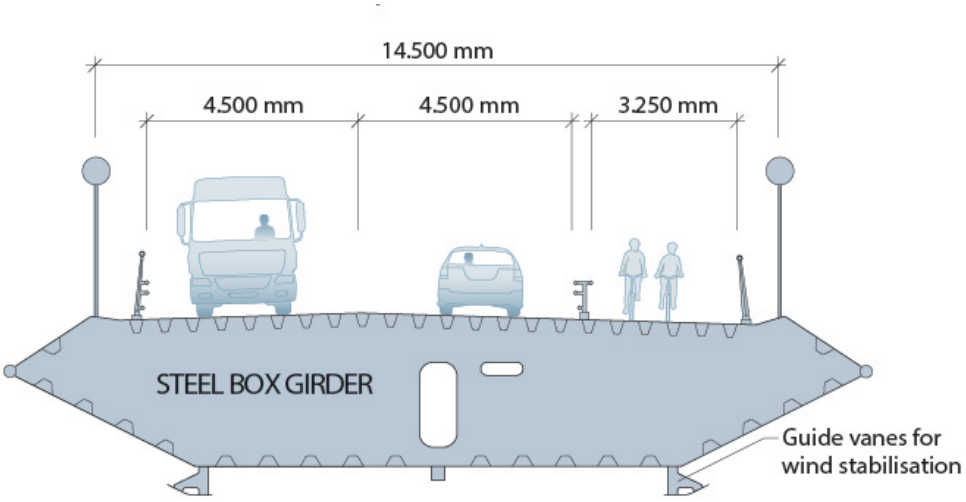

Figure 4.9: Bridge deck [15]

These kind of box girders usually have a streamlined hexagonal shape, with the hangers attached to the upper edges. This type of girder is torsionally stiff, which leads to a favourable distribution of forces between the two cable planes. This is because the torsional moment is taken up partly by the deck and partly by the cable systems, and in turn, the force distribution between the two cable systems on each side of the deck becomes more even. The twist angle of the deck is also reduced. The shape of the deck gives a significant aerodynamic benefit. The sharp edges on each side divide the air flow, reducing the drag coefficient, vortex shedding and flutter induced vibrations, and thus improving aerodynamic stability. The effect of this streamlined shape and the angle of the edge plates on vortex shedding is illustrated in Figure 4.10. It is seen that for a reduced angle, the vortex shedding is reduced as less vortices are formed and shed [10]. According to experimental tests conducted by Wang [25], keeping the angle of the inclined web below 16° not only restrains and delays vortex shedding but it also increases the critical flutter wind speed.
The design is asymmetric about the horizontal axis, which is beneficial in regards to vortex shedding. At vortex shedding level wind speeds, the asymmetric shape makes it so that it is more difficult for the upper vortices to become powerful enough to excite fluctuations of the deck (see Figure 4.11). At the point when critical flutter wind speeds are reached however, the upper vortex has strengthened to a level as powerful as the lower vortex. This means that the asymmetric shape does not stop aerodynamic instability from being introduced to the girder [25]. To further suppress vortex shedding induced vibrations, guide vains can be added on the bottom face (see Figure 4.9). They work by guiding the air flow through the vanes and thus disturb the formation of large vortices.
Stiffeners should be added to avoid buckling of the hollow box girder. They are placed on the inside where corrosion protection can be established efficiently by dehumidifying the air. The application of a streamlined box girder gives a noticeable saving in construction cost as compared to the truss deck. This is largely due to the fact that the box girders can be pre-fabricated in multiple sections and then assembled at the construction site [10].

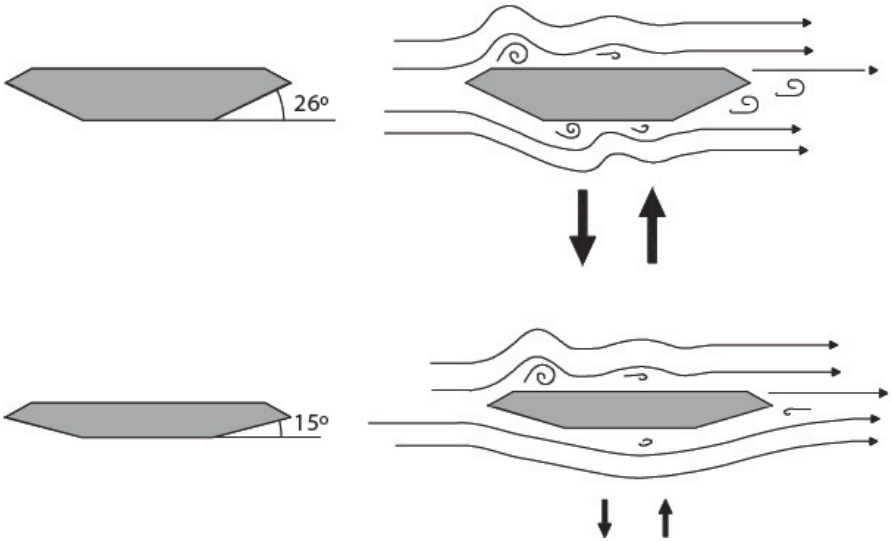

Figure 4.10: Effect of box girder shape and edge angle on vortex shedding [10]

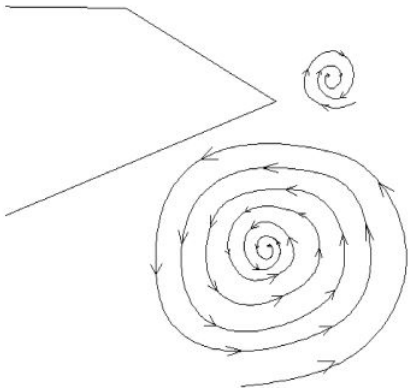

Figure 4.11: Vortex formation at low wind speeds [25]

4.3.2 Dual Box Girders

A dual box girder, is a cross section type where two box girders are used which are separated by a large gap. The box girders are connected together by stiffened transverse girders at regular intervals along the span. A dual box girder bridge is shown in Figure 4.12. The idea behind the dual box girder is twofold. Firstly, employing an air vent in the centre of the deck has been found to give clear aerodynamic stabilization benefits. Studies have shown that there is a clear trend for the flutter critical wind speed to increase as the gap between the two box girders is increased, until an optimal point is reached, after which it will decrease again [26]. It should be noted that since dual box girders have their masses distributed relatively far from the centre of mass of the bridge deck, the cross section is still very torsionally stiff despite the large gap. Secondly, the cross section dimensions, weight and material demand is significantly reduced as compared to using one large box section which means that the construction cost is reduced as well.

Figure 4.12: Conceptual design from 2002 of the Tsing Lung Bridge in Hong Kong [10]

4.4 Pylons

The pylons of a suspension bridge are tower structures. Their primary function is to elevate the main cables, and thus their height depend on the span length and sag ratio of the cables. In contrast to a regular free-standing tower, where the moment induced from the horizontal wind loading dominates the design, the most decisive load on the pylons will be the axial force originating from the cables which are attached to the pylon [10]. This is seen in Figure 4.13, where T_C and T_A are the forces in the cables on either side of the tower, and R_T is the resultant of the vertical components of the cable forces at the supporting point. Hence the towers can be designed as simply supported columns susceptible to buckling. In the case of lateral loading on the deck, it will deflect laterally, in which case a proper structural model for the pylon would be a simply supported column loaded with an axial force R_T at the top and a moment $R_T e_g$ at the bottom, where e_g is the eccentricity of the column base as compared to the top. This model is shown in Figure 4.14.

It is noted that even though the axial loading from the cables is the dominating part of the pylon structural design, it is only part of the force system acting on the pylon and other forces such as reactions from cable dead load and wind loading should not be neglected [10].

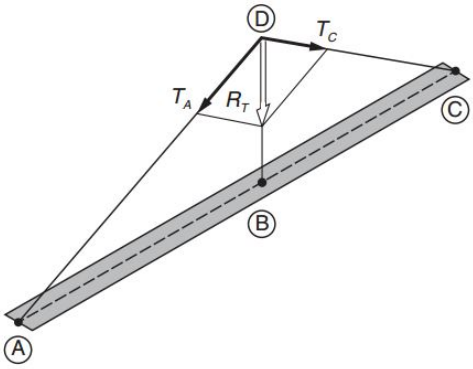

Figure 4.13: The axial force resultant acting on the pylon tower [10]

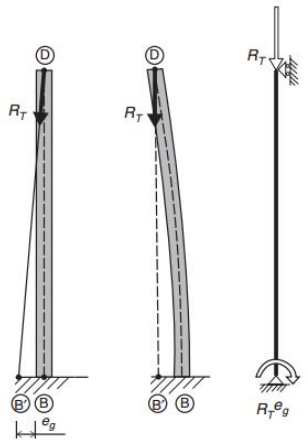

Figure 4.14: Pylon modelled as a column with base moment [10]

5 The Halsafjorden Bridge

5.1 Overview

As part of the Ferjefri E39 project, NPRA is conducting a study of the possible bridge designs to cross the over 2 km wide fjord. Currently, the Halsafjord must be crossed by a ferry connection, which can be felt as a barrier as it contributes to increasing the travel time between the towns in the region. A bridge over this fjord would effectively replace this ferry connection, and reduce travel times through the region [14]. Many possible solutions have been investigated for crossing the fjord, such as a single span suspension bridge, a floating bridge, a multi-span suspension bridge with a floating support and an underwater tunnel. The solution considered in this thesis is the single span suspension bridge. The bridge site is located over 4 km north of the current ferry connection, reaching from Halsaneset on the west side of the fjord, to Åkvik on the east. Figure 5.1 shows the bridge site, as well as the current ferry connection.

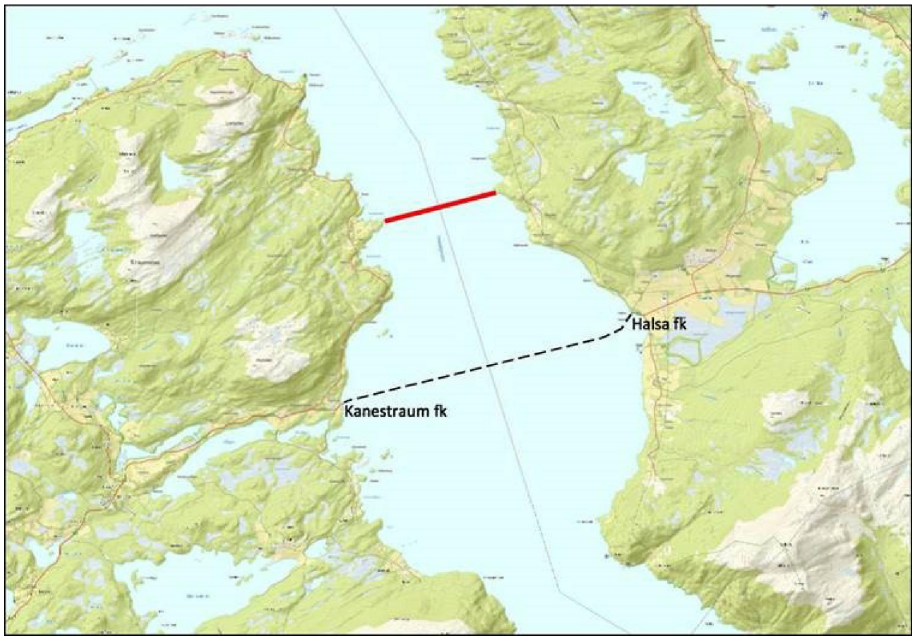

Figure 5.1: Halsafjorden bridge site (red line) and the current ferry crossing (dotted line) [www.vegvesen.no]

With a width of ca. 2000 meters and a depth of up to 490 meters at this site, bridging this fjord involves great challenges. The depth makes it difficult to place intermediate supports along the span, and therefore a single span suspension bridge is considered. Such a suspension bridge would have a main span of 2050 m, which would be the longest

main span in the world. Currently, the record holder is the Akashi-Kaikyo bridge in Japan with a main span of 1991 meters. An illustration of the proposed bridge design is shown in Figure 5.2. The extreme length and slenderness of the proposed bridge makes aerodynamic design highly important.

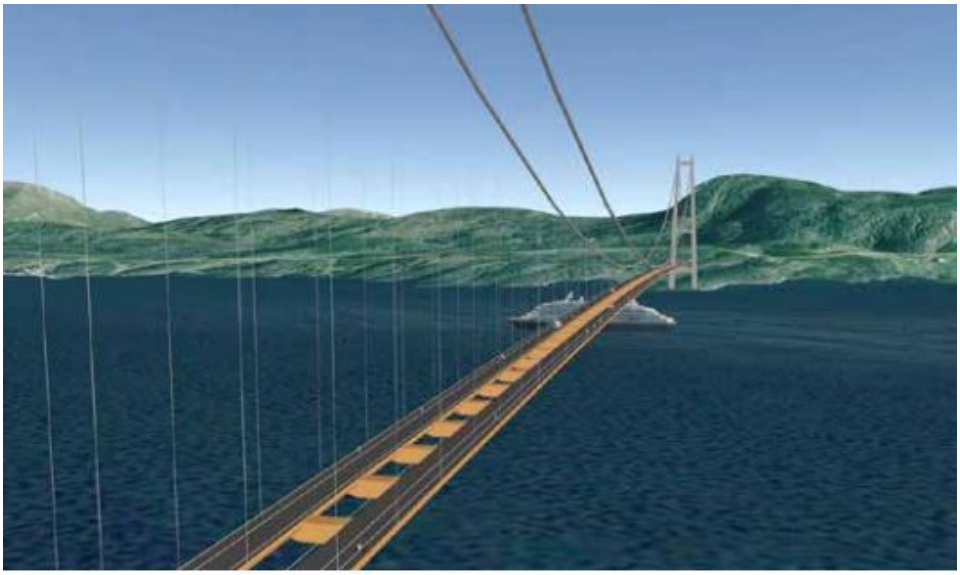

Figure 5.2: Illustration of a proposed bridge design over Halsafjorden [14]

5.2 Outline of the Bridge

A side view of the proposed bridge design with relevant dimensions is shown in Figure 5.3. Concrete pylons with a height of 265 meters are on either side of the main span, from which the cables suspend down to the rock anchor blocks over a side span of 410 meters. The cable sag is $e_c = 205\,m$ which gives a sag ratio of 0,1. The main cables have a diameter of $\phi 75\,mm$, a tensile strength of $1860\,MPa$ and a constructive steel area of $A = 0,375\,m^2$ each. Hangers as full-locked coil ropes with a diameter of $\phi 100\,mm$ are used to connect the cables to the bridge deck at 30 meter intervals. The deck consists of a twin box girder, chosen for its beneficial aerodynamic properties. Each box girder has a height of $D = 2,5\,m$, a width of $B = 11\,m$ and an area of $A = 0,4430\,m^2$, whereas the gap between them is 10 meter long. Each girder supports a two lane roadway as well as a walking/cycling path. The two box girders are connected together by transverse stiffened steel girders with a height of 2,5 m, width of 1,5 m and a constructive steel area of 0,132 m^2. The transverse girders are placed in line with the hangers at 30 m intervals along the bridge span [16]. The bridge deck is shown in Figure 5.4.

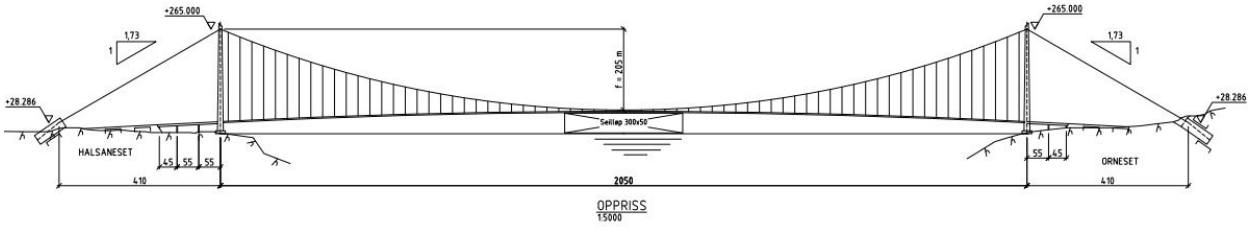

Figure 5.3: Illustration of a proposed bridge design over Halsafjorden [16]

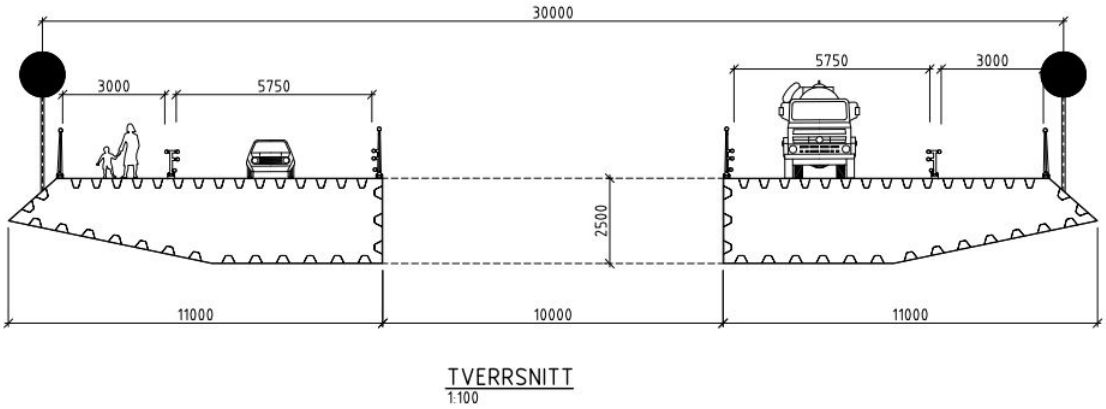

Figure 5.4: Bridge deck of the proposed Halsafjorden bridge [16]

5.3 Cross-Sectional Properties of Bridge Deck

The necessary cross sectional parameters for numerical analysis of the bridge will be presented in this section. All data in this section was either given by or based on data provided by the NRPA [16].

5.3.1 Stiffness Parameters

The second moment of area for a given cross section quantifies its ability to resist bending or buckling. It is highly dependent on the size and shape, or mass distribution, of the section at hand [9]. For a single box in the Halsafjorden bridge deck, the second moments of area are given as

$$\begin{cases} I_{y,box} = 0,4414\, m^4 \\ I_{z,box} = 5,2398\, m^4 \\ I_{T,box} = 1,0402\, m^4 \end{cases} \tag{5.1}$$

where $I_{y,box}$ is the second moment of area of one box girder about the horizontal axis, $I_{z,box}$ about the vertical axis, and $I_{T,box}$ is the torsional constant. However, since the deck consists of two box girders, the centre of gravity of each box does not coincide with the centre of gravity of the combined system about the vertical z axis. As a consequence, the

parallel axis theorem must be used to calculate the second moment of area of the total dual box cross section. This theorem must be used whenever it is necessary to find the second moment of area with respect to any axis other than the centroidal axis [9]. Hence, we find that

$$I_z = 2 \cdot \left(I_{z,box} + A_{box} \cdot r_z^2\right) \tag{5.2}$$

where r_z is the perpendicular distance between the two axes in question, the centroid of the deck and the vertical centroid of one box, $r_z = 9,69\,m$. The contribution from the transverse girder has been assumed to be negligible in this case. Additionally, since the horizontal gravity axis for each box coincides with the centroid, $r_y = 0$, then the total second moment of area about the horizontal axis simply becomes

$$I_y = 2 \cdot I_{y,box} \tag{5.3}$$

and the torsional constant becomes

$$I_T = 2 \cdot I_{T,box} \tag{5.4}$$

The above quantities are then given as

$$\begin{cases} I_y = 0,8828\,m^4 \\ I_z = 93,67\,m^4 \\ I_T = 2,0804\,m^4 \end{cases} \tag{5.5}$$

For a full description of the stiffness of the bridge deck, we must also determine a warping constant C_w. It has been given to be $C_{w,box} = 0,856\,m^6$ for each box girder, and assumed to be $C_w = 2 \cdot C_{w,box}$ for the total deck cross section. This assumption is deemed acceptable as the warping constant has only a small influence on the results. A description of the bending stiffness of the bridge deck is given by multiplication of the before determined parameters with either the Young's modulus of elasticity E or the shear modulus G as follows

$$\begin{cases} EI_y = 1,766 \times 10^{11}\,Nm^2 \\ EI_z = 1,873 \times 10^{13}\,Nm^2 \\ EC_w = 3,424 \times 10^{11}\,Nm^4 \\ GI_T = 1,664 \times 10^{11}\,Nm^2 \end{cases} \tag{5.6}$$

where $E \approx 200 \times 10^9\,N/m^2$ and $G \approx 80 \times 10^9\,N/m^2$ for steel.

5.3.2 Mass Parameters

The distributed mass in the vertical z direction is given as the sum of the individual contributions from the two box girders, the transverse girders and half of the mass of the hanger cables. Due to the mass distribution of the dual box girder deck, the rotational mass must be found using the parallel axis theorem, as such

$$m_\theta = 2 \cdot m_{\theta,box} + m_t + 2 \cdot \left(\frac{m_h}{2} + m_c\right) \cdot r_\theta^2 \tag{5.7}$$

where $m_{\theta,box}$ is the mass contribution from a single box, m_t,m_h and m_c are the mass contributions from the transverse girders, hanger cables and main cables respectively, and r_θ is half the distance between the two cable systems. It is found that the distributed masses are

$$\begin{cases} m_c = 3200\,kg/m \\ m_z = 13250\,kg/m \\ m_\theta = 2760000\,kgm^2/m \end{cases} \tag{5.8}$$

Since the numerical analysis performed in Section 6 will be performed in modal coordinates, we need to establish the modally equivalent distributed masses $\tilde{m}_z$ and $\tilde{m}_\theta$. Generally, a modal equivalent of an evenly distributed mass in the i direction can be obtained with the following equation

$$\tilde{m}_i = \tilde{M}_i / \int_L \left(\boldsymbol{\varphi}_i^T \cdot \boldsymbol{\varphi}_i\right) dx \tag{5.9}$$

For the z and θ directions and a two mode approach, this reduces to

$$\tilde{m}_z = \tilde{M}_z / \int_L \left(\phi_z^2\right) dx = \int_{L_{exp}} \left(m_z + 2 \cdot m_c\right) \phi_z^2 dx / \int_L \phi_z^2 dx \tag{5.10}$$

$$\tilde{m}_\theta = \tilde{M}_\theta / \int_L \left(\phi_\theta^2\right) dx = \int_{L_{exp}} m_\theta \phi_\theta^2 dx / \int_L \phi_\theta^2 dx \tag{5.11}$$

Assuming $L_{exp} = L$, i.e. the wind exposed span is identical to the bridge main span, this is reduced further and we find the modally equivalent and evenly distributed masses

$$\begin{cases} \tilde{m}_z = m_z + 2 \cdot m_c = 19650\,kg/m \\ \tilde{m}_\theta = m_\theta = 2760000\,kgm^2/m \end{cases} \tag{5.12}$$

5.3.3 Cable Forces

For control purposes, the capacity of the main cables has been calculated. The capacity of a cable in the ultimate limit state is given by Handbook N400 from the NPRA [13].

Given the cable properties already established in Section 5.2, an ultimate tensile strength of $f_{u,c} = 1860\,MPa$ and a constructive steel area of $A_c = 0,375\,m^2$, we get the capacity of the main cables

$$F_{Rd} = \frac{F_{uk}}{1,5\gamma_m} = \frac{f_{u,c}A_c}{1,5 \cdot 1,2} = 387,5 \times 10^3\,kN \tag{5.13}$$

where $\gamma_m = 1,2$ is a material factor. The design load on the cables is the horizontal static load given by Eq. 4.27, and given as

$$\bar{H} = \frac{m_z g L^2}{16 e_c}\left\{1 + \frac{2m_c}{m_z}\left[1 + \frac{4}{3}\left(\frac{e_c}{L}\right)^2\right]\right\} = \frac{13250 \cdot 9,81 \cdot 2050^2}{16 \cdot 205}\left\{1 + \frac{2 \cdot 3200}{13250}\left[1 + \frac{4}{3}\left(\frac{205}{2050}\right)^2\right]\right\} = 248,05 \times 10^3\,kN$$

It is seen that $F_{Rd} > \bar{H}$ and that the utilization is $\frac{\bar{H}}{F_{Rd}} = 64\%$, so the cables pass the capacity check.

5.3.4 Load Coefficients

The load coefficients have been determined from static tests and found to be

$$\begin{bmatrix} \bar{C}_L & C'_L \\ \bar{C}_M & C'_M \end{bmatrix} = \begin{bmatrix} -0,246 & 4,473 \\ 0,098 & -1,540 \end{bmatrix} \tag{5.14}$$

where the drag coefficient $\bar{C}_D$ and its derivative C'_D have not been quantified since y direction response is minimal as compared to the other directions and horizontal motion is in addition not associated with instabilities.

5.4 Aerodynamic Derivatives and Indicial Functions

The common practice is to use aerodynamic derivatives obtained from aeroelastic section model tests for the calculation of dynamic response and the prediction of instabilities in a bridge deck. The aerodynamic derivatives in the Halsafjorden bridge have been described by the NPRA as indicial function pairs measured at mode shapes TS1/VS2, and must therefore be converted to aerodynamic derivatives to keep within the framework used in this thesis, which operates in the frequency domain. Indicial functions are the analogous time-domain counterparts of the aerodynamic derivatives. On the most general form, indicial functions are given by [2]

$$\Phi(s) = a_0 - \sum_{i=1}^{n} a_i e^{-b_i s} \tag{5.15}$$

where a_0, a_i and b_i are all constants to be identified from a non-linear least square method, and $s = V \cdot t/B$ is the dimensionless time. The first part of the equation, a_0, accounts for quasi-steady effect while the second part describes the unsteady evolution of the force. Indicial functions have the property that they must converge into one as time approaches infinity, and it follows that b_i must always be a positive value. The indicial functions can be converted to aerodynamic derivatives in the frequency domain by the following relationships [16]:

$$
\begin{aligned}
\frac{2\pi}{\hat{V}_i} H_1^* &= \frac{dC_L}{d\alpha}\left[1 - \sum_{i=1}^{N} a_{iLz} \frac{\pi^2}{b_{iLz}^2 \hat{V}_i^2 + \pi^2}\right] \\
\frac{2}{\hat{V}_i^2} H_4^* &= \frac{dC_L}{d\alpha}\left[\sum_{i=1}^{N} a_{iLz} \frac{b_{iLy}}{b_{iLz}^2 \hat{V}_i^2 + \pi^2}\right] \\
\frac{4\pi}{\hat{V}_i^3} H_2^* &= \frac{dC_L}{d\alpha}\left[\sum_{i=1}^{N} - a_{iL\alpha} \frac{b_{iL\alpha}}{b_{iL\alpha}^2 \hat{V}_i^2 + \pi^2}\right] \\
\frac{4\pi^2}{\hat{V}_i^2} H_3^* &= \frac{dC_L}{d\alpha}\left[1 - \sum_{i=1}^{N} a_{iL\alpha} \frac{\pi^2}{b_{iL\alpha}^2 \hat{V}_i^2 + \pi^2}\right] \\
\frac{2\pi}{\hat{V}_i} A_1^* &= \frac{dC_M}{d\alpha}\left[1 - \sum_{i=1}^{N} a_{iMz} \frac{\pi^2}{b_{iMz}^2 \hat{V}_i^2 + \pi^2}\right] \\
\frac{2}{\hat{V}_i^2} A_4^* &= \frac{dC_M}{d\alpha}\left[\sum_{i=1}^{N} a_{iMz} \frac{b_{iMy}}{b_{iMz}^2 \hat{V}_i^2 + \pi^2}\right] \\
\frac{4\pi}{\hat{V}_i^3} A_2^* &= \frac{dC_M}{d\alpha}\left[\sum_{i=1}^{N} -a_{iM\alpha} \frac{b_{iM\alpha}}{b_{iM\alpha}^2 \hat{V}_i^2 + \pi^2}\right] \\
\frac{4\pi^2}{\hat{V}_i^2} A_3^* &= \frac{dC_M}{d\alpha}\left[1 - \sum_{i=1}^{N} a_{iM\alpha} \frac{\pi^2}{b_{iM\alpha}^2 \hat{V}_i^2 + \pi^2}\right]
\end{aligned}
\tag{5.16}
$$

where $\hat{V}_i = 2\pi \cdot V/(B \cdot \omega_i)$ is the reduced mean wind velocity. In the particular case of the Halsafjorden bridge, $\frac{dC_L}{d\alpha} = 2\pi$ and $\frac{dC_M}{d\alpha} = \frac{\pi}{2}$. These are coefficients which should not be confused with the actual load coefficient slopes in Section 5.3.4. The constants a_{iLy}, $a_{iL\alpha}$, a_{iMy} and $a_{iM\alpha}$ identified for the Halsafjorden bridge are given in Table 1. The aerodynamic derivatives obtained from these equations are shown in Figure 5.5, where the aerodynamic derivatives of a flat plate are shown as a reference, represented by dotted lines.

Table 1: Indicial function constants

Constants	$\varphi_{Lz}(H_1^*, H_4^*)$	$\varphi_{L\alpha}(H_2^*, H_3^*)$	$\varphi_{Mz}(A_1^*, A_4^*)$	$\varphi_{M\alpha}(A_2^*, A_3^*)$
a_1	$3,1871$	$9,9797 \times 10^2$	$6,3134 \times 10^1$	$1,7282$
b_1	$7,5233 \times 10^{-3}$	$4,1659 \times 10^{-1}$	$4,4634 \times 10^{-2}$	$8,2129 \times 10^{-2}$
a_2	$2,8661$	$2,5178 \times 10^1$	$-6,1917 \times 10^1$	$-8,7918 \times 10^{-1}$
b_2	$1,3663$	$3,2417 \times 10^1$	$4,7993 \times 10^{-2}$	$3,0692 \times 10^{-9}$
a_3	$-4,6341 \times 10^{-3}$	$-1,0000 \times 10^3$	0,0000	0,0000
b_3	$1,4553 \times 10^{-4}$	$4,1794 \times 10^{-1}$	0,0000	$9,6410 \times 10^{-2}$
a_4	-2,5164	0,0000	0,0000	0,0000
b_4	$1,3555 \times 10^{-1}$	0,0000	0,0000	0,0000

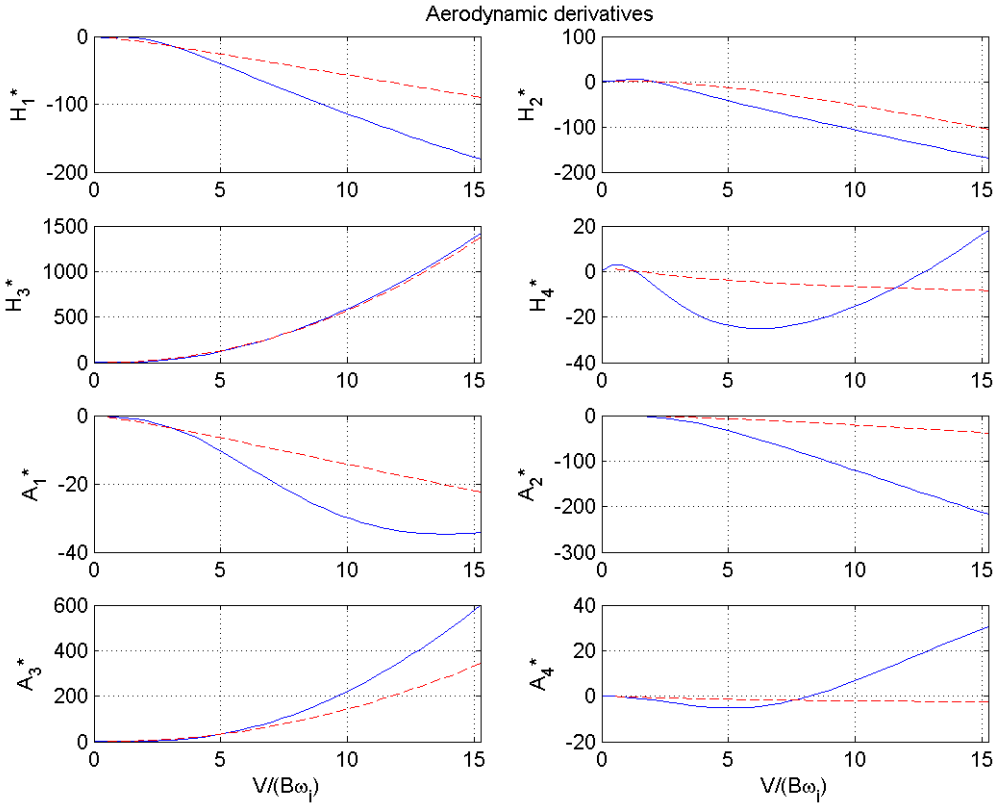

Figure 5.5: The aerodynamic derivatives of the Halsafjorden bridge deck. Dotted lines: Flat plate aerodynamic derivatives

5.5 Wind Properties at Bridge Site

At the time of writing this thesis, on site wind measurements have been ongoing for about two years. It has been found that the 10 minute average mean wind speed with a 50 years

return period, measured at $z_f = 50$ meters over sea level and normal to the bridge is [16]:

$$V_{10}(50) = 37,1\, m/s \tag{5.17}$$

The critical wind speed, determined based on a dynamic analysis and instability check, is required by [13] to be larger than 1,6 times the average mean wind speed, and has a return period of 500 years,

$$V_{cr,min} = 1,6 \cdot V_{10}(50) = 59,4\, m/s \tag{5.18}$$

The turbulence intensities have also been measured at the same height, and found to be

$$I_u = 0,12 \qquad I_v = 0,107 \qquad I_w = 0,047 \tag{5.19}$$

The integral length scales are found to be

$${}^{x_f}L_u = 100 \cdot (z_f/10)^{0,3} = 162\, m \tag{5.20}$$

$${}^{x_f}L_w = {}^{x_f}\, L_u/12 = 13,5\, m \tag{5.21}$$

6 Numerical Analysis

This section will present the methods used for analysis of the proposed Halsafjorden bridge, as well as the obtained results. The calculation program ALVSAT was used to find the eigenfrequencies and corresponding mode shapes in still air conditions. The lowest vertical eigenmode and lowest eigenmode in torsion were identified, and a two mode solution approach was pursued in modal coordinates. A frequency domain solution strategy was deemed to be most suitable, and selected for calculating the dynamic response and finding the stability limits. These calculations were performed using self-made scripts in the MATLAB programming language. These scripts can be found in Appendix B and have been verified against similar examples in [21].
For this analysis, the structure is assumed to be lightly damped such that a choice of vertical damping ratio $\zeta_z = 0,005$ at zero mean wind velocity is reasonable. The torsional damping ratio has little consequence on the stability limit, as seen from Figure 6.1, and its initial value is chosen as $\zeta_\theta = 0,005$.

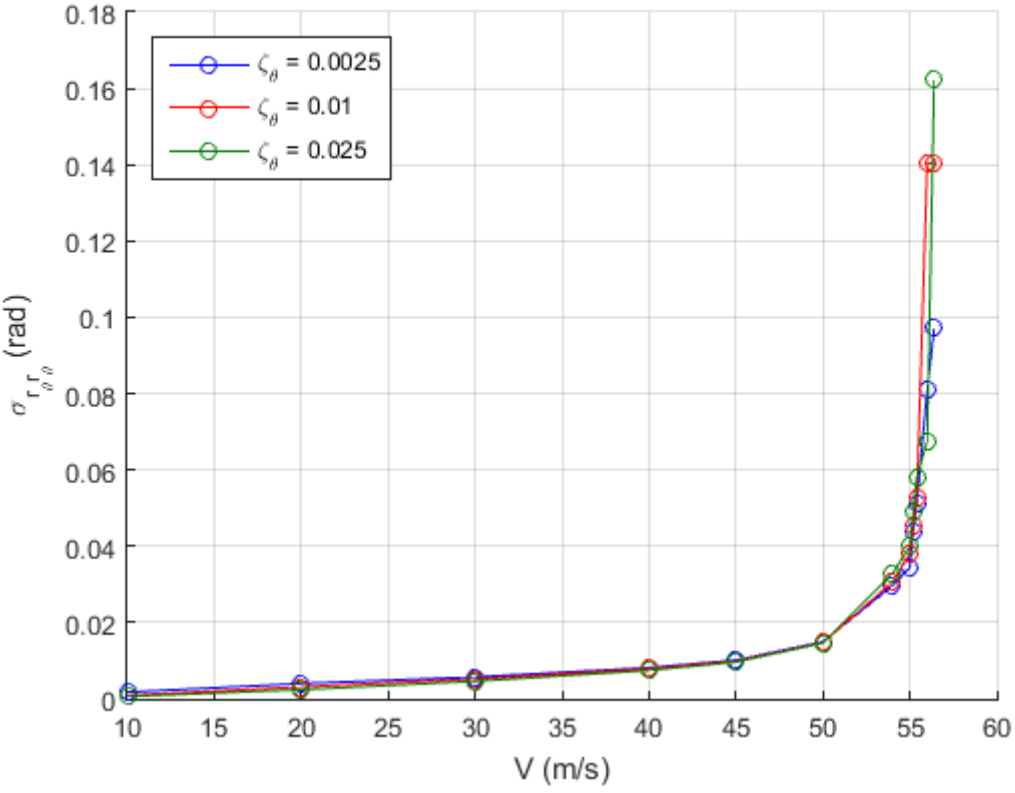

Figure 6.1: Effects of the variation on the damping ratio ζ_θ on the torsion response

6.1 ALVSAT

ALVSAT is a computer program designed specifically for the analysis of long suspension bridges under wind action [7]. Though the program has other capabilities, in this thesis it has been exclusively used to calculate the horizontal, vertical and torsional eigenfrequencies and eigenmodes in still air conditions, i.e. for $V = 0$. ALVSAT uses Galerkin's method (see Section 2.1.3) with Fourier coefficients to solve the eigenvalue problem. The precision of the mode shapes is dependent on the number of Fourier coefficients used in the calculation. As a general rule, the number of Fourier coefficients must be higher or equal to the number of mode shapes to be calculated. The 6 lowest eigenmodes for each direction of motion have been calculated, corresponding to 3 symmetric mode shapes and 3 asymmetric. The number of Fourier coefficients has been chosen to be 8 coefficients for each mode. This is deemed a sufficient number since the last rows of coefficients in the ALVSAT output are either close to or equal to zero. The values of the input parameters for the ALVSAT model, as well as the input file itself are given in Appendix A.1. The resulting output file is given in Appendix A.2.

6.2 Eigenfrequencies and Mode Shapes

The eigenfrequencies extracted from the ALVSAT output file are given in Table 2. Only the vertical and torsional eigenfrequencies are shown, as the horizontal modes will not be considered in the analysis. The notation is as follows: V=Vertical, T=Torsional, S=Symmetric, A=Asymmetric. The eigenfrequencies are numbered corresponding to the order they occur along the frequency range. The normalized mode shapes obtained from the calculations are shown in Figures 6.2 - 6.4. It is seen that the lowest eigenfrequencies in vertical and torsional motion are $\omega_z(V = 0) = 0,537\, rad/s$ and $\omega_\theta(V = 0) = 1,01\, rad/s$, respectively. Both have a corresponding asymmetrical mode shape. It should be noted that the lowest vertical and torsional mode shapes are shape-wise similar, so there is a possibility for coupling of the eigenfrequencies, that is, flutter instability may occur (see Section 3.7.4).

Table 2: Lowest eigenfrequencies for the Halsafjorden bridge

Mode Shape	ω_i [rad/s]	Mode Shape	ω_i [rad/s]
VA1	0,537	VS3	1,270
VS1	0,656	VA3	1,510
VS2	0,887	TS2	1,530
VA2	1,000	TA2	1,970
TA1	1,010	TS3	2,46
TS1	1,030	TA3	2,95

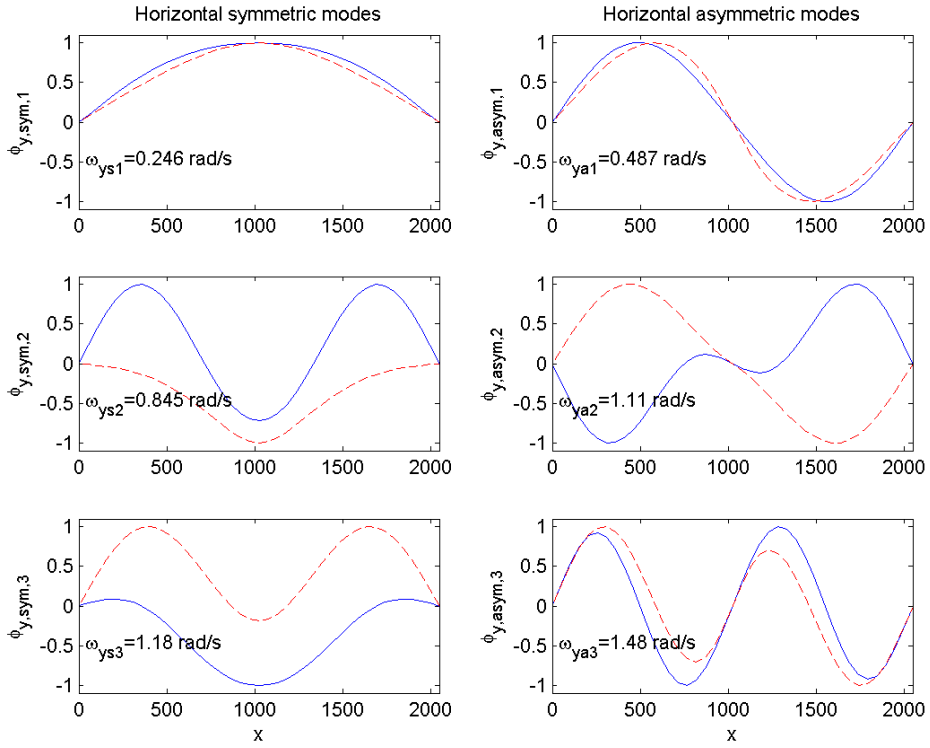

Figure 6.2: Lowest horizontal mode shapes for the Halsafjorden bridge. Fully drawn lines: main girder, broken lines: the cables

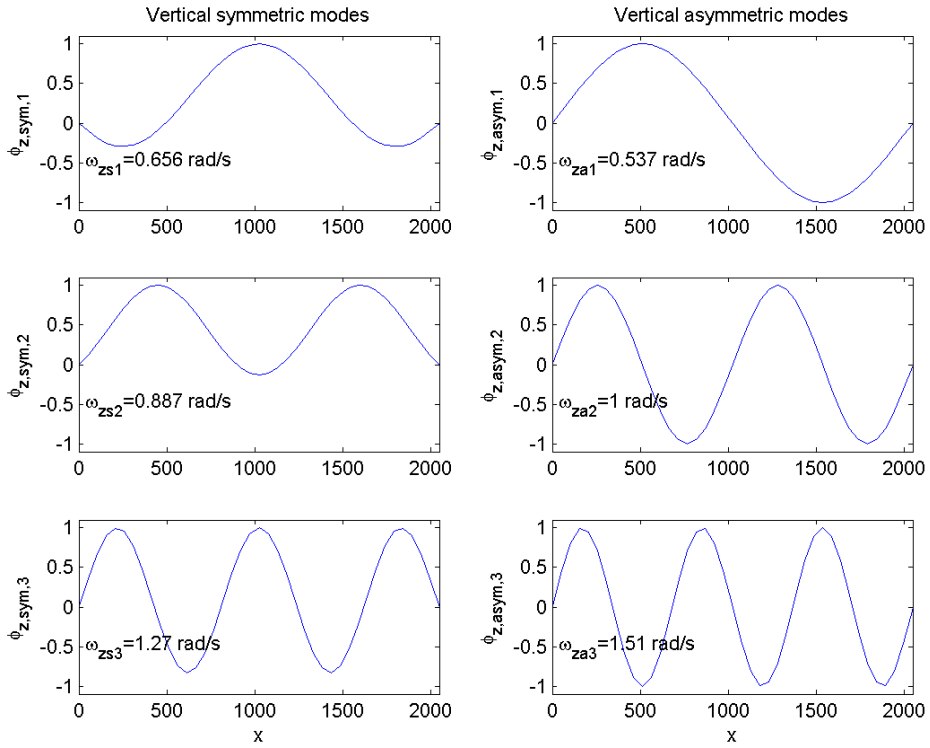

Figure 6.3: Vertical mode shapes for the Halsafjorden bridge

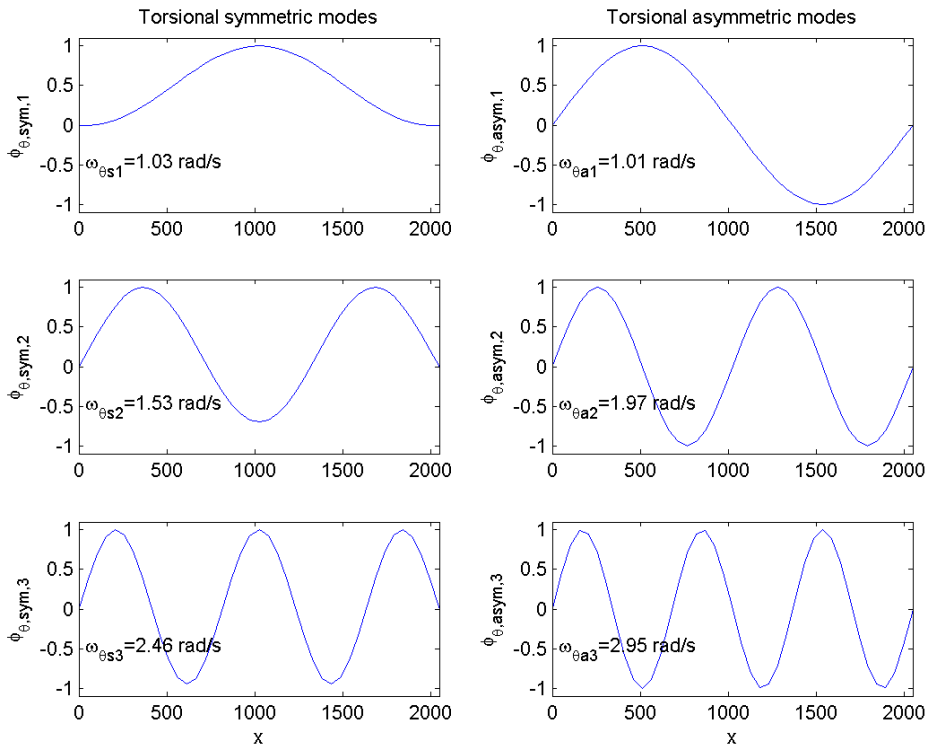

Figure 6.4: Torsional mode shapes for the Halsafjorden bridge

6.3 Dynamic Response Calculations

6.3.1 Analysis Process

The response calculations in this section focus solely on the lowest eigenfrequencies in vertical and torsional motion. From inspection of Figures 6.3 and 6.4 it is seen that the largest deformations occur at $x = L/4 = 512,5\,m$ from each end, and therefore, dynamic response calculations will be pursued at that location. The height of bridge deck is estimated to be $z_f = 50\,m$. The mode shape matrix is given as

$$\mathbf{\Phi} = \begin{bmatrix} \phi_z & 0 \\ 0 & \phi_\theta \end{bmatrix} \tag{6.1}$$

Since the mode shapes have been normalized, the mode shape matrix at the point of interest is given as

$$\mathbf{\Phi}_r(L/4) = \begin{bmatrix} 1 & 0 \\ 0 & 1 \end{bmatrix} \tag{6.2}$$

A short summary of the constants necessary for a numerical calculation of the response of the bridge is provided in Table 3, however most of these have already been presented in previous sections. Note that the reference width B is the width of two box sections.

Table 3: Halsafjorden bridge constants

(a) Bridge properties

ρ [kg/m^3]	$L = L_{exp}$ [m]	B [m]	D [m]	$\tilde{m}_z$ [kg/m]	$\tilde{m}_\theta$ [kgm^2/m]	ω_z [rad/s]	ω_θ [rad/s]	$\zeta_z = \zeta_\theta$ [−]
1,25	2050	22	2,5	19650	2760000	0,537	1,01	0,005

(b) Wind properties at bridge site

I_u [−]	I_w [−]	${}^{x_f}L_u$ [m]	${}^{x_f}L_w$ [m]
0,12	0,047	162	13,5

Additionally, the aerodynamic coefficients $\kappa_{ae_{ij}}$ and $\zeta_{ae_{ij}}$ have already been established in Section 3.7 and the load coefficients in Section 5.3.4.
The spectral density response matrix at $L/4$ is given by

$$\mathbf{S}_{rr}(L/4,\omega) = \begin{bmatrix} S_{r_z r_z} & S_{r_z r_\theta} \\ S_{r_\theta r_z} & S_{r_\theta r_\theta} \end{bmatrix} = \mathbf{\Phi}_r(L/4) \cdot \mathbf{S}_\eta(\omega) \cdot \mathbf{\Phi}_r^T(L/4) \tag{6.3}$$

where $\mathbf{S}_\eta(\omega) = \hat{\mathbf{H}}^*_\eta(\omega) \cdot \mathbf{S}_{\hat{R}}(\omega) \cdot \hat{\mathbf{H}}^T_\eta(\omega)$. In this case, the non-dimensional frequency response function from Eq. 3.43 reduces to

$$\hat{\mathbf{H}}_\eta(\omega) = \left\{ \begin{bmatrix} 1 & -\kappa_{ae_{z\theta}} \\ 0 & 1-\kappa_{ae_{\theta\theta}} \end{bmatrix} - \omega^2 \begin{bmatrix} \omega_z^{-2} & 0 \\ 0 & \omega_\theta^{-2} \end{bmatrix} + 2i\omega \begin{bmatrix} \omega_z^{-1} & 0 \\ 0 & \omega_\theta^{-1} \end{bmatrix} \begin{bmatrix} \zeta_z - \zeta_{ae_{zz}} & -\zeta_{ae_{z\theta}} \\ -\zeta_{ae_{\theta z}} & \zeta_\theta - \zeta_{ae_{\theta\theta}} \end{bmatrix} \right\}^{-1} \tag{6.4}$$

The modal load matrix is defined by

$$\mathbf{S}_{\hat{R}}(\omega) = \begin{bmatrix} S_{\hat{R}_z\hat{R}_z} & S_{\hat{R}_z\hat{R}_\theta} \\ S_{\hat{R}_\theta\hat{R}_z} & S_{\hat{R}_\theta\hat{R}_\theta} \end{bmatrix} \qquad \text{where} \quad S_{\hat{R}_n\hat{R}_m}(\omega) = \frac{\rho B^3}{2\tilde{m}_n}\frac{\rho B^3}{2\tilde{m}_m}\left(\frac{V}{B\omega_n}\right)^2\left(\frac{V}{B\omega_m}\right)^2 \hat{J}^2_{nm} \tag{6.5}$$

$n, m = z \text{ or } \theta$. $\hat{J}^2_{nm}$ is the reduced joint acceptance function, who's general expression is given in Eq. 3.54. In this situation, the expression is reduced to the following:

$$\hat{J}^2_{zz} = \iint_{L_{exp}} \phi_z(x_1)\phi_z(x_2)\left[\left(2\bar{C}_L\right)^2 I_u^2 \hat{S}_u \hat{C}o_{uu}(\omega,\Delta x) + \left(C'_L + \frac{D}{B}\bar{C}_D\right)^2 I_w^2 \hat{S}_w \hat{C}o_{ww}(\omega,\Delta x)\right] dx_1 dx_2 / \left(\textstyle\int_0^L \phi_z^2 dx\right)^2$$

$$\hat{J}^2_{z\theta} = \iint_{L_{exp}} \phi_z(x_1)\phi_\theta(x_2)\left[4\bar{C}_L B\bar{C}_M I_u^2 \hat{S}_u \hat{C}o_{uu}(\omega,\Delta x) + \left(C'_L + \frac{D}{B}\bar{C}_D\right) BC'_M I_w^2 \hat{S}_w \hat{C}o_{ww}(\omega,\Delta x)\right] dx_1 dx_2 / \left(\textstyle\int_0^L \phi_z^2 \int_0^L \phi_\theta^2 dx\right)$$

$$\hat{J}^2_{\theta\theta} = \iint_{L_{exp}} \phi_\theta(x_1)\phi_\theta(x_2)\left[\left(2B\bar{C}_M\right)^2 I_u^2 \hat{S}_u \hat{C}o_{uu}(\omega,\Delta x) + \left(BC'_M\right)^2 I_w^2 \hat{S}_w \hat{C}o_{ww}(\omega,\Delta x)\right] dx_1 dx_2 / \left(\textstyle\int_0^L \phi_\theta^2 dx\right)^2$$

$$\hat{J}_{\theta z} = \hat{J}_{z\theta} \tag{6.6}$$

Since this is a numerical analysis, the reduced joint acceptance functions must be obtained by numerical integration in the form of a double summation. The integrals $\iint_{L_{exp}} \phi_n(x_1)\phi_m(x_2)\hat{C}o_{uu}dx_1dx_2$ and $\iint_{L_{exp}} \phi_n(x_1)\phi_m(x_2)\hat{C}o_{ww}dx_1dx_2$ in the above equation can be found numerically by [22]

$$I(\beta) = \frac{1}{N^2} \sum_{n=1}^{N} \sum_{m=1}^{N} \phi_i(\hat{x}_n)\, \phi_j(\hat{x}_m) \cdot exp(-\beta \cdot \Delta\hat{x}) \tag{6.7}$$

where $\Delta\hat{x} = |\hat{x}_n - \hat{x}_m|$, N is the number of integration points and $\beta = C_{kx}\omega L_{exp}/V$ with $k = u$ or w. It is assumed that $C_{ux} = 9/(2\pi)$ and $C_{wx} = 6/(2\pi)$. Substituting $I(\beta)$ into the relevant equations for the joint acceptance function we get

$$\hat{J}^2_{zz} = L^2 \left[\left(2\bar{C}_L\right)^2 I_u^2 \hat{S}_u I_{u,zz}(\beta) + \left(C'_L + \frac{D}{B}\bar{C}_D \right)^2 I_w^2 \hat{S}_w I_{w,zz}(\beta) \right] \Bigg/ \left(\int_0^L \phi_z^2 dx \right)^2 \tag{6.8}$$

$$\hat{J}^2_{z\theta} = L^2 \left[4\bar{C}_L B \bar{C}_M I_u^2 \hat{S}_u I_{u,z\theta}(\beta) + \left(C'_L + \frac{D}{B}\bar{C}_D \right) B C'_M I_w^2 \hat{S}_w I_{w,z\theta}(\beta) \right] \Bigg/ \left(\int_0^L \phi_z^2 \int_0^L \phi_\theta^2 dx \right) \tag{6.9}$$

$$\hat{J}^2_{\theta\theta} = L^2 \left[\left(2B\bar{C}_M\right)^2 I_u^2 \hat{S}_u I_{u,\theta\theta}(\beta) + \left(BC'_M \right)^2 I_w^2 \hat{S}_w I_{w,\theta\theta}(\beta) \right] \Bigg/ \left(\int_0^L \phi_\theta^2 dx \right)^2 \tag{6.10}$$

Having now defined the necessary parameters to calculate the spectral density response matrix $\mathbf{S}_{rr}$, we obtain the corresponding covariance matrix by frequency domain integration

$$\mathbf{Cov}_{rr}(x_r = L/4) = \int_0^\infty \mathbf{S}_{rr}(L/4, \omega)\, d\omega = \begin{bmatrix} \sigma^2_{r_z r_z} & Cov_{r_z r_\theta} \\ Cov_{r_\theta r_z} & \sigma^2_{r_\theta r_\theta} \end{bmatrix} \tag{6.11}$$

6.3.2 Analysis Results

Following the procedure in Section 6.3.1, the response analysis of the Halsafjorden bridge at response location $x_r = L/4$ along the bridge is performed in MATLAB. Figure 6.5 shows the resulting standard deviation of the dynamic response in the vertical across wind direction z and in torsion θ at various mean wind velocities, as well as their covariance coefficient and the mean wind dependent resonance frequencies associated with the lowest modes in z and θ.

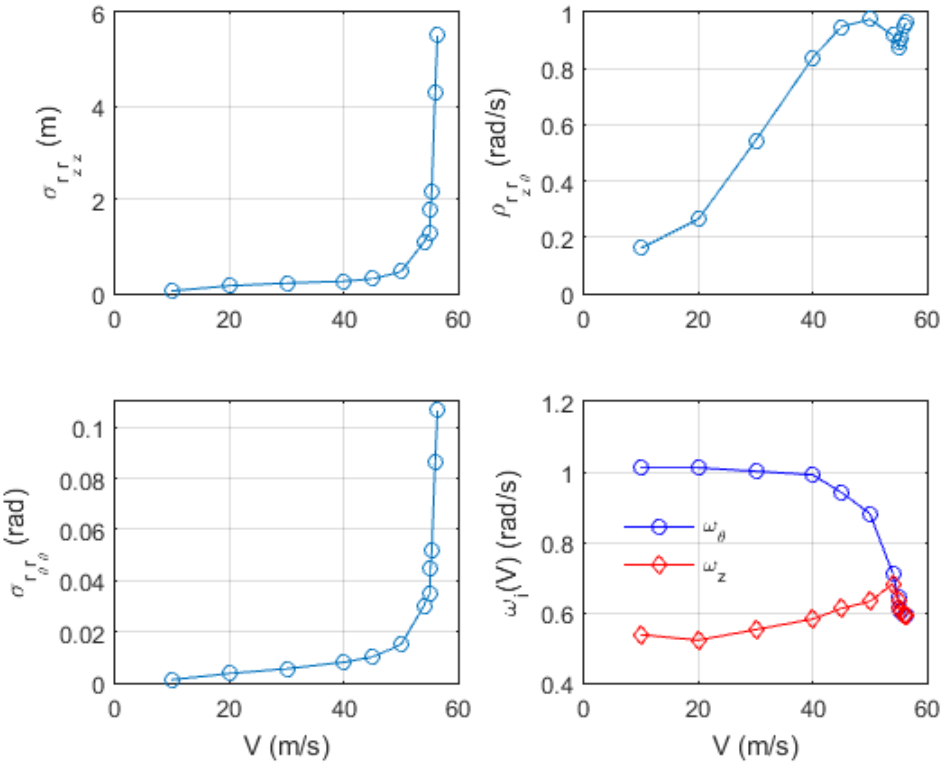

Figure 6.5: Top and lower left: Dynamic response at $L/4$. Top right: covariance coefficient. Lower right: resonance frequencies associated with the lowest modes in vertical direction and torsion

A stability limit, where there is large increase in displacement for a small increase in mean wind velocity, is seen to be reached at a mean wind velocity of slightly below 60 m/s, more specifically, at approximately $V_{cr} = 56,4$ m/s. For comparison, Selberg's formula (Eq. 3.81) gives a critical mean wind velocity of $V_{cr} = 47,36$ m/s. This number is notably lower, however, Selberg's formula is only used to provide a first estimate and thus should not be viewed as a concrete solution. It should be noted that the value found for the critical mean wind velocity is lower than the requirement set in Section 5.5, $V_{cr} = 56,4 < V_{cr,min} = 59,4$ m/s. However, the value for $V_{cr,min}$ is given for a wind field with a return period of 500 years, and as such includes safety factors. Since the difference between the calculated V_{cr} and the required $V_{cr,min}$ is only 3 m/s, it should be investigated further if this is acceptable. However, this is outside of the scope of this thesis. The covariance coefficient $\rho_{r_z r_\theta}$ approaches 1 as the mean wind velocity increases, which indicates modal coupling. This coupling combined with the large increase in displacement indicates flutter instability. It is noticeable that the $\rho_{r_z r_\theta}$ curve makes a small drop when the modes start to couple. A reasonable explanation for this was not found in the writing of this thesis, however it might simply be a numerical issue. Modal coupling is seen even more clearly in the lower right diagram of Figure 6.5, which shows coupling occur already at $V = 55,2$ m/s, at which point the resonance frequencies begin oscillating at

the same frequency. By comparison with the response diagrams (upper and lower left), we see that as the two modes have coupled the response starts to drastically increase until a stability limit is reached. From the lower right diagram it is further seen that the torsional resonance frequency ω_θ is gradually reduced for higher values of mean wind velocity, while ω_z increases, but at a slower rate. This complies well with the theory of flutter, which gives that the aerodynamic forces associated with the motion in torsion are the main driving forces for modal coupling. The dominance of the torsional eigenmode is also evident as the coupled modes seem to follow the declining curve of the torsional mode.

Figure 6.6 shows the development of the absolute value of the determinant of the frequency response function for selected mean wind velocities. Since the frequency response function describes the relationship between the input and the output of the system (see Section 2.1.2), which in this case are the wind loading and the response of the structure, the peaks will be located at the points where response is the highest, namely at the resonance frequencies. The first peak represents the response relationship at the lowest vertical eigenfrequency, and the second peak at the lowest torsional eigenfrequency. It is seen that the peaks move closer together with increasing wind velocity, as they should, since the torsional eigenfrequency is reduced with larger wind velocities while the vertical eigenfrequency is increased. It is seen that the peaks are reduced with higher wind velocities (excluding velocities close to the stability limit). This is largely due to the effects of aerodynamic damping. It is interesting to note that close to the stability limit the two frequencies have coupled, and the eigenmodes will work together and produce only one peak. This peak is however larger than the original peaks at $V = 0$ m/s. Even though total damping has increased at this point due to motion induced effects, the two modes now work together and the response becomes considerably larger. The tail of the frequency response function has been lifted at the wind velocity close to the stability limit, which is caused by reduced stiffness.

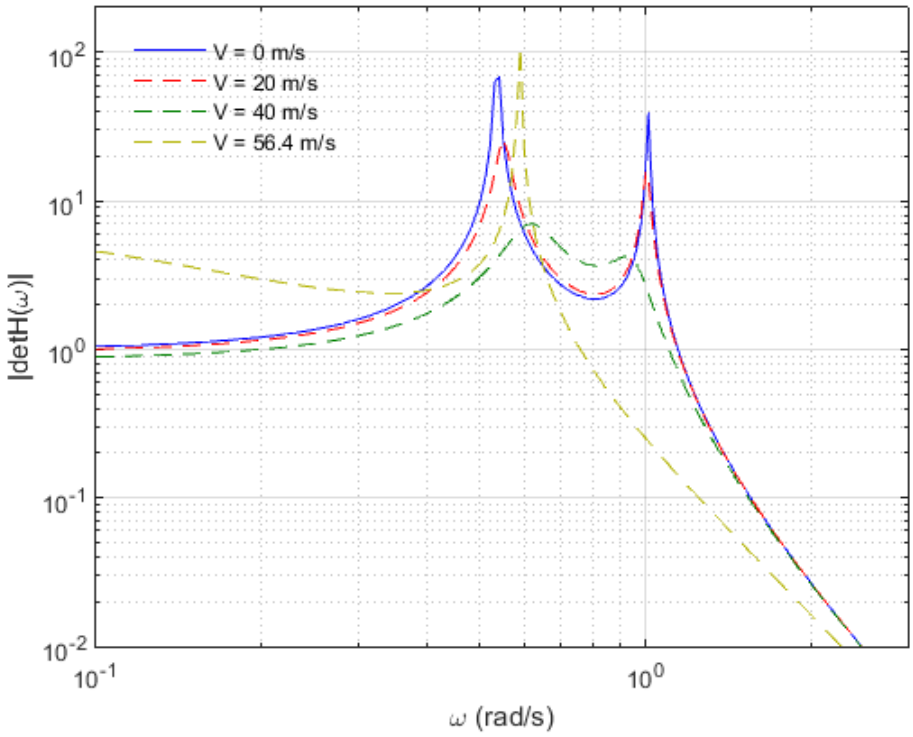

Figure 6.6: The absolute value of the determinant of the frequency response function at chosen mean wind velocities

For further analysis, the components of the frequency response function are presented in Figure 6.7. By comparing H_{22} with H_{11} it becomes more apparent how much a greater impact the torsional aerodynamic forces have on the stability limit, since the peak of H_{22} moves by a much greater amount. It is also apparent that the system loses torsional stiffness since the tail of H_{22} has increased at $V \approx V_{cr}$, while it gains a little bit of vertical stiffness since the tail of H_{11} is lowered by a small amount. The peaks of both H_{11} and H_{22} at $V \approx V_{cr}$ are increased beyond the original peak due to the considerable increase in response. H_{12} gives even more evidence of modal coupling and the largely increasing tail of the function indicates a large loss of stiffness between the cross terms due to aerodynamic effects. Figure 6.8 gives a comparison between the spectral density at a wind velocity of $V = 30$ m/s and at $V_{cr} = 56,4$ m/s. At 30 m/s there are two clear peaks in the spectral densities, including the cross spectrum between vertical and torsion response components. However, as in the determinant of the frequency response function, there is only one large peak at the critical mean wind velocity.

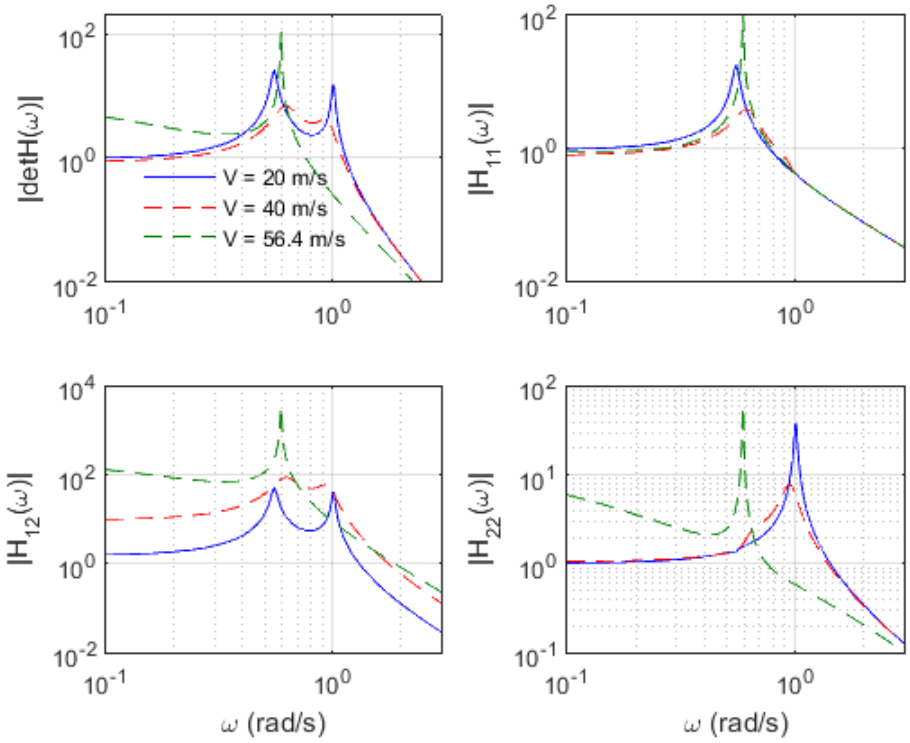

Figure 6.7: Each component of the frequency response function

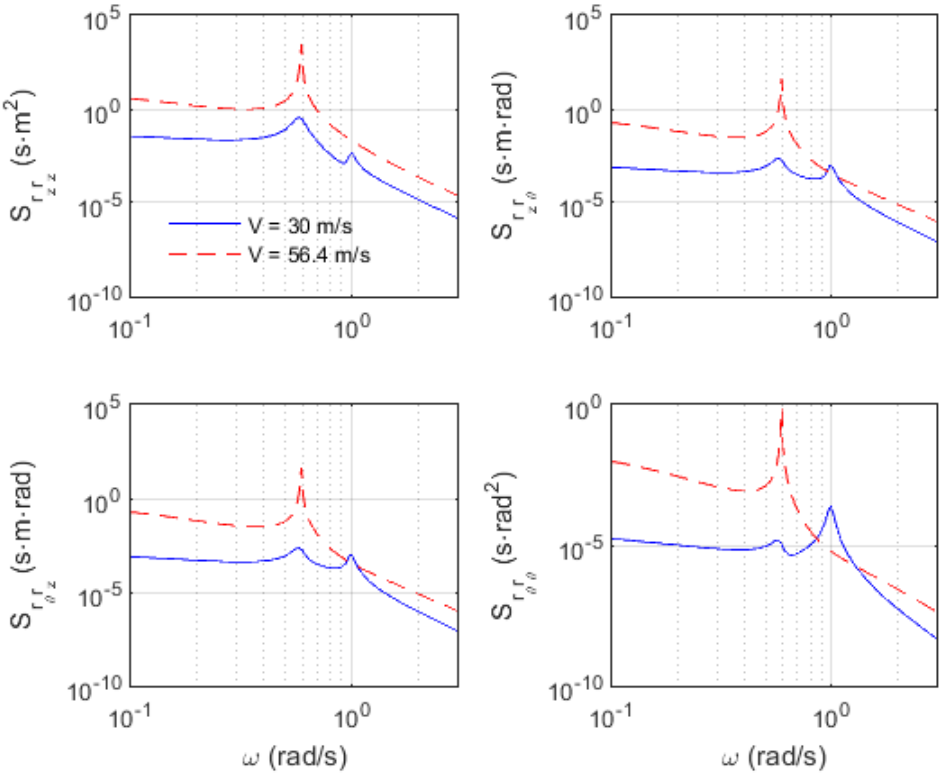

Figure 6.8: Spectra of response components in vertical direction, torsion and cross spectrum

Time series simulations (see Section 2.3.5) of the dynamic response at a point located at $x = L/4$ along the span at both $V = 30$ m/s and $V_{cr} = 56,4$ m/s are given in Figures 6.9 and 6.10, respectively. Note that these are only two realisations of the process, and no two realisations will be unique. By comparing the two figures we see the effects that the motion induced forces have on the response. Close to the stability limit, at $V_{cr} = 56,4$ m/s, the dynamic response of the structure is much greater than at $V = 30$ m/s, reaching up to about 10 m vertical deformation and a cross sectional rotation of over 0,2 rad $\approx 11,46°$. It is also seen that the vertical deformation becomes more narrow banded, as its frequency has increased, while the torsional deformation has become more broad banded since its frequency has decreased.

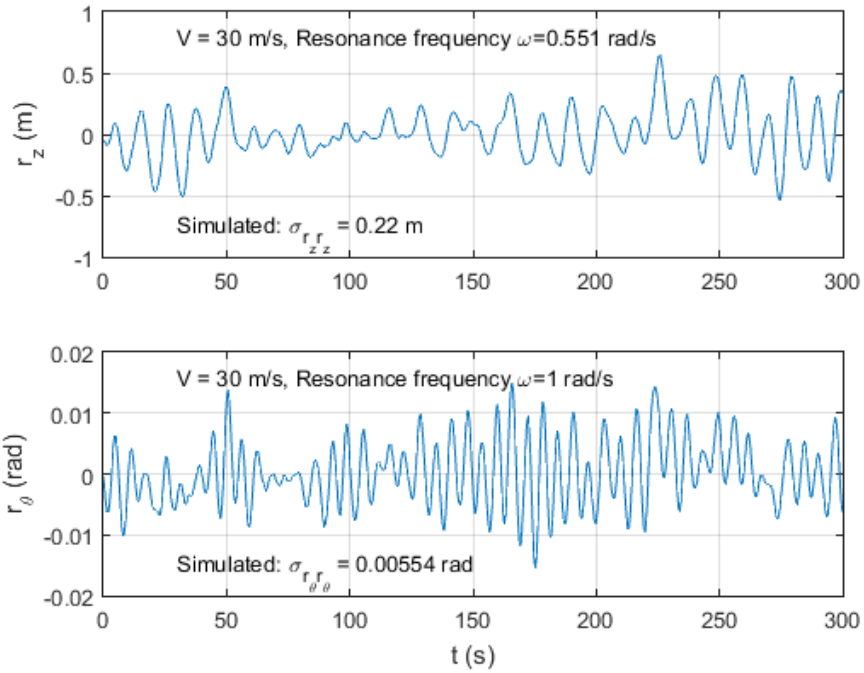

Figure 6.9: Time domain simulation of dynamic response at $x = L/4$ and $V = 30$ m/s

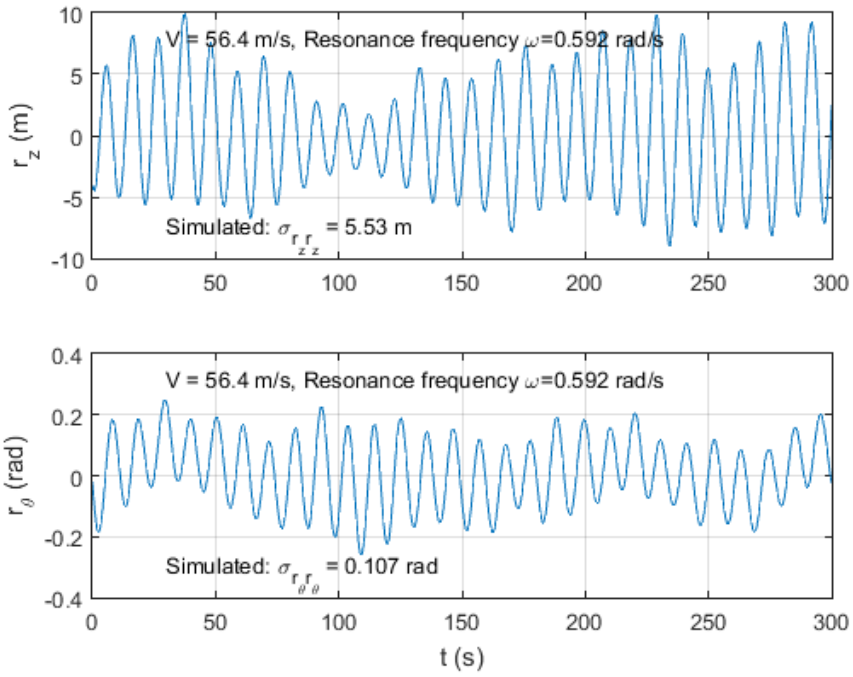

Figure 6.10: Time domain simulation of dynamic response at $x = L/4$ and critical mean wind velocity $V_{cr} = 56,4$ m/s

6.3.3 Parameter Study

This section is intended to study what effects the aerodynamic derivatives have on the system in terms of response, stiffness and damping. The aerodynamic derivatives are shown graphically in Figure 5.5

The aerodynamic derivatives have the effect of changing the total damping and stiffness of the combined structure and flow system. Figure 6.11 shows the development of the total damping and aerodynamic stiffness and damping coefficients with increasing mean wind velocities. The upper left diagram shows how both the total torsional damping and vertical damping are increased. This explains why the peaks in the frequency response function (Figure 6.6) appears to be almost damped out. It is also noticeable that the torsional damping increases by a much greater extent than the vertical damping. With reference to Eq. 3.60 - 3.63 we can see which aerodynamic derivatives cause changes in which aerodynamic coefficients. H_1^* is what affects $\zeta_{ae_{zz}}$ and thus affects the total vertical damping, $\zeta_{z,tot} = \zeta_z - \zeta_{ae_{zz}}$. In this case, H_1^* is negative and increasing which in turn makes $\zeta_{ae_{zz}}$ negative and increasing. This has the effect of increasing the total vertical damping, and thus reduce the vertical response peak. In the same manner, A_2^* causes an increase in torsional damping and a reduction of the torsion peak as it is negative as well. The upper right diagram shows the development of the aerodynamic stiffness coefficients $\kappa_{ae_{zz}}$ and $\kappa_{ae_{\theta\theta}}$. The diagram shows that $\kappa_{ae_{\theta\theta}}$ is always positive and increasing, which means it contributes to loss of stiffness in the system. It is important to note that $\kappa_{ae_{\theta\theta}}$ eventually

increases even beyond a value of 1, at which point the system has theoretically lost all its stiffness in torsion, making way for large torsional deformations. The vertical aerodynamic stiffness coefficient $\kappa_{ae_{zz}}$ however quickly attains negative values, giving increasing total vertical stiffness. This is why the torsional eigenfrequency is decreased with increasing mean wind velocity, and why the vertical eigenfrequency is increased. This corresponds well with the frequency response function and the discussion in Section 6.3.2. The cross damping terms $\zeta_{ae_{z\theta}}$ and $\zeta_{ae_{\theta z}}$ are shown in the lower left diagram, while the cross stiffness terms $\kappa_{ae_{z\theta}}$ and $\kappa_{ae_{\theta z}}$ are shown in the lower right diagram. It is apparent that $\zeta_{ae_{\theta z}}$ and $\kappa_{ae_{\theta z}}$ can be considered negligible in comparison with $\zeta_{ae_{z\theta}}$ and $\kappa_{ae_{z\theta}}$, which means that the torsional velocity and displacement are the clear driving forces for coupling motion. There is a notch in the blue curve in the lower diagrams. This is likely due to numerical issues and it is more plausible the development should look like a continuous curve.

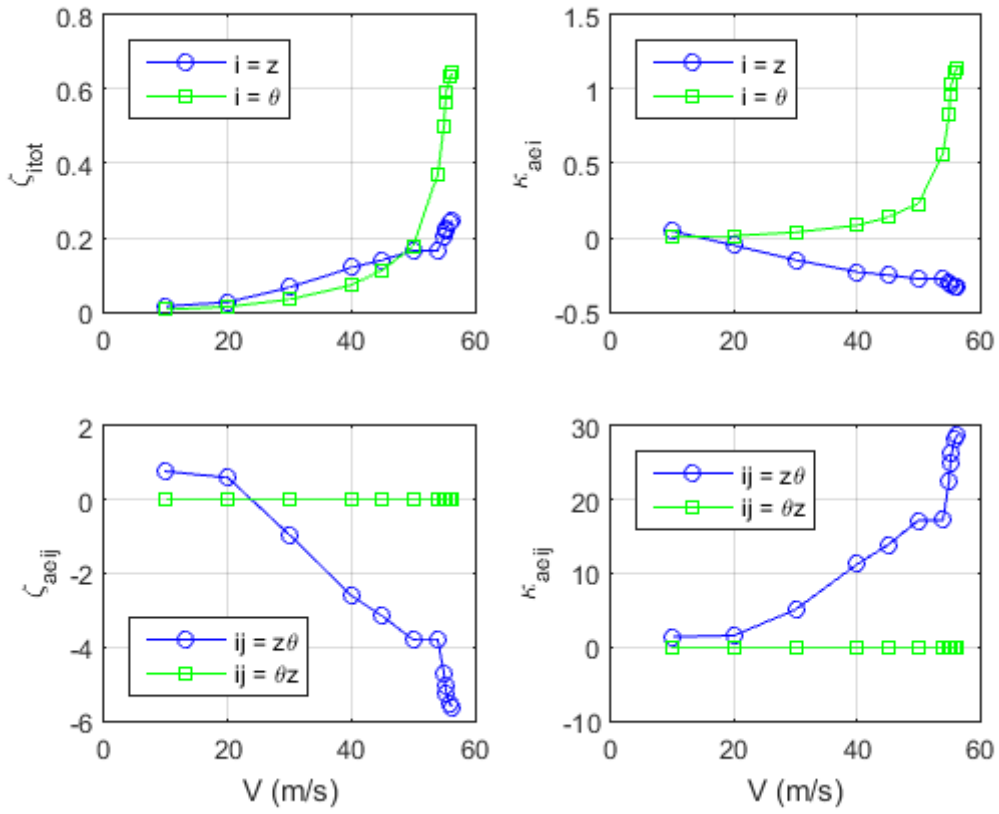

Figure 6.11: Development of total damping and aerodynamic stiffness contributions

The effects of the aerodynamic derivatives on the stability limit are investigated by performing the response calculations and setting the particular aerodynamic derivative to be studied as half its original value, and double its original value, respectively. The result of this parameter study is presented in Figures 6.12 and 6.13. It is seen that A_3^* has the biggest effect on the stability limit by far. As A_3^* takes half its original value, the stability limit has increased to over 66 m/s. At double its original value, A_3^* has caused the

stability limit to drop to around 45 m/s. Since A_3^* affects $\kappa_{ae_{\theta\theta}}$, this change is due to loss or increase of torsional stiffness. When A_3^* becomes larger, so does $\kappa_{ae_{\theta\theta}}$ and the system loses torsional stiffness, giving a stability limit at a lower mean wind velocity. The reverse is true for a smaller A_3^*. This indicates that the stability limit is mainly caused by motion induced loss of torsional stiffness. The more torsional stiffness the system loses, the faster the torsional eigenfrequency drops to the same value as the vertical eigenfrequency.

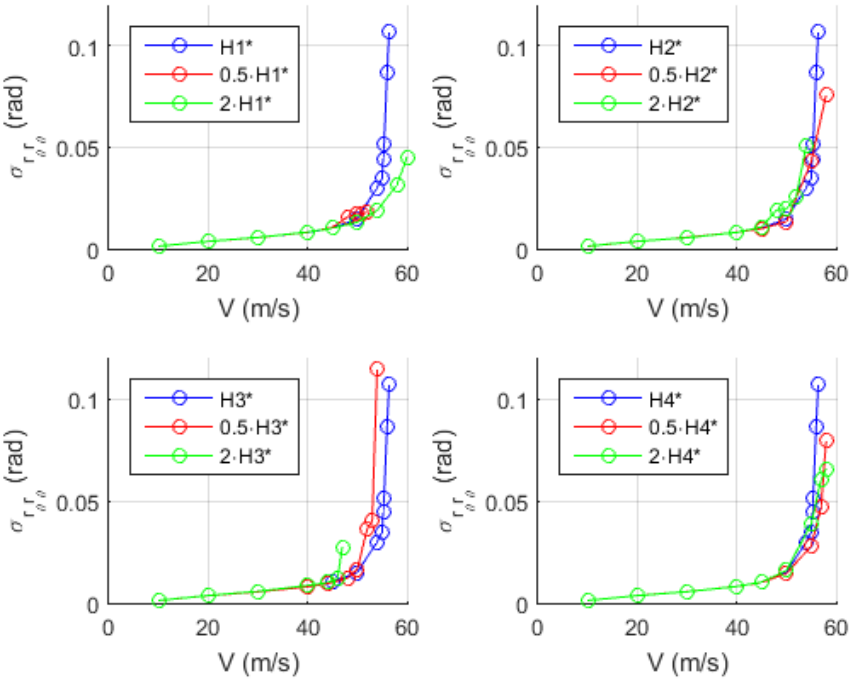

Figure 6.12: Effects of the variation of aerodynamic derivatives on the torsional response

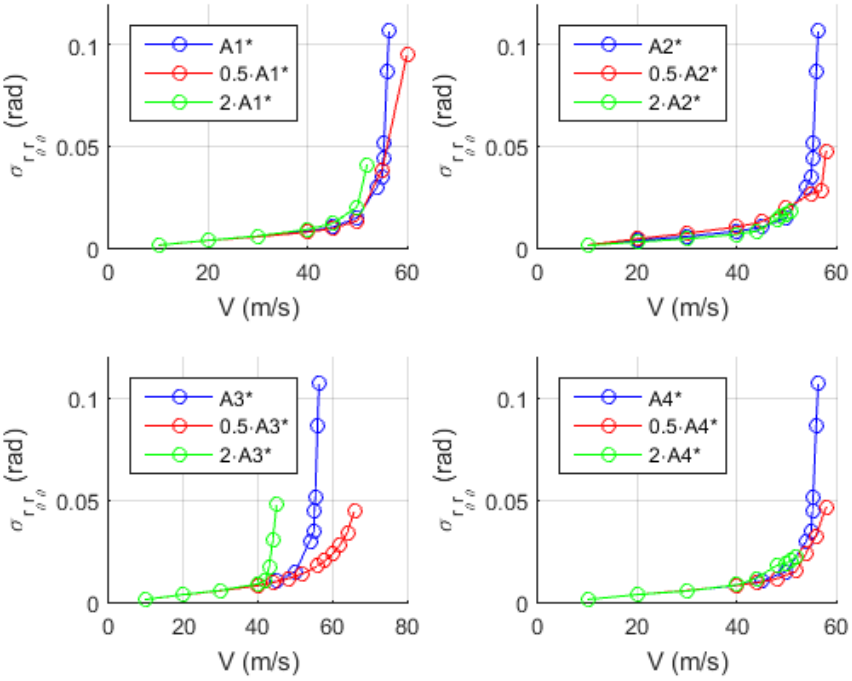

Figure 6.13: Effects of the variation of aerodynamic derivatives on the torsional response

6.4 Stability Limits

As discussed in Section 3.7 there are four different types of motion induced instabilities that can occur in a bridge section, identified by the type of response that develops. In this section they will be discussed with reference to the Halsafjorden bridge.

Since static divergence is purely a static problem of losing torsional stiffness, the quasi-static version of A_3^* may be used, $A_3^* = C_M' \left(\frac{V}{B\omega_i(V)}\right)^2$. A static divergence stability limit is identified by $1 - \kappa_{ae_{\theta\theta}} = 0$. With reference to Eq. 3.61 using the quasi-static version of A_3^* it is seen that a stability problem will never occur for a negative C_M'. In the case of the Halsafjorden bridge section, $C_M' = -1,540$ and therefore static divergence is not an issue.

Similarly, and as explained in Section 3.7.2, galloping instability can only occur if H_1^* attains positive values. For the Halsafjorden bridge section H_1^* is purely negative, and as such, galloping instability will not occur.

Since $\zeta_\theta - \zeta_{ae_{\theta\theta}} = 0$ is a requirement for dynamic instability in torsion, if A_2^* is always negative, ζ_θ and $\zeta_{ae_{\theta\theta}}$ will always have the same sign and therefore this equation will never equate to zero. Therefore dynamic instability in torsion will not occur in the Halsafjorden bridge section.

The last type of instability, flutter, can however occur. A flutter instability limit has already been identified in Section 6.3.2 using dynamic response calculations. Another method is the one described in Section 3.7.4, where it is assumed that the flutter instability

limit occurs at frequencies where $\omega_r = \omega_\theta(V_{cr}) = \omega_z\,(V_{cr})$, i.e. where the lowest shape-wise similar vertical and torsional eigenfrequencies have coupled. It has been found that the mode shapes used in this analysis, ϕ_z and ϕ_θ, are shape-wise similar such that $\phi_z \approx \phi_\theta$. To calculate the stability limit based on this assumption, a self made MATLAB program was used and can be found in Appendix B. The program determines when the roots of the real part of the impedance matrix are equal to the roots of the imaginary part, i.e. finds if there are values of ω_r for which both $\mathrm{Re}\left(\det\left(\hat{\mathbf{E}}_\eta\right)\right) = 0$ and $\mathrm{Im}\left(\det\left(\hat{\mathbf{E}}_\eta\right)\right) = 0$ simultaneously. The result is presented in Figure 6.14, where a solution is found at a point where the two lines intersect. It is seen that even though the roots come close to being equal, they are never fully equal. For comparison, the dynamic response calculations found that the vertical and torsional eigenfrequencies couple at $V = 55,2$ m/s, translating to a reduced mean wind velocity of about $\hat{V} = 4,10$, while the stability limit was identified at $V = 56,4$ m/s, or $\hat{V} = 4,33$. At this $\hat{V}$ interval, the roots in Figure 6.14a are very closely spaced. Figure 6.14b gives a closer look at the interval where the resonance frequencies are close to coupled. It is seen that the difference between them at their closest point is about $\Delta\omega = 0,008$ rad/s. Due to this low margin, it can be concluded that according to this method, a flutter instability has a high risk of occurring.

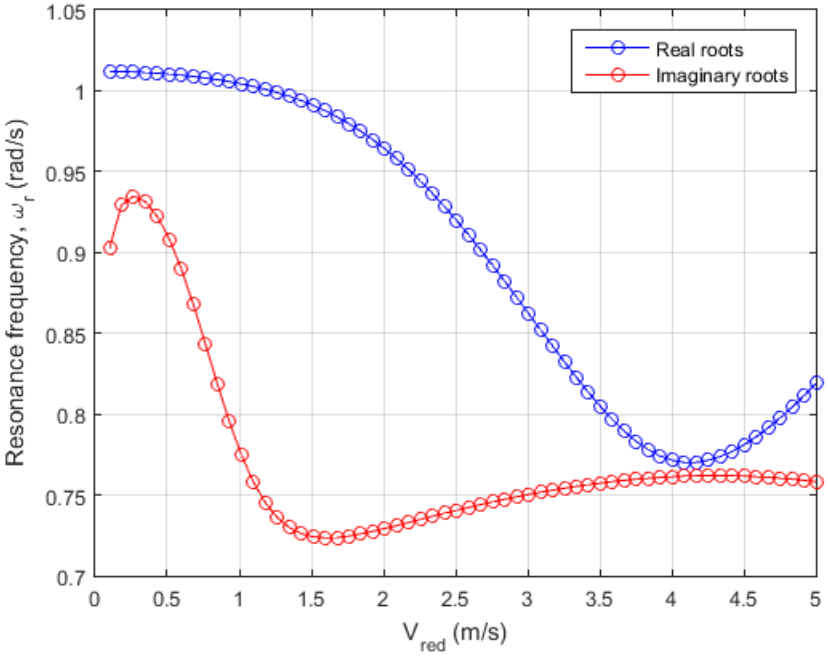

(a) Development of the real and imaginary roots of the impedance matrix

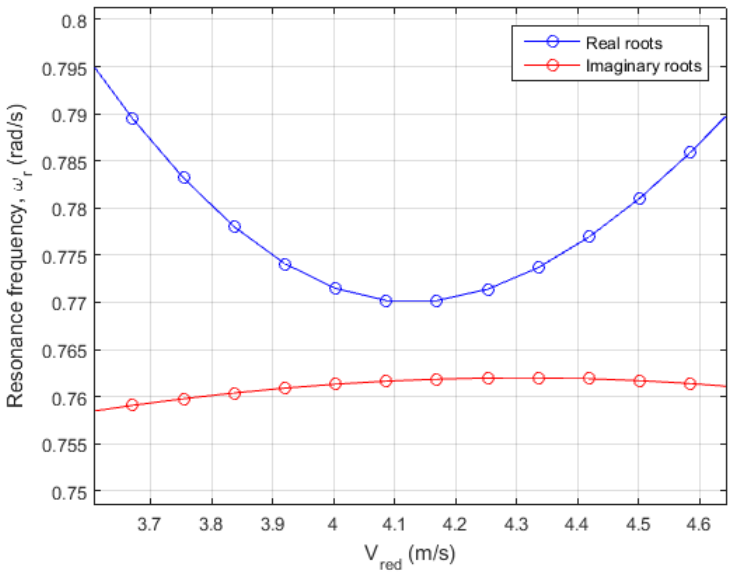

(b) A closer look at the most critical velocity range

Figure 6.14: Flutter analysis of the Halsafjorden bridge section

6.5 Control of Wind Induced Response

If a structure is found not to meet the aerodynamic requirements imposed on it, there are several ways of controlling the response either by reducing the response directly or changing relevant design parameters to increase the stability limit.

While early in the design phase, the possibility of adjusting the geometrical shape of the deck is feasible. This is done to obtain a more aerodynamic cross section with the aim

of decreasing drag forces and increasing the stability limit. The easiest way to improve aerodynamic performance of a bridge deck is usually to reduce the height of the deck edge, since both flutter and vortex shedding are sensitive to the height-to-width ratio of the deck. This reduction must however be within reasonable practical limits. Alternatively, edge treatments such as deck extensions and fairings can be used to improve the aerodynamic performance of the deck [23].

Additionally, increasing the stiffness of the bridge deck will also lead to improved aerodynamic performances, especially important if the bridge is subject to loss of stiffness due to motion induced loads. By increasing the torsional stiffness, the torsional resonance frequency will increase, thus contributing to decreasing the risk of coupling between the two modes. However, increasing the stiffness of the deck may prove expensive, especially for very long spans. Other avenues may be explored as well, such as increasing the distance between the main cable planes, increasing the centre-to-centre distance between the box girders, adjusting the cable sag, and the addition of stay cables [1].

Aerodynamic optimization of the bridge deck can be performed in wind tunnel tests, with the purpose of reducing the motion induces loads acting on the deck. The drag forces should be kept as low as possible as they will be transferred from the deck and to the top of the towers, producing moment loading. The slopes of the moment and lift coefficients (C_M' and C_L') are very important to avoid instability and increase flutter velocity. Preferably they should be as much as possible lower than the values of a flat plate, $\pi/2$ and 2π respectively, to increase the flutter velocity stability limit [5]. It is noted that for the proposed Halsafjorden bridge section, C_M' is negative and close to equal to $-\pi/2$. A smaller number would decrease A_3^*, which as seen in Figure 6.13 would increase the stability limit considerably. Furthermore, a positive A_3^* produces positive aerodynamic torsional stiffness which decreases the total torsional stiffness in the combined structure and flow system, and lowers the torsional frequency until it coincides with the vertical one, as was seen in the previous sections. Performing aerodynamic optimization of the deck in wind tunnel tests makes it possible to identify a deck cross section with a more favourable C_M'. In this particular case, since C_M' affects A_3^* which has great influence on the stability limit as discussed in Section 6.3.3, this might be a feasible course of action.

A highly effective method of controlling the dynamic response, is to increase the damping in the bridge. Damping is a complicated phenomenon and difficult to estimate, yet a significant part of structural design due to the large effect it can have on the structural response. There are several different damping mechanisms that can occur in a structure, such as material damping, which occurs in the material itself on a molecular level, frictional damping between structural members and connections in mechanical joints and supports in the system, damping due to energy dissipation mechanisms in the foundation, and aerodynamic damping. There are several types of dampers available to increase damping in the system and mitigate the structural response. Inertial dampers, such as the tuned

mass dampers, absorb vibration by utilizing inertial effects. The damping added to the system does not stem from energy dissipation, but rather from modification of the building frequency response. This works as the damper masses are tuned to be out of phase with the response, and hence interrupt the response vibration. A tuned mass damper consists of an additional mass that is attached to the main system through a spring and a dashpot. Therefore the system is represented as a 2 degree of freedom system. The frequency of this mass is tuned to a particular structural frequency. When that frequency is excited, the damper resonates out of phase with the structural motion. This effect can be seen clearly on the frequency response function of the system, as the resonance peak is reduced and replaced by two smaller peaks corresponding to the two modal frequencies of the new 2 degree of freedom system. Another notable type of dampers are viscous fluid dampers, which exploit the properties of highly viscous materials in order to develop resisting forces that are proportional to the body's velocity and act in the opposite direction of the body's movement. Friction dampers dissipate energy directly through frictional mechanisms and allow for plastic behaviour to occur in selected regions of a structure. They are designed to have a fixed slipping load, and when this load is reached in the structure, the damper activates and two surfaces dissipate energy by slipping on each other. Note that this is plastic deformation, and hence not reversible [23].

6.6 Further Discussion

In the analysis performed in this thesis there are many factors that could contribute to inaccuracies in the model and the results. With such a complex structure, a vast number of mechanical properties, dimensions, and geometric shapes in all parts of the bridge come into play, as well as experimental values obtained from wind tunnel tests. All of these variables affect the dynamic behaviour of the bridge. For computational efficiency as well as cost and time constraints, various assumptions and simplifications have been made in the bridge calculation model, which means the result will not be entirely accurate. A stability limit was not explicitly identified by investigation of the real and imaginary parts of the impedance matrix, however, the resonance frequencies were found to be very closely spaced at the same velocity range as the stability limit that was identified using response calculations. The possibility of a stability limit at this velocity range must therefore be considered. Moreover, this analysis was based only on the two lowest modes while a full multi-mode analysis would provide more accurate results, and a more complete description of the stability limits. It should be noted that in recent years it has been found that a flutter stability limit can occur even before $\omega_\theta(V_{cr}) = \omega_z(V_{cr})$, so a search for stability limits based on that assumption may be unreliable. In such a case, a flutter stability limit should be identified through response calculations instead.

7 Conclusions

The aim of this thesis was to investigate motion induced instability in long, slender suspension bridges by identification of stability limits, and to study which aerodynamic derivatives have the greatest influence on said stability limits. A case study was performed on one bridge in particular, the proposed Halsafjorden bridge. The bridge has a main span of 2050 meters, and a dual box girder deck with each girder supporting a roadway and a walking path. The bridge may therefore be considered as slender.

A simplified model of the bridge was set up where it was assumed that the bridge behaves as combination of two cables and a beam. This simplification can cause some inaccuracies in the calculations, and is but one side of the design process. The relevant load coefficients were extracted from wind tunnel test, and the aerodynamic derivatives calculated from indicial functions.

The dynamic response analysis allowed for the identification of a stability limit at $V_{cr} = 56,4$ m/s for the lowest modes in vertical direction and torsion. This number is lower than the requirement set by [13], $V_{cr,min} = 59,4$ m/s. Therefore either adjustments should be made to the bridge design or external control mechanisms should be applied to fulfil this requirement.

In the analysis of the impedance matrix it was determined that the only type of instability that will occur in this bridge is flutter. However, a flutter stability limit was not explicitly identified by this method. The two eigenfrequencies investigated were however dangerously close to being equal at a certain velocity range. By comparing these results with the result from the dynamic response analysis it is found that this critical velocity range is similar in both cases, making a strong case for adopting the result from the response analysis to air on the safe side, rather than the results from the impedance matrix analysis.

As was seen, A_3^* has a large effect on the stability limit, and therefore accurate prediction of the aerodynamic derivatives in wind tunnel tests is of great importance to correctly predict stability limits. As A_3^* increases, $\kappa_{ae_{\theta\theta}}$ increases as well which gives the system lower total torsional stiffness and causes its torsional eigenfrequency to decrease. The torsional eigenfrequency ω_θ was found to be the main driving force for modal coupling, which explains the large effect of A_3^* on the stability limit. Even though the system was found to gain increased damping for increasing mean wind velocities, the frequency response function shows only one peak, which is larger than the two peaks at $V = 0$. This is due to considerably larger deformations and the cooperation between the vertical and torsional modes.

8 Bibliography

[1] Astiz, M. A. (1998). Flutter Stability of Very Long Suspension Bridges. *Journal of Bridge Engineering*, 3(3), 132-139. Springer, 1. edition.

[2] Chobsilprakob, P., Kim, K.-D., Suthasupradit, S. and Manovachirasan, A. (2014). Application of Indicial Functions for the Flutter Analysis of Long Span Suspension Bridge During Erection. *International Journal of Steel Structures*, 14(1), 185-194.

[3] Chopra, A. K. (2011). *Dynamics of Structures - Theory and Applications to Earthquake Engineering.* Pearson Prentice Hall, 4. edition.

[4] Dahlen, A. and Lystad, T. M. (2013). *Instrumentering av Bergsøysundbrua og Gjemnesundbrua.* Master's thesis, Norwegian University of Science and Technology, Trondheim.

[5] Diana, G., Fiammenghi, G., Belloli, M. and Rocchi, D. (2013). Wind Tunnel Tests and Numerical Approach for Long Span Bridges: the Messina Bridge. *Journal of Wind Engineering and Industrial Aerodynamics*, 122, 38-49.

[6] Ewins, D. J. (2000). *Modal Testing: Theory, Practice and Application.* Research Studies Press, 2. edition.

[7] Fergestad, D., Høyte, J., and Brathaug, H.-P. (1996) *Brukermanual til ALVSAT versjon 3.7: Analyse av lineære svingninger av hengebru i vinduro.* SINTEF Bygg og miljøteknikk, Konstruksjonsteknikk.

[8] Gazzloa, F. (2015). *Mathematical Models for Suspension Bridges: Nonlinear Structural Instability.* Springer, 1. edition.

[9] Ghavami, P. (2014). *Mechanics of Materials: An Introduction to Engineering Technology.* Springer, 1. edition.

[10] Gimsing, N. J. and Georgakis C. T. (2012). *Cable Supported Bridges: Concept and Design.* John Wiley & Sons Ltd., 3. edition.

[11] Kitagawa, M. (2004). Technology of the Akashi Kaikyo Bridge. *Structural Control and Health Monitoring*, 11, 75-90.

[12] Lin, S. and Huang, Z. (2016). *Comparative Design of Structures.* Springer, 1. edition.

[13] NPRA. (2015). *Bruprosjektering: Håndbok N400.* www.vegvesen.no.

[14] NPRA. (2012). *Ferjefri E39: Delprosjekt Fjordkryssing.* www.vegvesen.no.

[15] NPRA. (2012). *Hardanger Bridge: Technical Brochure.* www.vegvesen.no.

[16] NPRA, Berntsen, K. Private communication.

[17] Otto, A. (2011). *Methods of Numerical Simulation in Fluids and Plasmas.* University of Alaska Fairbanks.

[18] Papadrakakis, M., Stefanou, G. and Papadopoulos, V. (2011). *Computational Methods in Stochastic Dynamics.*

[19] Rainieri, C. and Fabbrocino, G. (2014). *Operational Modal Analysis of Civil Engineering Structures.* Springer, 1. edition

[20] Rupakhety, R. and Sigbjörnsson, R. (2012). *Computational Mechanics 1: Lecture*

Notes. Universioty of Iceland.

[21] Strømmen, E. N. (2014). *Structural Dynamics*. Springer, 1. edition.

[22] Strømmen, E. N. (2010). *Theory of Bridge Aerodynamics*. Springer, 2. edition.

[23] Tamura, Y. and Kareem, A. (2013). Advanced Structural Wind Engineering. Springer, 1. edition.

[24] TSI Incorporated. (2012). *Turbulence Intensity Measurements*.

[25] Wang Q., Liao, H., Li, M. and Ma, C. (2011). Influence of aerodynamic configuration of a streamline box girder on bridge flutter and vortex-induced vibration. *Journal of Modern Transportation*, 19(4), 261-267.

[26] Yang, Y., Ge, Y. and Zhang, W. (2009). Flutter Performance and Surrounding Flow Structures of Central-Slotted Box Girders. *Computational Structural Engineering*, Shanghai, 577-586.

Appendix

A ALVSAT

This appendix includes all relevant data for the calculations performed in ALVSAT, both the input data for the calculations of the eigenvalue problem as well as the resulting output data.

A.1 Input

A summary of the parameters used for the input file to define the bridge model is provided in Table 4 below. Most of these parameters have been previously defined or calculated in Section 5.

Table 4: Input parameters used in Alvsat

Parameter	Value	Description
DG	$2,5$	*Height of bridge deck* [m]
DC	$0,691$	*Diameter of main cable* [m]
BG	11	*Breadth of bridge deck* [m]
L	2050	*Length of bridge main span* [m]
HM	3,02	*Shortest hanger length* [m]
F	205	*Sag of main cable* [m]
NY	26,283	*Hogging of bridge deck* [m]
MG	13250	*Mass of both bridge decks pr. meter* [kg/m]
MC	3200	*Mass of each main cable pr. meter* [kg/m]
H	$2,48 \times 10^8$	*Tension in each of the main cables, bridge span centre* [N]
EIZ	$1,873 \times 10^{13}$	*Bending stiffness of bridge deck about vertical axis, lateral displacement* [Nm^2]
G	$9,80665$	*Gravitational acceleration* [m/s^2]
S0	0	*Tension in bridge deck* [N]
PI1/PI2	0,231	*Length of backstay nr.* 1/2*, as a proportion of* L [-]
FI1/FI2	0,523	*Incline of backstay* 1/2 [rad]
HR	0,84	*Vertical distance between hanger fastening level and centre of gravity of bridge deck* [m]
BC	15	*Half the distance* (c/c) *between main cables* [m]
M	2 760 000	*Rotational inertia of the deck and main cables* [kgm^2/m]
AC	0,375	*Cross sectional area of each of the main cables* [m^2]
EIX	$1,766 \times 10^{11}$	*Bending stiffness of bridge deck about horizontal axis, vertical displacement* [Nm^2]
EIW	$3,424 \times 10^{11}$	*Warping torsion stiffness for bridge deck* [Nm^4]
GIT	$1,664 \times 10^{11}$	*Torsional stiffness for bridge deck* [Nm^2]
EC	$2,0 \times 10^{11}$	*Modulus of elasticity for main cables* [N/m^2]

The input file in its entirety is as follows:

```
TEXT
Bru over Halsafjorden. Testkjøring rev. 22.02.2016
Dempning: Korr. buffeting-teori og 0,5 % strukturell dempning
Lastfaktor på vind er 1.0 (r.p. 50 år)
MODE
1 1 1
0 0 0
0 0 0
STRU
2.5 0.691 22
2050 3.02 205 26.283
13250 3200 2.48E8 1.873e13
0 0 0
.231 .231 .523 .523
0.84 15
2760000 .375
1.766E11 3.424E11 1.664E11 0.200E12
FREQ
8 8 8
6 6 6
0 0 0 0
30 50 1
ENVI
2 2
29.16 62 0.0232
1 1 .9 1.25
COEF
0.826
0
1.0
-0.251 9.7 2 1
2.401 9.7 2 1
0.002 9.7 2 1
0.770 9.7 2 1
STAT
10 10 10
DYNA
1 1 1
0 0 0
600
0.005 -0.0074 0.0141
0.005 -0.0077 0.0096
0.005 -0.0062 0.0074
0.005 -0.0059 0.0065
0.005 -0.0043 0.0061
0.005  0.0031 0.0059
200
200
200
200
200
200
200
END
```

A.2 Output

```
0000000000000000000000000000000000000000000000000000000000000000000000000000000000000000000000000000
 0.0                                                                                                  0.0
 0.0 Bru over Halsafjorden. Testkjøring rev. 22.02.2016                                               0.0
 0.0 Dempning: Korr. buffeting-teori og 0,5 % strukturell dempning                                    0.0
 0.0 Lastfaktor på vind er 1.0 (r.p. 50 år)                                                           0.0
 0.0                                                                                                  0.0
 0000000000000000000000000000000000000000000000000000000000000000000000000000000000000000000000000000
 0.0.....................................................................................................0.0
 0.0.....................................................................................................0.0
 0.0.............................. Analysed by ...........................................................0.0
 0.0.....................................................................................................0.0
 0.0.....................................................................................................0.0
 0.0.....................................................................................................0.0
 0.0.....000.....0000.......000.....000...0000000.......000.....000000000000.0.0
 0.0....0    0....0   0........0  0.....0  0..0        0.....0    0....0          0.0.0
 0.0...0      0...0   0........0  0.....0  0.0          0...0      0...0          0.0.0
 0.0..0        0..0   0........0  0.....0  0.0          0..0        0..0          0.0.0
 0.0.0     0     0.0   0........0  0.....0  0.0    000   0.0     0     0.00000 00000.0.0
 0.0.0    0.0    0.0   0........0  0.....0  0.0   0...0000.0    0.0    0.....0 0.....0.0
 0.0.0   0...0   0.0   0........0  0.....0  0.0   0........0   0...0   0.....0 0.....0.0
 0.0.0   0...0   0.0   0........0  0.....0  0.0    0.......0   0...0   0.....0 0.....0.0
 0.0.0   0...0   0.0   0........0   0...0   0.0     0......0   0...0   0.....0 0.....0.0
 0.0.0   0...0   0.0   0........0   0...0   0..0      0.....0   0...0   0.....0 0.....0.0
 0.0.0   0...0   0.0   0........0   0...0   0...0      0....0   0...0   0.....0 0.....0.0
 0.0.0   0...0   0.0   0.........0   0.0   0.....0      0...0   0...0   0.....0 0.....0.0
 0.0.0   0...0   0.0   0.........0   0.0   0......0     0..0   0...0   0.....0 0.....0.0
 0.0.0   00000   0.0   0.........0   0.0   0.......0    0.0   00000   0.....0 0.....0.0
 0.0.0         0.0   0..........0   0   0.........0    0.0           0.....0 0.....0.0
 0.0.0         0.0   0..........0   0   0..........0   0.0           0.....0 0.....0.0
 0.0.0         0.0   0..........0       0..........0   0.0           0.....0 0.....0.0
 0.0.0   00000 0.0   0...........0     0...........0   0.0   00000   0.....0 0.....0.0
 0.0.0   0...0 0.0   0...........0     0....0000...0   0.0   0...0   0.....0 0.....0.0
 0.0.0   0...0 0.0   00000000....0     0....0    000   0.0   0...0   0.....0 0.....0.0
 0.0.0   0...0 0.0           0.....0  0.....0         0.0   0...0   0.....0 0.....0.0
 0.0.0   0...0 0.0           0.....0  0.....0         0.0   0...0   0.....0 0.....0.0
 0.0.0   0...0 0.0           0.....000......0        0..0   0...0   0.....0 0.....0.0
 0.0.0000...0000.00000000000.....0.......0000000...0000...0000.....000.....0.0
 0.0.....................................................................................................0.0
 0.0.....................................................................................................0.0
 0.0.....................                                    ......................0.0
 0.0..................... Version 3.7 / 940628 /             ......................0.0
 0.0.....................                                    ......................0.0
 0.0.....................................................................................................0.0
 0.0.....................................................................................................0.0
0.0...000000000000000000000000000000000000000000000000000000000000000000000000000000000000000000...0.0
0.0...0                                                                                          0...0.0
0.0...0  Developed by:   SINTEF div. of Structural Engineering                                   0...0.0
0.0...0                  N-7034 TRONDHEIM  NTH                                                   0...0.0
0.0...0                                                                                          0...0.0
0.0...0                  Excecuted 16-05-01 at 13:10:13                                          0...0.0
0.0...0                                                                                          0...0.0
0.0...000000000000000000000000000000000000000000000000000000000000000000000000000000000000000000...0.0
 0.0.....................................................................................................0.0
0.0000000000000000000000000000000000000000000000000000000000000000000000000000000000000000000000000.0
 0.....................................................................................................0.0
000000000000000000000000000000000000000000000000000000000000000000000000000000000000000000000000000000
1RUN MODES

                                HOR    VER    TOR
          FRECUENCY ANALYSES:   1      1      1
          STATIC    ANALYSES:   0      0      0
          DYNAMIC   ANALYSES:   0      0      0
      STRUCTURAL PARAMETERS :

          LENGTH OF BRIDGE SPAN                 L    =  2050.
          MINIMUM HANGER LENGTH                 HM   =  3.020
          SAG OF MAIN CABLES                    F    =  205.0
          HOGGING OF THE GIRDER                 NY   =  26.28
          LENGTH OF SIDE SPAN SECOND. CABLE     L1   =  .0000
          SAG OF SECONDARY CABLES               FS   =  .0000
          MASS    OF GIRDER                     MG   =  .1325E+05
          MASS    OF MAIN CABLES (ONE CABLE)    MC   =  3200.
          TENSION IN MAIN CABLE (ONE CABLE)     H    =  .2480E+09
          RIGIDITY OF GIRDER                    EI   =  .1873E+14
          ACCELERATION OF GRAVITY               G    =  9.807
          TYPICAL DIMENSION OF GIRDER           DG   =  2.500
          TYPICAL DIMENSION OF ONE CABEL        DC   =  .6910
          TYPICAL WIDTH OF THE GIRDER           BG   =  22.00
```

```
TENSION IN GIRDER                        S0   =  .0000
TENSION IN SECOND. CABLES                F0   =  .0000
INITIAL STRAIN IN SECOND. CABLES         STR  =  .0000
LENGTH OF BACKSTAYS IN % OF              PI1  =  .2310
THE LENGTH OF THE BRIDGE SPAN            PI2  =  .2310
CABLE SLOPE OF BACKSTAY 1:               FI1  =  .5230
CABLE SLOPE OF BACKSTAY 2:               FI2  =  .5230
DISTANCE BETWEEN POINT OF ATTACHMENT
FOR HANGERS AND THE CENTER OF
GYRATION                                 HR   =  .8400
HALF THE DISTANCE BETWEEN
THE CABLES                               BC   =   15.0000
MASS MOMENT OF INERTIA                   M    =  .2760E+07
HORIZONTAL COMPONENT OF
CROSS SECTION OF EACH CABLE              AC   =  .3750
BENDING STIFFNESS OF GIRDER              EIX  =  .1766E+12
WARPING RESISTANCE                       EIW  =  .3424E+12
TORSIONAL STIFFNESS                      GIT  =  .1664E+12
MODULUS OF ELASTICITY OF CABLE           EC   =  .2000E+12

1DATA FOR FREQUENCY ANALYSES

                                         HOR  VER  TOR
NUMBER OF COEFFICIENTS (NFC):             8    8    8
NUMBER OF NORMAL MODES (NNM):             6    6    6


FREQUENCY RANGE FOR ITERATION SEARCH :

LOWER LIMIT FOR VERTICAL MODE     VOMI =  .0000
UPPER LIMIT FOR VERTICAL MODE     VOMA =  .0000
LOWER LIMIT FOR TORSIONAL MODE    TOMI =  .0000
UPPER LIMIT FOR TORSIONAL MODE    TOMA =  .0000
MAXIMUM NUMBER OF ITERATIONS      NMAX =   30
NO. OF INTERVALS IN
FREQUENCY RANGE IN ASYM           ITFR =   50
BRIDGE HELD/FREE AT THE ENDS      LC   =    1
LC=0 : FREE  LC=1 : HELD AT ONE END

ENVIRONMENTAL DATA

ESDU  SPECTRUM (ISTYP=2)
----------------------

WIND SPEED AT THE LEVEL OF THE BRIDGE (UREF) =   38.60
INTEGRAL LENGTH SCALE OF U IN X-DIR (XLU)    =   448.2
TURBULENCE INTENSITY U COMPONENT             =   .1370
CHARACTERISTIC HEIGHT ABOVE THE
GROUND OF THE BRIDGE DECK                    =   62.00
WIND VELOCITY 10 M ABOVE THE GROUND          =   29.16
TURBULENCE INTENSITY OF VERTICAL VELOCITY    =   .7551E-01
INTEGRAL LENGTH SCALE OF U IN Y-DIR          =   127.4
INTEGRAL LENGTH SCALE OF U IN Z-DIR          =   81.11
INTEGRAL LENGTH SCALE OF W IN X-DIR          =   37.56
INTEGRAL LENGTH SCALE OF W IN Y-DIR          =   21.35
INTEGRAL LENGTH SCALE OF W IN Z-DIR          =   27.18
ALFA VALUE IN MODIFIED VON KARMAN SPECTRUM   =   .5884
BETA1 IN MODIFIED VON KARMAN SPECTRUM        =   .6259
BETA2 IN MODIFIED VON KARMAN SPECTRUM        =   .3741
TERRAIN ROUGHNESS (Z0)                       =   .2320E-01

ESDU   COHERENCE FUNCTION (ICTYP=2)
----------------------------------

DECAY FACTOR HORIZONTAL SEPARATION (U,W)=    1.000        1.000
DECAY FACTOR VERTICAL SEPARATION  (U,W) =    1.000        1.000
AVERAGE CORRELATION BETWEEN LOADS
ON GIRDER AND CABLES                    =    .9000
DENSITY OF AIR:                         =    1.250

COEFFICIENTS (FORM FACTORS)

CDG(1:5) :    .8260       .0000       .0000       .0000       .8260
CDDG(1:5):    .0000       .0000       .0000       .0000       .0000
CDC(1:5) :   1.000        .0000       .0000       .0000      1.000
CLG(1:5) :  -.2510       9.700       2.000       1.000      -.2510
CLDG(1:5):   2.401        9.700       2.000       1.000       2.401
CMG(1:5) :   .2000E-02    9.700       2.000       1.000       .2000E-02
CMDG(1:5):   .7700        9.700       2.000       1.000       .7700
```

1DATA FOR STATIC ANALYSIS

NUMBER OF INTERVAL FOR RESPONS CALCULATION

HOR	VER	TOR
10	10	10

DATA FOR DYNAMIC ANALYSES

	HOR	VER	TOR
CROSS TERMS BETWEEN MODES:	1	1	1
IRS :	0	0	0

DURATION OF STORM : 600.

CRITICAL DAMPING RATIOS :

CRDR(1,1:3) : .5000E−02 −.7400E−02 .1410E−01
CRDR(2,1:3) : .5000E−02 −.7700E−02 .9600E−02
CRDR(3,1:3) : .5000E−02 −.6200E−02 .7400E−02
CRDR(4,1:3) : .5000E−02 −.5900E−02 .6500E−02
CRDR(5,1:3) : .5000E−02 −.4300E−02 .6100E−02
CRDR(6,1:3) : .5000E−02 .3100E−02 .5900E−02

1 ********** HORIZONTAL RESPONSE **********

***** OUTPUT FROM THE FREQUENCY ANALYSIS *****

EVALUATION OF SYMMETRIC MODES:

MODE NO:	PERIOD SEC	FREQUENCY RAD/SEC
1	25.58721	.24556
2	7.43792	.84475
3	5.34431	1.17568

FOURIER CONSTANTS :

MODE	1		2		3	
	GIRDER	CABLES	GIRDER	CABLES	GIRDER	CABLES
	.1000E+01	.8929E+00	.1860E+00	−.5136E+00	−.3285E+00	.7781E+00
	.3806E−01	−.2748E−01	.1000E+01	.1838E+00	.1646E+00	.1000E+01
	−.2195E−02	.4504E−02	.1680E−01	−.3746E−01	.1218E−01	−.2759E−01
	.3687E−03	−.1539E−02	−.2146E−02	.9640E−02	−.1727E−02	.8119E−02
	−.8025E−04	.5860E−03	.5225E−03	−.3900E−02	.3516E−03	−.2721E−02
	.2461E−04	−.2586E−03	−.1481E−03	.1621E−02	−.1105E−03	.1242E−02
	−.8389E−05	.1257E−03	.5323E−04	−.8139E−03	.3602E−04	−.5613E−03
	.3309E−05	−.6604E−04	−.1988E−04	.4023E−03	−.1464E−04	.3010E−03

MODES OF VIBRATION

	1		2		3	
OBSERVATION POINT	GIRDER	CABLES	GIRDER	CABLES	GIRDER	CABLES
.00	.000E+00	.000E+00	.000E+00	.000E+00	.000E+00	.000E+00
102.50	.172E+00	.129E+00	.493E+00	−.175E−01	.307E−01	.562E+00
205.00	.338E+00	.257E+00	.882E+00	−.412E−01	.426E−01	.103E+01
307.50	.490E+00	.381E+00	.108E+01	−.772E−01	.221E−01	.132E+01
410.00	.624E+00	.500E+00	.106E+01	−.134E+00	−.351E−01	.140E+01

```
          512.50        .735E+00    .610E+00   .829E+00   -.215E+00  -.123E+00    .127E+01
          615.00        .823E+00    .709E+00   .443E+00   -.322E+00  -.227E+00    .966E+00
          717.50        .887E+00    .795E+00  -.478E-02   -.450E+00  -.329E+00    .564E+00
          820.00        .929E+00    .864E+00  -.413E+00   -.585E+00  -.411E+00    .161E+00
          922.50        .952E+00    .910E+00  -.694E+00   -.702E+00  -.462E+00   -.145E+00
         1025.00        .959E+00    .927E+00  -.794E+00   -.751E+00  -.479E+00   -.262E+00
1          ****************************************
          ********** HORIZONTAL RESPONSE *************
          ****************************************

          ***** OUTPUT FROM THE FREQUENCY ANALYSIS *****


          EVALUATION OF ASYMMETRIC MODES:/
           MODE          PERIOD        FREQUENCY
           NO:             SEC          RAD/SEC


              1        12.89222          .48736
              2         5.66201         1.10971
              3         4.24020         1.48181


          FOURIER CONSTANTS :

 MODE              1                          2                          3

           GIRDER        CABLES       GIRDER        CABLES       GIRDER        CABLES

          .1000E+01    .4770E+00   -.2202E+00    .1000E+01   -.7206E-01    .2104E+00
          .3868E-01   -.5244E-01   -.1603E+00    .1503E+00    .1000E+01    .5777E+00
         -.3711E-02    .1201E-01    .6712E-02   -.2317E-01    .1614E-01   -.6064E-01
          .7740E-03   -.4418E-02   -.1317E-02    .8009E-02   -.2606E-02    .1698E-01
         -.2017E-03    .1802E-02    .3311E-03   -.3092E-02    .6833E-03   -.6678E-02
          .6652E-04   -.8572E-03   -.1100E-03    .1463E-02   -.2151E-03    .2956E-02
         -.2393E-04    .4183E-03    .3898E-04   -.6987E-03    .7903E-04   -.1454E-02
         -.4415E-05   -.2244E-03   -.1617E-04    .3762E-03   -.3155E-04    .7487E-03


          MODES OF VIBRATION

                                    1                          2                          3
     OBSERVATION          GIRDER      CABLES       GIRDER      CABLES       GIRDER      CABLES
     POINT
             .00        .000E+00    .000E+00    .000E+00    .000E+00    .000E+00    .000E+00
          102.50        .329E+00    .123E+00   -.158E+00    .384E+00    .577E+00    .367E+00
          205.00        .621E+00    .240E+00   -.276E+00    .713E+00    .923E+00    .624E+00
          307.50        .844E+00    .341E+00   -.328E+00    .942E+00    .899E+00    .696E+00
          410.00        .975E+00    .419E+00   -.306E+00    .105E+01    .512E+00    .561E+00
          512.50        .100E+01    .466E+00   -.227E+00    .102E+01   -.876E-01    .266E+00
          615.00        .931E+00    .474E+00   -.120E+00    .882E+00   -.668E+00   -.909E-01
          717.50        .772E+00    .435E+00   -.248E-01    .667E+00   -.101E+01   -.381E+00
          820.00        .547E+00    .343E+00    .301E-01    .420E+00   -.977E+00   -.490E+00
          922.50        .282E+00    .195E+00    .333E-01    .189E+00   -.594E+00   -.351E+00
         1025.00       -.168E-06   -.119E-06   -.234E-07   -.108E-06    .373E-06    .226E-06
1          ****************************************
          ********** VERTICAL    RESPONSE *************
          ****************************************

          ***** OUTPUT FROM THE FREQUENCY ANALYSIS *****



          **********  SYMMETRIC  MODES  **********


           MODE          PERIOD        FREQUENCY
           NO:             SEC          RAD/SEC

              1        9.57608           .65613

              2        7.07971           .88749

              3        4.95216          1.26878


          FOURIER CONSTANTS :

 MODE       1             2             3
```

```
          .1000E+01     .9454E+00     .1212E+00

         -.9577E+00     .1000E+01     .5951E-01

         -.6460E-01    -.1749E+00     .1000E+01

         -.1945E-01    -.4168E-01    -.1758E-01

         -.8416E-02    -.1685E-01    -.5627E-02

         -.4333E-02    -.8438E-02    -.2595E-02

         -.2491E-02    -.4780E-02    -.1412E-02

         -.1543E-02    -.2934E-02    -.8467E-03


  MODES OF VIBRATION :          1          2          3

     OBSERVATION
     POINT :
           .00              .0000E+00  .0000E+00  .0000E+00
        102.50             -.3573E+00  .4097E+00  .7274E+00
        205.00             -.5438E+00  .8967E+00  .1072E+01
        307.50             -.5239E+00  .1321E+01  .8306E+00
        410.00             -.3045E+00  .1547E+01  .1450E+00
        512.50              .8319E-01  .1516E+01 -.5711E+00
        615.00              .5676E+00  .1228E+01 -.8919E+00
        717.50              .1072E+01  .7773E+00 -.6229E+00
        820.00              .1508E+01  .2976E+00  .7366E-01
        922.50              .1802E+01 -.6590E-01  .7805E+00
       1025.00              .1908E+01 -.1981E+00  .1076E+01
1          **********  ASYMMETRIC MODES  **********/

            MODE        PERIOD       FREQUENCY
            NO:           SEC         RAD/SEC

               1       11.70565         .53677

               2        6.28596         .99956

               3        4.15777        1.51119


          FOURIER CONSTANTS :

  MODE       1             2             3

         .1000E+01     .6803E-02     .1282E-02

        -.6804E-02     .1000E+01     .6262E-03

        -.1278E-02    -.6349E-03     .1000E+01

        -.4246E-03    -.1695E-03     .0000E+00

        -.1818E-03    -.6737E-04     .0000E+00

        -.8992E-04     .0000E+00     .0000E+00

        -.4891E-04     .0000E+00     .0000E+00

        -.2847E-04     .0000E+00     .0000E+00


  MODES OF VIBRATION :          1          2          3

     OBSERVATION
     POINT :
           .00             .0000E+00  .0000E+00  .0000E+00
        102.50             .3019E+00  .5878E+00  .8090E+00
        205.00             .5817E+00  .9511E+00  .9511E+00
        307.50             .8080E+00  .9511E+00  .3090E+00
        410.00             .9549E+00  .5878E+00 -.5878E+00
        512.50             .1006E+01 -.1852E-06 -.1000E+01
        615.00             .9549E+00 -.5878E+00 -.5878E+00
        717.50             .8080E+00 -.9511E+00  .3090E+00
        820.00             .5817E+00 -.9511E+00  .9511E+00
```

```
          922.50              .3019E+00  -.5878E+00   .8090E+00
         1025.00             -.1790E-06   .3704E-06  -.5556E-06


           ONE START FREQUENCY TRIED IN ASYM
           NUMBER OF ITERATIONS NECESSARY:       4
1          ******************************************
          ********** TORSIONAL  RESPONSE *************
          ******************************************


          ***** OUTPUT FROM THE FREQUENCY ANALYSIS *****


           **********  SYMMETRIC  MODES  **********

            MODE        PERIOD       FREQUENCY
            NO:           SEC         RAD/SEC

               1        6.07282        1.03464

               2        4.09734        1.53348

               3        2.54982        2.46416


          FOURIER CONSTANTS :

 MODE       1             2             3

         .1000E+01     .2418E+00     .3725E-01

        -.2428E+00     .1000E+01     .1855E-01

        -.3281E-01    -.2760E-01     .1000E+01

        -.1081E-01    -.7656E-02    -.5389E-02

        -.4891E-02    -.3280E-02    -.1787E-02

        -.2628E-02    -.1718E-02    -.8508E-03

        -.1575E-02    -.1016E-02    -.4799E-03

        -.1018E-02    -.6510E-03    -.2992E-03


 MODES OF VIBRATION :          1          2          3

    OBSERVATION
    POINT :
           .00              .0000E+00  .0000E+00  .0000E+00
         102.50             .3825E-02  .4592E+00  .7133E+00
         205.00             .7262E-01  .8509E+00  .1023E+01
         307.50             .1989E+00  .1083E+01  .7454E+00
         410.00             .3670E+00  .1100E+01  .4475E-01
         512.50             .5628E+00  .9007E+00 -.6652E+00
         615.00             .7611E+00  .5283E+00 -.9667E+00
         717.50             .9441E+00  .7269E-01 -.6812E+00
         820.00             .1090E+01 -.3602E+00  .2252E-01
         922.50             .1185E+01 -.6690E+00  .7294E+00
        1025.00             .1218E+01 -.7801E+00  .1023E+01
1          **********  ASYMMETRIC MODES  **********/

            MODE        PERIOD       FREQUENCY
            NO:           SEC         RAD/SEC

               1        6.20975        1.01183

               2        3.19575        1.96610

               3        2.13348        2.94505


          FOURIER CONSTANTS :
```

```
MODE        1              2              3

         .1000E+01      .1857E-02      .3702E-03

        -.1857E-02      .1000E+01      .1851E-03

        -.3699E-03     -.1858E-03      .1000E+01

        -.1319E-03     -.5305E-04      .0000E+00

        -.6152E-04     -.2291E-04      .0000E+00

        -.3354E-04      .0000E+00      .0000E+00

        -.2026E-04      .0000E+00      .0000E+00

        -.1316E-04      .0000E+00      .0000E+00


MODES OF VIBRATION :          1           2           3

    OBSERVATION
    POINT :
          .00             .0000E+00   .0000E+00   .0000E+00
       102.50             .3071E+00   .5878E+00   .8090E+00
       205.00             .5861E+00   .9511E+00   .9511E+00
       307.50             .8087E+00   .9511E+00   .3090E+00
       410.00             .9521E+00   .5878E+00  -.5878E+00
       512.50             .1002E+01  -.1852E-06  -.1000E+01
       615.00             .9521E+00  -.5878E+00  -.5878E+00
       717.50             .8087E+00  -.9511E+00   .3090E+00
       820.00             .5861E+00  -.9511E+00   .9511E+00
       922.50             .3071E+00  -.5878E+00   .8090E+00
      1025.00            -.1834E-06   .3704E-06  -.5556E-06


      ONE START FREQUENCY TRIED IN ASYM
      NUMBER OF ITERATIONS NECESSARY:       4

      ***** CPU-TIME USED =     12.9600 *****
```

B MATLAB Codes

B.1 Calculation Codes

B.1.1 main.m

```
% This matlab code runs dynamic response analysis on Halsafjorden Bridge.
% Required functions:
% > ImportAlvsat.m, JAF.m
% Requires a result file obtained from Alvsat.

clear all
close all
clc

%% Input parameters

% Import from Alvsat:
txtfile = 'halsafjordfinal.res'; %Name of text file to import
nModesH = 6; nModesV = 6; nModesT = 6; %Number of modes to import
nPoints = 11; %Number of observation points along bridge (half span)
lineEV=[211,260,312,360,426,474]; %First lines containing eigenvalue data
lineEM=[237,286,344,393,458,507]; %First lines containing eigenmode data


% Bridge geometry:
L = 2050; %Length of bridge span [m]
Lexp = 2050; %Flow exposed length, assumed equal to length of span [m]
B = 22; %Width of one box [m]
D = 2.5; %Height of box section [m]
gap = 10; %opening between box girders [m]
zf = 50; %height of deck over sea level at x=L/2 [m]

% Bridge mass and damping parameters:
m_z = 13250+2*3200; %Modally equivalent and evenly distributed mass [kg/m]
m_theta = 1320000+2*3200*15^2; %Modally equivalent and evenly distributed mass [kgm^2/m]
zeta_z = 0.005; zeta_theta = 0.005; %Damping ratios

% Bridge load coefficients:
C_D = 1.246; C_L = -0.246; C_M = 0.098; %Load coefficients
dC_L = 4.473; dC_M = -1.54; %Load coefficient slopes

% Wind data:
rho = 1.25; %Density of air [kg/m^3]
Iu = 0.12; Iv = 0.107; Iw = 0.047; %Turbulence intensity
% V = [10 20 30 40 45 50 54 55 55.2 55.4 56 56.4];
```

```
V = [10 20 30 40 45 47 50 52 54 56 58 60];
% V = linspace(10,46,30);
Nv = length(V); %Number of wind increments

% Frequency response calculations:
xr = L/4; %Location of response calculation along span.
x = linspace(0,1,2*nPoints-1); %Normalized length
omegamin = 0.001; %Minimum frequency
omegamax = 10; %Maximum frequency
Nomega = 1000; %Number of frequency increments

%End of input parameters

%% Eigenfrequencies and mode shapes
% Imports eigenfrequencies and mode shapes from a specified
% Alvsat result file.
[omegaH,omegaV,omegaT,fiHs,fiHa,fiVs,fiVa,fiTs,fiTa]=...
    ImportAlvsat(txtfile,nModesH,nModesV,nModesT,lineEV,lineEM,nPoints);
[omega_z,rowz] = min(omegaV(:,3));
[omega_theta,rowv] = min(omegaT(:,3));
if rowz <= nModesV/2
    fiV = fiVs(:,rowz+1);
else
    fiV = fiVa(:,rowz+1-nModesV/2);
end
if rowv <= nModesT/2
    fiT = fiTs(:,rowv+1);
else
    fiT = fiTa(:,rowv+1-nModesV/2);
end
[rowfi] = find(fiVa==xr);
PHIr = [fiV(rowfi) 0; 0 fiT(rowfi)]; %Mode shape matrix

%% Wind data calculations
xfLu = 100*(zf/10)^0.3; xfLw = xfLu/12;
Au = 6.8/(2*pi); Aw = 9.4/(2*pi);
Cux = 9/(2*pi); Cwx = 6/(2*pi);

%% Frequency response

% Matrix creation:
% Mean wind velocity dependent eigenfrequency
omegaVz = zeros(1,Nv+1); omegaVz(1) = omega_z;
omegaVv = zeros(1,Nv+1); omegaVv(1) = omega_theta;
omegar = linspace(omegamin,omegamax,Nomega);
% Frequency response function / Impedence matrix
H11 = zeros(Nv,Nomega); H12 = H11; H21 = H11; H22 = H11;
```

```
detH = zeros(Nv,Nomega);
% Reduced wind velocity
VredVz = zeros(1,Nv);
VredVv = zeros(1,Nv);
% Unit vector
I = eye(2,2);
% Spectral Density response matrix
Srr11 = zeros(Nv,Nomega);
Srr12 = Srr11; Srr21 = Srr11; Srr22 = Srr11;
% Covariance matrix
sigmaz = zeros(1,Nv); sigmav = sigmaz;
COVzv = sigmaz; COVvz = sigmaz;
% Joint Acceptance Function
Iu11 = zeros(Nomega); Iu12 = Iu11; Iu22 = Iu11;
Iw11 = zeros(Nomega); Iw12 = Iw11; Iw22 = Iw11;
betau = zeros(Nomega); betaw = betau;
J11red = zeros(Nomega); J12red = J11red; J22red = J11red;
% Kaimal Spectral Density
Su = zeros(Nomega); Sw = zeros(Nv,Nomega);
% Aerodynamic Coefficients
k_aezv = zeros(1,Nv); k_aezz = k_aezv; k_aevz = k_aezv; k_aevv = k_aezv;
z_aezv = zeros(1,Nv); z_aezz = z_aezv; z_aevz = z_aezv; z_aevv = z_aezv;

% Mode shape integrals
fizz = L*trapz(x,fiV.^2);
fizv = L*trapz(x,fiV.*fiT);
fivz = fizv;
fivv = L*trapz(x,fiT.^2);

for i = 1:Nv
    VredVz(i) = V(i)/(B*omegaVz(i));
    VredVv(i) = V(i)/(B*omegaVv(i));

    H1v = VredVz(i)*(2*pi)*(1-(3.1871*pi^2/((7.5233e-3)^2*(VredVz(i)*(2*pi))^2+pi^2)...
        +2.8661*pi^2/(1.3663^2*(VredVz(i)*(2*pi))^2+pi^2)+...
        (-4.6341e-3)*pi^2/((1.4553-4)^2*(VredVz(i)*(2*pi))^2+pi^2)+...
        (-2.5164)*pi^2/((1.3555e-1)^2*(VredVz(i)*(2*pi))^2+pi^2)));
    H4v = pi*(VredVz(i)*(2*pi))^2*...
        (3.1871*((7.5233e-3)/((7.5233e-3)^2*(VredVz(i)*(2*pi))^2+pi^2))+...
        2.8661*(1.3663/(1.3663^2*(VredVz(i)*(2*pi))^2+pi^2))+...
        (-4.6341e-3)*((1.4553-4)/((1.4553-4)^2*(VredVz(i)*(2*pi))^2+pi^2))+...
        (-2.5164)*((1.3555e-1)/((1.3555e-1)^2*(VredVz(i)*(2*pi))^2+pi^2)));
    H2v = 0.5*(VredVz(i)*(2*pi))^3*...
        (-(9.9797e2)*(4.1659e-1)/((4.1659e-1)^2*(VredVz(i)*(2*pi))^2+pi^2)+...
        -(2.5178e1)*(3.2417e1)/((3.2417e1)^2*(VredVz(i)*(2*pi))^2+pi^2)+...
        -(-1e3)*(4.1794e-1)/((4.1794e-1)^2*(VredVz(i)*(2*pi))^2+pi^2)+0);
    H3v = (1/(2*pi))*(VredVz(i)*(2*pi))^2*(1-...
```

```
    ((9.9797e2)*pi^2/((4.1659e-1)^2*(VredVz(i)*(2*pi))^2+pi^2)+...
    (2.5178e1)*pi^2/((3.2417e1)^2*(VredVz(i)*(2*pi))^2+pi^2)+...
    (-1e3)*pi^2/((4.1794e-1)^2*(VredVz(i)*(2*pi))^2+pi^2)+0));
A1v = (1/4)*(VredVv(i)*(2*pi))*(1-...
    ((6.3134e1)*pi^2/((4.4634e-2)^2*(VredVv(i)*(2*pi))^2+pi^2)+...
    (-6.1917e1)*pi^2/((4.7993e-2)^2*(VredVv(i)*(2*pi))^2+pi^2)+0));
A4v = (pi/4)*(VredVv(i)*(2*pi))^2*...
    ((6.3134e1)*(4.4634e-2)/((4.4634e-2)^2*(VredVv(i)*(2*pi))^2+pi^2)+...
    (-6.1917e1)*(4.7993e-2)/((4.7993e-2)^2*(VredVv(i)*(2*pi))^2+pi^2)+0);
A2v = (1/8)*(VredVv(i)*(2*pi))^3*...
    (-(1.7282)*(8.2129e-2)/((8.2129e-2)^2*(VredVv(i)*(2*pi))^2+pi^2)+...
    -(-8.7918e-1)*(3.0692e-9)/((3.0692e-9)^2*(VredVv(i)*(2*pi))^2+pi^2)+...
    -(0)*(9.641e-2)/((9.641e-2)^2*(VredVv(i)*(2*pi))^2+pi^2)+0);
A3v = (1/(8*pi))*(VredVv(i)*(2*pi))^2*(1-...
    ((1.7282)*pi^2/((8.2129e-2)^2*(VredVv(i)*(2*pi))^2+pi^2)+...
    (-8.7918e-1)*pi^2/((3.0692e-9)^2*(VredVv(i)*(2*pi))^2+pi^2)+...
    (0)*pi^2/((9.641e-2)^2*(VredVv(i)*(2*pi))^2+pi^2)+0));

% Aerodynamic coefficients
k_aezz(i) = (rho*B^2/(2*m_z))*H4v;
k_aezv(i) = (rho*B^3/(2*m_z))*H3v*(fizv/fizz);
k_aevv(i) = (rho*B^4/(2*m_theta))*A3v;
k_aevz(i) = (rho*B^3/(2*m_theta))*A4v*(fivz/fivv);
K_ae = [k_aezz(i) k_aezv(i); k_aevz(i) k_aevv(i)];
z_aezz(i) = (rho*B^2/(4*m_z))*H1v;
z_aezv(i) = (rho*B^3/(4*m_z))*H2v*(fizv/fizz);
z_aevv(i) = (rho*B^4/(4*m_theta))*A2v;
z_aevz(i) = (rho*B^3/(4*m_theta))*A1v*(fivz/fivv);
Z_ae = [z_aezz(i) z_aezv(i); z_aevz(i) z_aevv(i)];

for k = 1:Nomega
    % Impedance matrix
    omega=omegar(k); omegaz=omega/omega_z; omegav=omega/omega_theta;
    Ek = I-K_ae-[omegaz^2 0; 0 omegav^2]+...
        2i*([omegaz 0; 0 omegav]*([zeta_z 0; 0 zeta_theta]-Z_ae));
    % FRF
    Hk = inv(Ek);
    H11(i,k) = Hk(1,1); H12(i,k) = Hk(1,2);
    H21(i,k) = Hk(2,1); H22(i,k) = Hk(2,2);
    detH(i,k) = abs(det(Hk));
end
[~,locz] = max(abs(H11(i,:)));
[~,locv] = max(abs(H22(i,:)));
omegaVznew = omegar(locz);
omegaVvnew = omegar(locv);
omegaVz(i+1) = omegaVznew;
omegaVv(i+1) = omegaVvnew;
```

```
    % Normalized auto spectral density:
    Su = (Au*xfLu/V(i))*ones(size(omegar))./((1+1.5*Au*xfLu*omegar/V(i)).^(5/3));
    Sw = (Aw*xfLw/V(i))*ones(size(omegar))./((1+1.5*Aw*xfLw*omegar/V(i)).^(5/3));

    % Joint Acceptance Function
    betau = Cux*Lexp*omegar/V(i);
    betaw = Cwx*Lexp*omegar/V(i);
    [Iu11] = JAF(x,fiV,fiV,betau);
    [Iu12] = JAF(x,fiV,fiT,betau);
    [Iu22] = JAF(x,fiT,fiT,betau);
    [Iw11] = JAF(x,fiV,fiV,betaw);
    [Iw12] = JAF(x,fiV,fiT,betaw);
    [Iw22] = JAF(x,fiT,fiT,betaw);

    J11 = L^2.*((2*C_L)^2*Iu^2*Su.*Iu11+(dC_L+(D/B)*C_D)^2*Iw^2*Sw.*Iw11);
    J12 = L^2.*(4*C_L*B*C_M*Iu^2*Su.*Iu12+(dC_L+(D/B)*C_D)*B*dC_M*Iw^2*Sw.*Iw12);
    J22 = L^2.*((2*B*C_M)^2*Iu^2*Su.*Iu22+(B*dC_M)^2*Iw^2*Sw.*Iw22);

    J11red = J11/(fizz^2);
    J12red = J12/(fizz*fivv);
    J22red = J22/(fivv^2);

    % Normalized modal load matrix
    for j = 1:Nomega
        SRR11 = (rho*B^3/(2*m_z))*(rho*B^3/(2*m_z))...
            *(V(i)/(B*omega_z))^2*(V(i)/(B*omega_z))^2*J11red(j);
        SRR12 = (rho*B^3/(2*m_z))*(rho*B^3/(2*m_theta))...
            *(V(i)/(B*omega_z))^2*(V(i)/(B*omega_theta))^2*J12red(j);
        SRR21 = SRR12;
        SRR22 = (rho*B^3/(2*m_theta))*(rho*B^3/(2*m_theta))...
            *(V(i)/(B*omega_theta))^2*(V(i)/(B*omega_theta))^2*J22red(j);
        H = [H11(i,j) H12(i,j); H21(i,j) H22(i,j)];
        SRR = [SRR11 SRR12; SRR21 SRR22];
        Seta = conj(H)*SRR*H';
        Srr = PHIr*Seta*PHIr';
        Srr11(i,j) = Srr(1,1); Srr12(i,j) = Srr(1,2);
        Srr21(i,j) = Srr(2,1); Srr22(i,j) = Srr(2,2);
    end

    COVrrVi = [trapz(omegar,abs(Srr11(i,:))) trapz(omegar,abs(Srr12(i,:)));...
        trapz(omegar,abs(Srr21(i,:))) trapz(omegar,abs(Srr22(i,:)))];

    sigmaz(1,i) = sqrt(COVrrVi(1,1)); COVzv(1,i) = COVrrVi(1,2);
    COVvz(1,i) = COVrrVi(2,1); sigmav(1,i) = sqrt(COVrrVi(2,2));
end
```

```
clear ADplot c0 c1 c2 i j J11 J12 J22 k locv locz...
    rowfi rowv rowz Seta COVrr Srr SRR SRR11 SRR12 SRR21 SRR22

save response.mat
```

B.1.2 ImportAlvsat.m

```
% This matlab code extracts eigenvalues and corresponding
% eigenmodes from an Alvsat response file.

function [omegaH,omegaV,omegaT,fiHs,fiHa,fiVs,fiVa,fiTs,fiTa] = ...
    ImportAlvsat(txtfile,nModesH,nModesV,nModesT,lineEV,lineEM,nPoints)

%% Output Structure Guide
%
% Eigenvalues exported into 3 matrices with the following structure:
%  symmetric  [mode no. period(sec) frequency(rad/s)]
%             [   ...         ...         ...       ]
%  asymmetric [mode no. period(sec) frequency(rad/s)]
%             [   ...         ...         ...       ]
%
% Eigenmodes given in a total of 6 separate matrices for symmetric and
% asymmetric modes for horizontal, vertical and torsional response,
% respecively.
% The structure for horizontal modes is as follows:
%              mode no.                  1                  2    ...
%       [Observation point Displ. (girder) Displ. (cable)   ...
%
% The structure for vertical/torsional modes is as follows:
%               mode no.         1         2    ...
%      [Observation point Displacement    ...
%
%% User Input Variables Guide
%
% txtfile - name of text file
% nModesH - number of horizontal modes
% nModesV - number of vertical modes
% nModesT - number of torsional modes
% lineEV - start of eigenvalue data lines
% ([xsym,xasym,zsym,zasym,tsym,tasym], set a column as 0 if not included)
% lineEM - start of eigenmode data lines
% ([xsym,xasym,zsym,zasym,tsym,tasym], set a column as 0 if not included)
% nPoints - number of observation points along bridge (half span)

%% Read text file

fid = fopen(txtfile);
S = textscan(fid,'%s','Delimiter','\n');
S = S{1};

%% Eigenvalues
```

```
nVar = 3; %no of variables
omegaH = zeros(nModesH,nVar); omegaV = zeros(nModesV,nVar);
omegaT = zeros(nModesT,nVar);
if nModesH ~= 0
    for j = 1:2;
        for i = 1:(nModesH/2)
            responseLine=S{i-1+lineEV(j)};
            responseData=sscanf(responseLine(1:end),'%f');
            omegaH(i+(nModesH/2)*(j-1),[1:nVar])=responseData;
        end
    end
end
if nModesV ~= 0
    for j = 1:2;
        for i = 1:(nModesV/2)
            responseLine=S{2*i-2+lineEV(j+2)};
            responseData=sscanf(responseLine(1:end),'%f');
            omegaV(i+(nModesV/2)*(j-1),[1:nVar])=responseData;
        end
    end
end
if nModesT ~= 0
    for j = 1:2;
        for i = 1:(nModesT/2)
            responseLine=S{2*i-2+lineEV(j+4)};
            responseData=sscanf(responseLine(1:end),'%f');
            omegaT(i+(nModesT/2)*(j-1),[1:nVar])=responseData;
        end
    end
end
% omega(~any(omega,2),:) = [];  %delete zeros rows

%% Eigenmodes

if nModesH ~=0
    nVarH = (nModesH/2)*2+1; %no of variables for horizontal modes
    fiH = zeros(nPoints*2*2,nVarH); %horizontal eigenmodes
    for j = 1:2;
        for i = 1:nPoints
            responseLine=S{i-1+lineEM(j)};
            responseData=sscanf(responseLine(1:end),'%f');
            fiH(i+2*nPoints*(j-1),[1:nVarH])=responseData;
        end
    end
    for j = 1:(nPoints-1)
        fiH(j+nPoints,1)=1025+102.5*j;
```

```
        fiH(j+3*nPoints,1)=1025+102.5*j;
        for k = 1:length(fiH(1,:))-1;
            fiH(j+nPoints,k+1)=fiH((nPoints-j),k+1);
            fiH(j+3*nPoints,k+1)=-fiH((3*nPoints-j),k+1);
        end
    end
    % Normalize eigenmodes
    for n=1:nVarH-1
        ms=max(abs(fiH(1:(2*nPoints-1),n+1)));
        fiH(1:(2*nPoints-1),n+1)=(1/ms).*fiH(1:(2*nPoints-1),n+1);
        ma=max(abs(fiH((2*nPoints+1):(4*nPoints-1),n+1)));
        fiH((2*nPoints+1):(4*nPoints-1),n+1)=(1/ma).*fiH((2*nPoints+1)...
            :(4*nPoints-1),n+1);
    end
    fiHs = fiH(1:2*nPoints-1,:); %symmetric modes
    fiHa = fiH(2*nPoints+1:4*nPoints-1,:); %aymmetric modes
else fiHs = []; fiHa = [];
end
if nModesV ~=0
    nVarV = (nModesV/2)+1; %no of variables for vertical modes
    fiV = zeros(nPoints*2*2,nVarV); %vertical eigenmodes
    for j = 1:2;
        for i = 1:nPoints
            responseLine=S{i-1+lineEM(j+2)};
            responseData=sscanf(responseLine(1:end),'%f');
            fiV(i+2*nPoints*(j-1),[1:nVarV])=responseData;
        end
    end
    for j = 1:(nPoints-1)
        fiV(j+nPoints,1)=1025+102.5*j;
        fiV(j+3*nPoints,1)=1025+102.5*j;
        for l = 1:length(fiV(1,:))-1;
            fiV(j+nPoints,l+1)=fiV((nPoints-j),l+1);
            fiV(j+3*nPoints,l+1)=-fiV((3*nPoints-j),l+1);
        end
    end
    % Normalize eigenmodes
    for n=1:nVarV-1
        ms=max(abs(fiV(1:(2*nPoints-1),n+1)));
        fiV(1:(2*nPoints-1),n+1)=(1/ms).*fiV(1:(2*nPoints-1),n+1);
        ma=max(abs(fiV((2*nPoints+1):(4*nPoints-1),n+1)));
        fiV((2*nPoints+1):(4*nPoints-1),n+1)=(1/ma).*fiV((2*nPoints+1)...
            :(4*nPoints-1),n+1);
    end
    fiVs = fiV(1:2*nPoints-1,:); %symmetric modes
    fiVa = fiV(2*nPoints+1:4*nPoints-1,:); %aymmetric modes
else fiVs = []; fiVa = [];
```

```
end
if nModesT ~= 0
    nVarT = (nModesT/2)+1; %no of variables for torsional modes
    fiT = zeros(nPoints*2*2,nVarT); %torsional eigenmodes
    for j = 1:2
        for i = 1:nPoints
            responseLine=S{i-1+lineEM(j+4)};
            responseData=sscanf(responseLine(1:end),'%f');
            fiT(i+2*nPoints*(j-1),[1:nVarT])=responseData;
        end
    end
    for j = 1:(nPoints-1)
        fiT(j+nPoints,1)=1025+102.5*j;
        fiT(j+3*nPoints,1)=1025+102.5*j;
        for l = 1:length(fiV(1,:))-1;
            fiT(j+nPoints,l+1)=fiT((nPoints-j),l+1);
            fiT(j+3*nPoints,l+1)=-fiT((3*nPoints-j),l+1);
        end
    end
    % Normalize eigenmodes
    for n=1:nVarT-1
        ms=max(abs(fiT(1:(2*nPoints-1),n+1)));
        fiT(1:(2*nPoints-1),n+1)=(1/ms).*fiT(1:(2*nPoints-1),n+1);
        ma=max(abs(fiT((2*nPoints+1):(4*nPoints-1),n+1)));
        fiT((2*nPoints+1):(4*nPoints-1),n+1)=(1/ma).*fiT((2*nPoints+1)...
            :(4*nPoints-1),n+1);
    end
    fiTs = fiT(1:2*nPoints-1,:); %symmetric modes
    fiTa = fiT(2*nPoints+1:4*nPoints-1,:); %aymmetric modes
else fiTs = []; fiTa = [];
end
```

B.1.3 ADs.m

```
% This script calculates the aerodynamic derivatives
% based on given indicial functions.
% ADs sorted in rows in the following format:
% [H1*; H2*; H3*; H4*; A1*; A2*; A3*; A4*]
% Requires 'response.mat' obtained by running 'main.m'.

clear all
close all

load response.mat
NvAD = 40; %Number of increments
H1 = zeros(1,NvAD); H2 = H1; H3 = H1; H4 = H1;
A1 = zeros(1,NvAD); A2 = A1; A3 = A1; A4 = A1;
Vred_min = 0/(B*omega_theta);
Vred_max = 180/(B*omega_z);
Vred = linspace(Vred_min,Vred_max,NvAD);

for i = 1:NvAD
    % ADs from new measurements
    H1(i) = Vred(i)*(2*pi)*(1-(3.1871*pi^2/((7.5233e-3)^2*(Vred(i)*(2*pi))^2+pi^2)...
        +2.8661*pi^2/(1.3663^2*(Vred(i)*(2*pi))^2+pi^2)+...
        (-4.6341e-3)*pi^2/((1.4553-4)^2*(Vred(i)*(2*pi))^2+pi^2)+...
        (-2.5164)*pi^2/((1.3555e-1)^2*(Vred(i)*(2*pi))^2+pi^2)));
    H4(i) = pi*(Vred(i)*(2*pi))^2*...
        (3.1871*((7.5233e-3)/((7.5233e-3)^2*(Vred(i)*(2*pi))^2+pi^2))+...
        2.8661*(1.3663/(1.3663^2*(Vred(i)*(2*pi))^2+pi^2))+...
        (-4.6341e-3)*((1.4553-4)/((1.4553-4)^2*(Vred(i)*(2*pi))^2+pi^2))+...
        (-2.5164)*((1.3555e-1)/((1.3555e-1)^2*(Vred(i)*(2*pi))^2+pi^2)));
    H2(i) = 0.5*(Vred(i)*(2*pi))^3*...
        (-(9.9797e2)*(4.1659e-1)/((4.1659e-1)^2*(Vred(i)*(2*pi))^2+pi^2)+...
        -(2.5178e1)*(3.2417e1)/((3.2417e1)^2*(Vred(i)*(2*pi))^2+pi^2)+...
        -(-1e3)*(4.1794e-1)/((4.1794e-1)^2*(Vred(i)*(2*pi))^2+pi^2)+0);
    H3(i) = (1/(2*pi))*(Vred(i)*(2*pi))^2*(1-...
        ((9.9797e2)*pi^2/((4.1659e-1)^2*(Vred(i)*(2*pi))^2+pi^2)+...
        (2.5178e1)*pi^2/((3.2417e1)^2*(Vred(i)*(2*pi))^2+pi^2)+...
        (-1e3)*pi^2/((4.1794e-1)^2*(Vred(i)*(2*pi))^2+pi^2)+0));
    A1(i) = (1/4)*(Vred(i)*(2*pi))*(1-...
        ((6.3134e1)*pi^2/((4.4634e-2)^2*(Vred(i)*(2*pi))^2+pi^2)+...
        (-6.1917e1)*pi^2/((4.7993e-2)^2*(Vred(i)*(2*pi))^2+pi^2)+0));
    A4(i) = (pi/4)*(Vred(i)*(2*pi))^2*...
        ((6.3134e1)*(4.4634e-2)/((4.4634e-2)^2*(Vred(i)*(2*pi))^2+pi^2)+...
        (-6.1917e1)*(4.7993e-2)/((4.7993e-2)^2*(Vred(i)*(2*pi))^2+pi^2)+0);
    A2(i) = (1/8)*(Vred(i)*(2*pi))^3*...
        (-(1.7282)*(8.2129e-2)/((8.2129e-2)^2*(Vred(i)*(2*pi))^2+pi^2)+...
```

```
        -(-8.7918e-1)*(3.0692e-9)/((3.0692e-9)^2*(Vred(i)*(2*pi))^2+pi^2)+...
        -(0)*(9.641e-2)/((9.641e-2)^2*(Vred(i)*(2*pi))^2+pi^2)+0);
    A3(i) = (1/(8*pi))*(Vred(i)*(2*pi))^2*(1-...
        ((1.7282)*pi^2/((8.2129e-2)^2*(Vred(i)*(2*pi))^2+pi^2)+...
        (-8.7918e-1)*pi^2/((3.0692e-9)^2*(Vred(i)*(2*pi))^2+pi^2)+...
        (0)*pi^2/((9.641e-2)^2*(Vred(i)*(2*pi))^2+pi^2)+0));
end
ADV = [H1;H2;H3;H4;A1;A2;A3;A4];

save ADs.mat
```

B.1.4 JAF.m

```
% This function calculates the joint acceptance function by
% numerical integration.
%
% Parameter definitions:
% x    - Normalized length along span
% f,g  - Mode shapes

function [I] = JAF(x,f,g,beta)

I = zeros(1,length(beta));
for i = 1:length(beta)
    for n = 1:length(x)
        for m = 1:length(x)
            dx = abs(x(n)-x(m));
            Co = exp(-beta(i)*dx);
            I(i) = I(i) + f(n)*g(m)*Co;
        end
    end
end
I = (1/length(x)^2).*I;
```

B.1.5 ADplate.m

```
% This function calculates the aerodynamic derivatives
% for an ideal flat plate.
%
% Parameter definitions:
% Vred    - Reduced wind velocity (non-dimensional)
% omegand - Non-dimensional eigenfrequency, mode i.
% Hn,An   - Aerodynamic derivatives for flat plate. n = 1,2,3,4.
% J0,J1   - Bessel functions of first kind, order 0 and 1 respectively.
% Y0,Y1   - Bessel functions of second kind, order 0 and 1 respectively.
% F       - Real part of Theodorsen's circulatory function
% G       - Imaginary part of Theodorsen's circulatory function
%
% INPUT:  Vred
% OUTPUT: Hn,An

function [H1,H2,H3,H4,A1,A2,A3,A4] = ADplate(Vred)

omegand = zeros(1,length(Vred));

F = zeros(1,length(Vred));
G = zeros(1,length(Vred));
H1 = zeros(1,length(Vred)); H2 = zeros(1,length(Vred));
H3 = zeros(1,length(Vred)); H4 = zeros(1,length(Vred));
A1 = zeros(1,length(Vred)); A2 = zeros(1,length(Vred));
A3 = zeros(1,length(Vred)); A4 = zeros(1,length(Vred));

for i = 1:length(Vred);
    omegand(i) = 1/Vred(i);

    J0 = besselj(0,omegand(i)/2);
    J1 = besselj(1,omegand(i)/2);
    Y0 = bessely(0,omegand(i)/2);
    Y1 = bessely(1,omegand(i)/2);

    F(i) = (J1*(J1+Y0)+Y1*(Y1-J0))/((J1+Y0)^2+(Y1-J0)^2);
    G(i) = -(J1*J0+Y1*Y0)/((J1+Y0)^2+(Y1-J0)^2);

    H1(i) = -2*pi*F(i)*Vred(i);
    H2(i) = 0.5*pi*(1+F(i)+4*G(i)*Vred(i))*Vred(i);
    H3(i) = 2*pi*(F(i)*Vred(i)-G(i)/4)*Vred(i);
    H4(i) = 0.5*pi*(1+4*G(i)*Vred(i));

    A1(i) = -0.5*pi*F(i)*Vred(i);
    A2(i) = -(pi/8)*(1-F(i)-4*G(i)*Vred(i))*Vred(i);
```

```
    A3(i) = 0.5*pi*(F(i)*Vred(i)-G(i)/4)*Vred(i);
    A4(i) = 0.5*pi*G(i)*Vred(i);
end
end
```

B.1.6 stability.m

```
% This script investigates four types of instabilities that bridge
% decks are susceptible to by inspection of the impedance matrix.
% Requires 'response.mat' obtained from running 'main.m'.

close all
clear all

load response.mat

%% Calculation switches (0 to disable, 1 to enable)
statdiv = 1; %Perform a static divergence instability check
gallop = 1; %Perform a galloping instability check
torsioninstab = 1; %Perform a torsional dynamic instability check
flutter = 1; %Performs a flutter instability check

%% Static divergence
if statdiv == 1
    if dC_M < 0
        disp('No static divergence instability')
    else
        Vcr_statdiv = B*omega_theta*sqrt(2*m_theta/(rho*B^4*dC_M));
    end
end

%% Galloping
if gallop == 1
    if dC_L < -C_D*D/B
        Vcr = -B*omega_z*zeta_z*4*m_z/((dC_L+C_D*D/B)*rho*B^2);
    else
        disp('No stability limit for galloping')
    end
end
%% Dynamic instability in torsion
if torsioninstab == 1
    if all(A2v<=0)== 1
        disp('No instability in pure torsion')
    else
        ReTorsroots = zeros(1,Nv);
        ImTorsion = zeros(1,Nv);
        for i = 1:Nv
            ReTorsion0 = 1-kaevv(i);
            ReTorsion1 = 0;
            ReTorsion2 = -1;
            ReTorsion = [ReTorsion2 ReTorsion1 ReTorsion0];
```

```
            ReTorsroots(i) = max(roots(ReTorsion));
            ImTorsion(i) = (zeta_theta - zaevv(i));
        end

        figure(); hold all;
        plot(VredVv,ReTorsroots,'b-o',VredVv,ImTorsion,'r-o')
        xlabel('V/(B*\omega_r)'); ylabel('Re,Im');
    end
end

%% Flutter

if flutter == 1

    zz = zeta_z; zv = zeta_theta;
    betaz = rho*B^2/m_z; betav = rho*B^4/m_theta;
    gamma = omega_theta/omega_z;
    Selberg = 0.6*B*omega_theta*((1-(omega_z/omega_theta)^2)*(m_z*m_theta)^0.5/(rho*B^3))^0.5;
    Vred = linspace(0.1,5,60);

    REr = zeros(1,length(Vred));
    IMr = zeros(1,length(Vred));
    for i = 1:length(Vred)

        H1 = Vred(i)*(2*pi)*(1-(3.1871*pi^2/((7.5233e-3)^2*(Vred(i)*(2*pi))^2+pi^2)...
            +2.8661*pi^2/(1.3663^2*(Vred(i)*(2*pi))^2+pi^2)+...
            (-4.6341e-3)*pi^2/((1.4553-4)^2*(Vred(i)*(2*pi))^2+pi^2)+...
            (-2.5164)*pi^2/((1.3555e-1)^2*(Vred(i)*(2*pi))^2+pi^2)));
        H4 = pi*(Vred(i)*(2*pi))^2*...
            (3.1871*((7.5233e-3)/((7.5233e-3)^2*(Vred(i)*(2*pi))^2+pi^2))+...
            2.8661*(1.3663/(1.3663^2*(Vred(i)*(2*pi))^2+pi^2))+...
            (-4.6341e-3)*((1.4553-4)/((1.4553-4)^2*(Vred(i)*(2*pi))^2+pi^2))+...
            (-2.5164)*((1.3555e-1)/((1.3555e-1)^2*(Vred(i)*(2*pi))^2+pi^2)));
        H2 = 0.5*(Vred(i)*(2*pi))^3*...
            (-(9.9797e2)*(4.1659e-1)/((4.1659e-1)^2*(Vred(i)*(2*pi))^2+pi^2)+...
            -(2.5178e1)*(3.2417e1)/((3.2417e1)^2*(Vred(i)*(2*pi))^2+pi^2)+...
            -(-1e3)*(4.1794e-1)/((4.1794e-1)^2*(Vred(i)*(2*pi))^2+pi^2)+0);
        H3 = (1/(2*pi))*(Vred(i)*(2*pi))^2*(1-...
            ((9.9797e2)*pi^2/((4.1659e-1)^2*(Vred(i)*(2*pi))^2+pi^2)+...
            (2.5178e1)*pi^2/((3.2417e1)^2*(Vred(i)*(2*pi))^2+pi^2)+...
            (-1e3)*pi^2/((4.1794e-1)^2*(Vred(i)*(2*pi))^2+pi^2)+0));
        A1 = (1/4)*(Vred(i)*(2*pi))*(1-...
            ((6.3134e1)*pi^2/((4.4634e-2)^2*(Vred(i)*(2*pi))^2+pi^2)+...
            (-6.1917e1)*pi^2/((4.7993e-2)^2*(Vred(i)*(2*pi))^2+pi^2)+0));
        A4 = (pi/4)*(Vred(i)*(2*pi))^2*...
            ((6.3134e1)*(4.4634e-2)/((4.4634e-2)^2*(Vred(i)*(2*pi))^2+pi^2)+...
            (-6.1917e1)*(4.7993e-2)/((4.7993e-2)^2*(Vred(i)*(2*pi))^2+pi^2)+0);
```

```
        A2 = (1/8)*(Vred(i)*(2*pi))^3*...
            (-(1.7282)*(8.2129e-2)/((8.2129e-2)^2*(Vred(i)*(2*pi))^2+pi^2)+...
            -(-8.7918e-1)*(3.0692e-9)/((3.0692e-9)^2*(Vred(i)*(2*pi))^2+pi^2)+...
            -(0)*(9.641e-2)/((9.641e-2)^2*(Vred(i)*(2*pi))^2+pi^2)+0);
        A3 = (1/(8*pi))*(Vred(i)*(2*pi))^2*(1-...
            ((1.7282)*pi^2/((8.2129e-2)^2*(Vred(i)*(2*pi))^2+pi^2)+...
            (-8.7918e-1)*pi^2/((3.0692e-9)^2*(Vred(i)*(2*pi))^2+pi^2)+...
            (0)*pi^2/((9.641e-2)^2*(Vred(i)*(2*pi))^2+pi^2)+0));

        RE0 = 1;
        RE1 = 0;
        RE2 = -(1+gamma^2+4*gamma*zz*zv+0.5*betaz*gamma^2*H4+...
            0.5*betav*A3);
        RE3 = gamma*(zv*betaz*gamma*H1+zz*betav*A2);
        RE4 = gamma^2*(1+0.5*betaz*H4+0.5*betav*A3+0.25*betaz*betav*...
            (A1*H2-A2*H1+A3*H4-A4*H3));
        RE = [RE4 RE3 RE2 RE1 RE0];
        REr(i) = abs(max(roots(RE))).*omega_theta;
        IM0 = 0;
        IM1 = 2*(zz*gamma+zv);
        IM2 = -0.5*(betaz*gamma^2*H1+betav*A2);
        IM3 = -2*(zz*(0.5*betav*A3+gamma)+zv*gamma^2*(0.5*betaz*H4+1));
        IM4 = 2*gamma^2*(0.125*betaz*betav*(H1*A3-H2*A4-...
            H3*A1+H4*A2)+0.25*(betaz*H1+betav*A2));
        IM = [IM4 IM3 IM2 IM1 IM0];
        IMr(i) = abs(max(roots(IM))).*omega_theta;
    end

    figure()
    plot(Vred,REr,'b-o',Vred,IMr,'r-o')
    xlabel('V_{red} (m/s)'); ylabel('Resonance frequency, \omega_r (rad/s)')
    legend('Real roots','Imaginary roots')
end
```

B.1.7 timesimulation.m

```
% This script performs a time domain simulation from the response
% spectral density. Requires 'response.mat' obtained from running 'main.m'.

clear all
close all
clc

load response.mat

Tmin = 0; %Minimum time value [s]
Tmax = 300; %Maximum time value [s]
Nt = 600; %Number of time increments

Vplot = [56.4]; %Wind velocities at which to perform simulation.
e = 0.01; %Error tolerance
domega = omegar(2) - omegar(1); %Frequency step
t = linspace(Tmin,Tmax,Nt);
for k = 1:length(Vplot)
    x1 = zeros(Nomega,length(t));
    x2 = zeros(Nomega,length(t));
    ind = find(abs(V - Vplot(k))<=e,1,'last');
    for i = 1:Nomega
        fi = 2*pi*rand;
        ck1 = sqrt(2.*domega.*Srr11(ind,i));
        ck2 = sqrt(2.*domega.*Srr22(ind,i));
        for j = 1:length(t)
            x1(i,j) = real(ck1.*exp(1i.*(omegar(i)*t(j)+fi)));
            x2(i,j) = real(ck2.*exp(1i.*(omegar(i)*t(j)+fi)));
        end
    end
    xt1 = sum(x1);
    xt2 = sum(x2);
    figure(); subplot(2,1,1); plot(t,xt1);
    ylabel('r_z (m)');
    text(0.1,0.9,['V = ' num2str(V(ind),3)...
        ' m/s, Resonance frequency \omega=' num2str(omegaVz(ind),3)...
        ' rad/s'],'Units','normalized')
    text(0.1,0.1,['Simulated: \sigma_{r_zr_z} = '...
        num2str(sigmaz(ind),3) ' m'],'Units','normalized')
    subplot(2,1,2); plot(t,xt2);
    xlabel('t (s)'); ylabel('r_\theta (rad)');
    text(0.1,0.9,['V = ' num2str(V(ind),3)...
        ' m/s, Resonance frequency \omega=' num2str(omegaVv(ind),3)...
        ' rad/s'],'Units','normalized')
```

```
    text(0.1,0.1,['Simulated: \sigma_{r_\thetar_\theta} = ' ...
        num2str(sigmav(ind),3) ' rad'],'Units','normalized')
end
```

B.2 Plot Codes

B.2.1 mainplot.m

```
% Main file
% This matlab code is the main file used to plot response quantities.
% Required functions:
% > modesh.m, plotADs.m, plotlog.m
% Requires 'response.mat' obtained from running 'main.m'.

clear all
close all
clc

load response.mat

%% Plot switches (0 to disable, 1 to enable)
% Use these switches to control which quantities to plot.

%Plot mode shapes
plotmodes = 0;

%Plot aerodynamic derivatives from experimental data
ADplot = 0;
plateADplot = 0; %Includes flat plate ADs for comparison,requires ADplot=1

%Wind velocities at which to plot response parameters:
Vplot = [20 40 56.4];
% (multiple values of Vplot are supported)
% (affects FRFplot, FRFcomponents, PSDplot switches below)

%Plot Kaimal Spectral Density:
KaimalSD = 0;
%Plot Joint Acceptance Function:
JAFplot = 0;
%Plot determinant of the Frequency Response Function:
FRFplot = 0;
%Plot all components of the Frequency Response Function:
FRFcomponents = 0;
%Plot Power Spectral Density:
PSDplot = 0;
%Plot aerodynamic damping and stiffness components:
damping_stiffness = 0;
%Response plot, plots sigma, covariance coefficient and omega:
COVplot = 0;
%Parameter study of the effects of changing ADs and damping ratio:
parameterstudy = 0;
```

```
%% Plots

if plotmodes == 1
    modesh(fiHs,fiHa,fiVs,fiVa,fiTs,fiTa,nModesH,nModesV,nModesT,...
        omegaH,omegaV,omegaT)
end

if ADplot == 1
    if plateADplot == 1
        [H1pl,H2pl,H3pl,H4pl,A1pl,A2pl,A3pl,A4pl] = ADplate(Vred);
        plotADs(Vred,Vred,ADV,H1pl,H2pl,H3pl,H4pl,A1pl,A2pl,A3pl,A4pl);
    else
        plotADs(Vred,Vred,ADV);
    end
end

if FRFplot == 1
    figure()
    plotlog(V,detH,omegar,Vplot);
    ylim([0.01 200]); xlim([0.1 3])
    xlabel('\omega (rad/s)')
    ylabel('|detH(\omega)|')
end

if FRFcomponents == 1
    figure()
    subplot(2,2,1)
    plotlog(V,abs(detH),omegar,Vplot);
    ylabel('|detH(\omega)|')
    ylim([0.01 200]); xlim([0.1 3])
    legend('Location','Southwest'); legend('boxoff')
    subplot(2,2,2)
    plotlog(V,abs(H11),omegar,Vplot);
    ylabel('|H_{11}(\omega)|')
    xlim([0.1 3]); legend off;
    subplot(2,2,3)
    plotlog(V,abs(H12),omegar,Vplot);
    xlabel('\omega (rad/s)')
    ylabel('|H_{12}(\omega)|')
    xlim([0.1 3]); legend off;
    subplot(2,2,4)
    plotlog(V,abs(H22),omegar,Vplot);
    xlabel('\omega (rad/s)')
    ylabel('|H_{22}(\omega)|')
    xlim([0.1 3]); legend off;
end
```

```
if KaimalSD == 1
    figure()
    semilogx(xfLu*omegar./V(end),omegar.*Su,...
        xfLw*omegar./V(end),omegar.*Sw)
    xlim([min(omegar) 2*max(omegar)])
    xlabel('Reduced frequency, \omega\cdot^{x_f}L_n/V')
    ylabel('Reduced auto spectral density, \omega\cdotS_n(\omega)/\sigma^2_n')
    legend('n = u','n = w')
end

if JAFplot == 1
    figure()
    loglog(betau,sqrt(Iu11),'-',betau,sqrt(Iu12),'--',betau,sqrt(Iu22),'-.');
    grid on
    xlabel('\beta=C_{ux}\cdot\omega\cdotL_{exp}/V')
    ylabel('Integral, I_u(\beta)')
    figure()
    loglog(betaw,sqrt(Iw11),'-',betaw,...
        sqrt(Iw12),'--',betaw,sqrt(Iw22),'-.'); grid on
    xlabel('\beta=C_{wx}\cdot\omega\cdotL_{exp}/V')
    ylabel('Integral, I_w(\beta)')
    xlim([0.1 100])
    figure()
    loglog(omegar.*Lexp./V(end),J11red,'b',...
        omegar.*Lexp./V(end),abs(J12red),'g',...
        omegar.*Lexp./V(end),J22red,'r');
    xlabel('\omega\cdotL_{exp}/V')
    ylabel('J_{red}^2')
    legend('J_{11}','J_{12}','J_{22}')
    title('The reduced joint acceptance function squared')
end

if PSDplot == 1
    figure()
    subplot(2,2,1)
    plotlog(V,abs(Srr11),omegar,Vplot);
    ylabel('S_{r_zr_z} (s\cdotm^2)')
    xlim([0.1 3])
    legend('Location','Southwest'); legend('boxoff')
    subplot(2,2,2)
    plotlog(V,abs(Srr12),omegar,Vplot);
    ylabel('S_{r_zr_\theta} (s\cdotm\cdotrad)')
    xlim([0.1 3]); legend off;
    subplot(2,2,3)
    plotlog(V,abs(Srr21),omegar,Vplot);
    xlabel('\omega (rad/s)')
```

```
    ylabel('S_{r_\thetar_z} (s\cdotm\cdotrad)')
    xlim([0.1 3]); legend off;
    subplot(2,2,4)
    plotlog(V,abs(Srr22),omegar,Vplot);
    xlabel('\omega (rad/s)')
    ylabel('S_{r_\thetar_\theta} (s\cdotrad^2)')
    xlim([0.1 3]); legend off;
end

if COVplot == 1
    CovCoef = COVzv./(sigmaz.*sigmav);
    figure()
    subplot(2,2,1); plot(V,sigmaz,'-o'); grid on;
    ylabel('\sigma_{r_zr_z} (m)')
    subplot(2,2,2); plot(V,CovCoef,'-o'); ylim([0 1]); grid on
    ylabel('\rho_{r_zr_\theta} (rad/s)')
    subplot(2,2,3); plot(V,sigmav,'-o'); grid on
    ylabel('\sigma_{r_\thetar_\theta} (rad)'); xlabel('V (m/s)')
    subplot(2,2,4); plot(V,omegaVv(1,1:length(omegaVv)-1),'b-o',...
        V,omegaVz(1,1:length(omegaVz)-1),'r-d'); grid on
    ylabel('\omega_i(V) (rad/s)'); xlabel('V (m/s)')
    legend('\omega_\theta','\omega_z','Location','Northwest'); legend('boxoff')
end

if damping_stiffness == 1
    figure()
    subplot(2,2,1); plot(V,zeta_z-z_aezz,'b-o',V,zeta_theta-z_aevv,'g-s');
    grid on; ylabel('\zeta_i_{tot}')
    legend('i = z','i = \theta','Location','Northwest')
    subplot(2,2,2); plot(V,k_aezz,'b-o',V,k_aevv,'g-s'); grid on
    ylabel('\kappa_{ae}_{i}')
    legend('i = z','i = \theta','Location','Northwest')
    subplot(2,2,3); plot(V,z_aezv,'b-o',V,z_aevz,'g-s'); grid on;
    legend('ij = z\theta','ij = \thetaz','Location','Southwest')
    ylabel('\zeta_{ae}_{ij}'); xlabel('V (m/s)')
    subplot(2,2,4); plot(V,k_aezv,'b-o',V,k_aevz,'g-s'); grid on
    ylabel('\kappa_{ae}_{ij}'); xlabel('V (m/s)')
    legend('ij = z\theta','ij = \thetaz','Location','Northwest')
    print -dtiff C:\Users\Notandi\Documents\MATLAB\Masteroppgave\kappazeta
end

%% Parametric study

if parameterstudy == 1

% Damping variation
col = {'b','r',[0 0.5 0]};
```

```
figure
for i = 1:3
    filename = [ 'dampingvar' num2str(i) '.mat' ];
    load(filename);
    hold on
    plot(V,sigmav,'-o','color',col{i})
end
xlabel('V (m/s)'); ylabel('\sigma_{r_\thetar_\theta} (rad)');
legend('\zeta_{\theta} = 0.0025','\zeta_{\theta} = 0.001',...
    '\zeta_{\theta} = 0.025','location','northwest')

% AD variation (omega_theta)
% H1
figure
subplot(2,2,1); grid on
hold all
plot(V,sigmav,'-o','color','b')
load 05H1.mat
plot(V,sigmav,'-o','color','r')
load 2H1.mat
plot(V,sigmav,'-o','color','g')
xlabel('V (m/s)'); ylabel('\sigma_{r_\thetar_\theta} (rad)');
ylim([0 0.12]);
legend('H1*','0.5\cdotH1*','2\cdotH1*','location','northwest')

% H2
load('response.mat','sigmav','V')
subplot(2,2,2); grid on
hold all
plot(V,sigmav,'-o','color','b')
load 05H2.mat
plot(V,sigmav,'-o','color','r')
load 2H2.mat
plot(V,sigmav,'-o','color','g')
xlabel('V (m/s)'); ylabel('\sigma_{r_\thetar_\theta} (rad)');
ylim([0 0.12]);
legend('H2*','0.5\cdotH2*','2\cdotH2*','location','northwest')

% H3
load('response.mat','sigmav','V')
subplot(2,2,3); grid on
hold all
plot(V,sigmav,'-o','color','b')
load 05H3.mat
plot(V,sigmav,'-o','color','r')
load 2H3.mat
plot(V,sigmav,'-o','color','g')
```

```
xlabel('V (m/s)'); ylabel('\sigma_{r_\thetar_\theta} (rad)');
ylim([0 0.12]);
legend('H3*','0.5\cdotH3*','2\cdotH3*','location','northwest')

% H4
load('response.mat','sigmav','V')
subplot(2,2,4); grid on
hold all
plot(V,sigmav,'-o','color','b')
load 05H4.mat
plot(V,sigmav,'-o','color','r')
load 2H4.mat
plot(V,sigmav,'-o','color','g')
xlabel('V (m/s)'); ylabel('\sigma_{r_\thetar_\theta} (rad)');
ylim([0 0.12]);
legend('H4*','0.5\cdotH4*','2\cdotH4*','location','northwest')

% A1
figure
subplot(2,2,1); grid on
load('response.mat','sigmav','V')
hold all
plot(V,sigmav,'-o','color','b')
load 05A1.mat
plot(V,sigmav,'-o','color','r')
load 2A1.mat
plot(V,sigmav,'-o','color','g')
xlabel('V (m/s)'); ylabel('\sigma_{r_\thetar_\theta} (rad)');
ylim([0 0.12]);
legend('A1*','0.5\cdotA1*','2\cdotA1*','location','northwest')

% A2
load('response.mat','sigmav','V')
subplot(2,2,2); grid on
hold all
plot(V,sigmav,'-o','color','b')
load 05A2.mat
plot(V,sigmav,'-o','color','r')
load 2A2.mat
plot(V,sigmav,'-o','color','g')
xlabel('V (m/s)'); ylabel('\sigma_{r_\thetar_\theta} (rad)');
ylim([0 0.12]);
legend('A2*','0.5\cdotA2*','2\cdotA2*','location','northwest')

% A3
load('response.mat','sigmav','V')
subplot(2,2,3); grid on
```

```
hold all
plot(V,sigmav,'-o','color','b')
load 05A3.mat
plot(V,sigmav,'-o','color','r')
load 2A3.mat
plot(V,sigmav,'-o','color','g')
xlabel('V (m/s)'); ylabel('\sigma_{r_\thetar_\theta} (rad)');
ylim([0 0.12]);
legend('A3*','0.5\cdotA3*','2\cdotA3*','location','northwest')

% A4
load('response.mat','sigmav','V')
subplot(2,2,4); grid on
hold all
plot(V,sigmav,'-o','color','b')
load 05A4.mat
plot(V,sigmav,'-o','color','r')
load 2A4.mat
plot(V,sigmav,'-o','color','g')
xlabel('V (m/s)'); ylabel('\sigma_{r_\thetar_\theta} (rad)');
ylim([0 0.12]);
legend('A4*','0.5\cdotA4*','2\cdotA4*','location','northwest')
end
```

B.2.2 modesh.m

```
% This matlab function plots the mode shape of a suspension bridge

% Input parameters:
% fiH - horizontal mode shapes obtained from exportResponseDat.m
% fiV - vertical mode shapes obtained from exportResponseDat.m
% fiT - torsional mode shapes obtained from exportResponseDat.m
% nModes - number of modes extracted from avlsat for each mode component

function modesh(fiHs,fiHa,fiVs,fiVa,fiTs,fiTa,nModesH,nModesV,nModesT,...
    omegaH,omegaV,omegaT)
X = [0 2050 -1.1 1.1]; % Axis settings
%% Horizontal modes
if isempty(fiHs) == 0
    h=figure(); hold all; grid off;
    for i = 1:2:(nModesH)
        subplot((nModesH/2),2,i)
        plot(fiHs(:,1),fiHs(:,(i+1)),'b-',...
            fiHs(:,1),fiHs(:,(i+2)),'r--')
        ylabel(['\phi_y_,_s_y_m_,_' num2str(i-0.5*(i-1))]);
        axis(X);
        text(40,-0.5,['\omega_y_s_' num2str(i-0.5*(i-1)) '=' num2str(...
            omegaH(i-0.5*(i-1),3),3) ' rad/s'])
        if i == 1
            title('Horizontal symmetric modes');
        end
        if i == 5
            xlabel('x');
        end
        subplot((nModesH/2),2,i+1)
        plot(fiHa(:,1),fiHa(:,(i+1)),'b-',...
            fiHa(:,1),fiHa(:,(i+2)),'r--')
        ylabel(['\phi_y_,_a_s_y_m_,_' num2str(i-0.5*(i-1))]);
        axis(X);
        text(40,-0.5,['\omega_y_a_' num2str(i-0.5*(i-1)) '=' num2str(...
            omegaH(i-0.5*(i-1)+nModesH/2,3),3) ' rad/s'])
        if i == 1
            title('Horizontal asymmetric modes');
        end
        if i == 5
            xlabel('x');
        end
    end
    saveas(h,sprintf('modeshH%d.tiff',1));
end
```

```
%% Vertical modes
if isempty(fiVs) == 0

    v=figure(); hold all; grid off;
    for i = 1:2:(nModesV)
        subplot((nModesV/2),2,i)
        plot(fiVs(:,1),fiVs(:,(i-0.5*(i-1)+1)))
        ylabel(['\phi_z_,_s_y_m_,_' num2str(i-0.5*(i-1))]);
        axis(X);
        text(40,-0.5,['\omega_z_s_' num2str(i-0.5*(i-1)) '=' num2str(...
            omegaV(i-0.5*(i-1),3),3) ' rad/s'])
        if i == 1
            title('Vertical symmetric modes');
        end
        if i == 5
            xlabel('x');
        end
        subplot((nModesV/2),2,i+1)
        plot(fiVa(:,1),fiVa(:,(i-0.5*(i-1)+1)))
        ylabel(['\phi_z_,_a_s_y_m_,_' num2str(i-0.5*(i-1))]);
        axis(X);
        text(40,-0.5,['\omega_z_a_' num2str(i-0.5*(i-1)) '=' num2str(...
            omegaV(i-0.5*(i-1)+nModesV/2,3),3) ' rad/s'])
        if i == 1
            title('Vertical asymmetric modes');
        end
        if i == 5
            xlabel('x');
        end
    end
    saveas(v,sprintf('modeshV%d.tiff',1));
end
%% Torsional modes
if isempty(fiTs) == 0
    % Symmetric:
    t=figure(); hold all; grid off;
    for i = 1:2:(nModesT)
        subplot((nModesT/2),2,i)
        plot(fiTs(:,1),fiTs(:,(i-0.5*(i-1)+1)))
        ylabel(['\phi_\theta_,_s_y_m_,_' num2str(i-0.5*(i-1))]);
        axis(X);
        text(40,-0.5,['\omega_\theta_s_' num2str(i-0.5*(i-1)) '=' num2str(...
            omegaT(i-0.5*(i-1),3),3) ' rad/s'])
        if i == 1
            title('Torsional symmetric modes');
        end
        if i == 5
```

```
            xlabel('x');
        end
        subplot((nModesT/2),2,i+1)
        plot(fiTa(:,1),fiTa(:,(i-0.5*(i-1)+1)))
        ylabel(['\phi_\theta_,_a_s_y_m_,_' num2str(i-0.5*(i-1))]);
        axis(X);
        text(40,-0.5,['\omega_\theta_a_' num2str(i-0.5*(i-1)) '=' num2str(...
            omegaT(i-0.5*(i-1)+nModesT/2,3),3) ' rad/s'])
        if i == 1
            title('Torsional asymmetric modes');
        end
        if i == 5
            xlabel('x');
        end
    end
    saveas(t,sprintf('modeshT%d.tiff',1));
end
```

B.2.3 plotlog.m

```
% This function generates a logarithmic plot of variables X and Y.
% This works for any length of Vplot and thus supports multiple plots
% in the same figure or subplot diagram.
%
% Parameter definitions:
% V - Mean Wind Velocity [m/s]
% Vplot - A vector of the mean wind velocities at which to plot [m/s]

function plotlog(V,Y,X,Vplot)
grid on;
C = {'b','r',[0 0.5 0],[0.7 0 0.7],[0.7 0.7 0]};
L = {'-','--','--','--','--'};
for k = 1:length(Vplot)
    ind = find(V == Vplot(k));
    if k <6
    color = C{k};
    line = L{k};
    loglog(X(1,:),Y(ind,:),'color',color,'linestyle',line); grid on
    legendInfo{k} = ['V = ' num2str(Vplot(k),3) ' m/s'];
    else
    color = rand(1,3);
    loglog(X(1,:),Y(ind,:),'color',color,'linestyle','--');
    legendInfo{k} = ['V = ' num2str(Vplot(k),3) ' m/s'];
    end
    hold on
end
hold off
legend(legendInfo,'Location','Northwest')
legend('boxoff')
```

B.2.4 plotADs.m

```
% This function plots defined aerodynamic derivatives for a structure.
% Optionally, flat plate aerodynamic derivatives can be included for
% comparison.
%
% Parameter definitions:
% Vred_z,Vred_theta - Reduced mean wind velocities in the vertical
%                     direction and in torsion, respectively
% ADs               - Aerodynamic derivatives
% Hnpl,Anpl         - Flat plate aerodynamic derivatives, n = 1,2,3,4

function plotADs(Vred_z,Vred_theta,ADs,varargin)

%Optional parameters, used for flat plate ADs.
switch nargin
    case 3
    case 11
        H1pl = varargin{1}; A1pl = varargin{5};
        H2pl = varargin{2}; A2pl = varargin{6};
        H3pl = varargin{3}; A3pl = varargin{7};
        H4pl = varargin{4}; A4pl = varargin{8};
    otherwise
        error('Unexpected inputs')
end

% Plot of Hn
figure();
subplot(4,2,1); plot(Vred_z,ADs(1,:),'b'); ylabel('H_1*');
xlim([min(Vred_z) max(Vred_z)]); grid on;
if exist('H1pl','var')
    hold on; plot(Vred_z,H1pl,'r--');ylabel('H_1*'); hold off
end
subplot(4,2,2);plot(Vred_theta,ADs(2,:),'b');ylabel('H_2*');
xlim([min(Vred_z) max(Vred_z)]); grid on;
if exist('H2pl','var')
    hold on; plot(Vred_theta,H2pl,'r--');ylabel('H_2*'); hold off
end
subplot(4,2,3); plot(Vred_z,ADs(3,:),'b'); ylabel('H_3*');
xlim([min(Vred_z) max(Vred_z)]); grid on;
if exist('H3pl','var')
    hold on; plot(Vred_z,H3pl,'r--');ylabel('H_3*'); hold off
end
subplot(4,2,4);plot(Vred_theta,ADs(4,:),'b');ylabel('H_4*');
xlim([min(Vred_z) max(Vred_z)]); grid on;
if exist('H4pl','var')
```

```
    hold on; plot(Vred_theta,H4pl,'r--');ylabel('H_4*'); hold off
end

% Plot of An
subplot(4,2,5); plot(Vred_z,ADs(5,:),'b'); ylabel('A_1*');
xlim([min(Vred_z) max(Vred_z)]); grid on;
if exist('A1pl','var')
    hold on; plot(Vred_z,A1pl,'r--');ylabel('A_1*'); hold off
end
subplot(4,2,6);plot(Vred_theta,ADs(6,:),'b');ylabel('A_2*');
xlim([min(Vred_z) max(Vred_z)]); grid on;
if exist('A2pl','var')
    hold on; plot(Vred_theta,A2pl,'r--');ylabel('A_2*'); hold off
end
subplot(4,2,7); plot(Vred_z,ADs(7,:),'b'); ylabel('A_3*');
xlabel('V/(B\omega_i)');
xlim([min(Vred_z) max(Vred_z)]); grid on;
if exist('A3pl','var')
    hold on; plot(Vred_z,A3pl,'r--');ylabel('A_3*'); hold off
end
subplot(4,2,8);plot(Vred_theta,ADs(8,:),'b');ylabel('A_4*');
xlabel('V/(B\omega_i)');
xlim([min(Vred_z) max(Vred_z)]); grid on;
if exist('A4pl','var')
    hold on; plot(Vred_theta,A4pl,'r--');ylabel('A_4*'); hold off
end
set(gcf,'NextPlot','add');axes;
h = title('Aerodynamic derivatives');
set(gca,'Visible','off');set(h,'Visible','on');

print -dtiff C:\Users\Notandi\Documents\MATLAB\Masteroppgave\AD
```